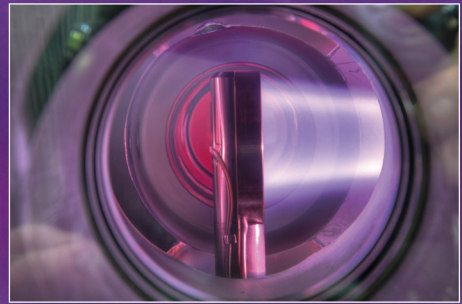
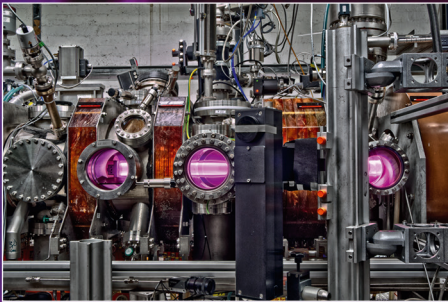


# Influence of Impurities on the Fuel Retention in Fusion Reactors

Michael Reinhart



Energie & Umwelt /  
Energy & Environment  
Band / Volume 296  
ISBN 978-3-95806-105-7





Forschungszentrum Jülich GmbH  
Institute of Energy and Climate Research  
Plasma Physics IEK-4

# Influence of Impurities on the Fuel Retention in Fusion Reactors

Michael Reinhart

Schriften des Forschungszentrums Jülich  
Reihe Energie & Umwelt / Energy & Environment

Band / Volume 296

---

ISSN 1866-1793

ISBN 978-3-95806-105-7

Bibliographic information published by the Deutsche Nationalbibliothek.  
The Deutsche Nationalbibliothek lists this publication in the Deutsche  
Nationalbibliografie; detailed bibliographic data are available in the  
Internet at <http://dnb.d-nb.de>.

Publisher and  
Distributor: Forschungszentrum Jülich GmbH  
Zentralbibliothek  
52425 Jülich  
Tel: +49 2461 61-5368  
Fax: +49 2461 61-6103  
Email: [zb-publikation@fz-juelich.de](mailto:zb-publikation@fz-juelich.de)  
[www.fz-juelich.de/zb](http://www.fz-juelich.de/zb)

Cover Design: Grafische Medien, Forschungszentrum Jülich GmbH

Printer: Grafische Medien, Forschungszentrum Jülich GmbH

Copyright: Forschungszentrum Jülich 2015

Schriften des Forschungszentrums Jülich  
Reihe Energie & Umwelt / Energy & Environment, Band / Volume 296

D 294 (Diss., Bochum, Univ., 2015)

ISSN 1866-1793  
ISBN 978-3-95806-105-7

The complete volume is freely available on the Internet on the Jülicher Open Access Server (JuSER)  
at [www.fz-juelich.de/zb/openaccess](http://www.fz-juelich.de/zb/openaccess).

Neither this book nor any part of it may be reproduced or transmitted in any form or by any  
means, electronic or mechanical, including photocopying, microfilming, and recording, or by any  
information storage and retrieval system, without permission in writing from the publisher.

## Abstract

The topic of this thesis is the influence of plasma impurities on the hydrogen retention in metals, in the scope of plasma-wall-interaction research for fusion reactors. This is addressed experimentally and by modelling. The mechanisms of the hydrogen retention are influenced by various parameters like the wall temperature, ion energy, flux and fluence as well as the plasma composition. The plasma composition is a relevant factor for hydrogen retention in fusion reactors, as their plasma will also contain impurities like helium or seeded impurities like argon.

The experiments treated in this thesis were performed in the linear plasma generator PSI-2 at Forschungszentrum Jülich, and are divided in 3 parts: The first experiments cover the plasma diagnostics, most importantly the measurement of the impurity ion concentration in the plasma by optical emission spectroscopy. This is a requirement for the later experiments with mixed plasmas. Diagnostics like Langmuir probe measurements are not applicable for this task because they do not distinguish different ionic species. The results also show that the impurity ion concentrations cannot be simply concluded from the neutral gas input to the plasma source, because the relation between the neutral gas concentration and impurity ion concentration is not linear.

The second and main part of the experiments covers the exposure of tungsten samples to deuterium plasmas. In the experiments, the impurity ion type and concentration is varied, to verify the general influence of helium and argon on the deuterium retention in tungsten samples exposed at low temperatures. It shows that helium impurities reduce the amount of retained deuterium by a factor of 3, while argon impurities slightly increase the total retention, compared to exposures to a pure deuterium plasma. Cross-sections of the exposed tungsten surfaces via TEM-imaging reveal a 12-15 nm deep helium nanobubble layer at the surface of the sample, while for the cases of pure deuterium or deuterium + argon exposures, a damaged layer of less than 5 nm thickness is observed. Connections between the helium nanobubbles provide a path for the molecular deuterium to the surface, which leads to the reduction of the total deuterium retention. The second part of the tungsten exposures investigates the influence of helium impurities under the variation of the ion fluence. It is found that the reduction factor for the deuterium retention stays constant in the fluence range investigated.

The last part of the experiments are exposures of aluminium samples to deuterium plasmas with helium and argon impurities of different concentrations, and the comparison with literature results for the same exposure conditions with beryllium sam-

ples. The results for the deuterium retention show a clearly different behaviour of aluminium and beryllium: While argon reduces the deuterium retention in beryllium, the deuterium retention in aluminium remains unchanged. But besides the deuterium retention, the surface modifications and erosion of aluminium and beryllium are found to have some similarities: With a pure deuterium plasma or a deuterium-helium plasma exposure, a grass-like structure is formed on the surface of both materials. With argon impurities in the deuterium plasma, these structures are suppressed. The reason for the formation of these structures are differences in the angular dependence of the sputtering yields of deuterium, helium and argon. The presence or absence of these structures also influences the surface erosion in the same way for both materials.

To work out the physical effects causing the results regarding the deuterium retention in tungsten, a diffusion model is developed, which calculates the distribution and total amount of deuterium in a metallic surface by diffusion and trapping in helium nanobubbles. It is then checked how the model agrees with the measurements performed at PSI-2. The results of the diffusion model simulations show that the reduction in the total deuterium retention and its fluence dependency correlates with the thickness of the helium nanobubble layer. Also, the increasing deuterium retention with argon impurities can be explained by the same model with a very shallow layer of argon-induced defects in the sample surface.

# Contents

<b>1</b>	<b>Introduction</b>	<b>6</b>
<b>2</b>	<b>Basics of deuterium retention in metals</b>	<b>10</b>
2.1	Diffusion and trapping of deuterium in tungsten . . . . .	10
2.2	Exposure parameters influencing the deuterium retention . . . . .	13
2.3	Helium and argon effects on deuterium retention . . . . .	14
<b>3</b>	<b>Experimental setup</b>	<b>17</b>
3.1	Linear plasma generator PSI-2 . . . . .	17
3.2	Langmuir probe . . . . .	21
3.3	Optical emission spectroscopy . . . . .	23
3.4	Target manipulators . . . . .	29
3.5	Thermal desorption spectroscopy . . . . .	33
<b>4</b>	<b>Experimental results</b>	<b>37</b>
4.1	Plasma characterization by optical emission spectroscopy . . . . .	37
4.1.1	Electron density: Balmer line ratios . . . . .	37
4.1.2	Electron density: Fulcher band lines . . . . .	40
4.1.3	Electron density: Paschen line Stark broadening . . . . .	43
4.1.4	Electron temperature: Paschen lines ratio . . . . .	46
4.1.5	Argon ion concentration . . . . .	48
4.1.6	Helium ion concentration . . . . .	54
4.2	Studies of deuterium retention in tungsten . . . . .	61
4.2.1	Surface modifications . . . . .	63
4.2.2	Deuterium retention with plasma impurities . . . . .	68
4.2.3	Deuterium retention with variation of ion fluence . . . . .	72
4.3	Studies of deuterium retention and erosion of aluminium and beryllium	74
4.3.1	Surface modifications . . . . .	76
4.3.2	Sputter yields . . . . .	84
4.3.3	Deuterium retention . . . . .	88
<b>5</b>	<b>Modelling of deuterium diffusion in metals</b>	<b>92</b>
5.1	Influence of helium nanobubbles . . . . .	100
5.2	Implementation of argon-induced defects . . . . .	104
5.3	Fluence dependency . . . . .	106

---

<b>6</b>	<b>Conclusions</b>	<b>111</b>
<b>7</b>	<b>Appendix I: Diffusion simulation MATLAB code</b>	<b>117</b>
<b>8</b>	<b>References</b>	<b>124</b>
<b>9</b>	<b>List of figures</b>	<b>134</b>



# 1 Introduction

One of the most important requirements for the development and growth of the global society and economy is to ensure a sufficient and reliable energy supply. The current global energy supply relies mainly on fossil fuels, nuclear fission and renewable energies. However, each of these methods also has drawbacks: The fossil fuels are limited and are related to climate change, nuclear fission contains the dangers of radioactive materials with very long decay times, and renewable energies are depending on other energy sources or energy storage when their own energy production is low.

An energy source which does not have any of these drawbacks would be nuclear fusion. As a nuclear energy, the fundamental source for this type of energy source is the binding energy between the nucleons in an atomic core. The binding energy is caused by the strong interaction (attracting) and the coulomb force (repulsive) between the nucleons. It turns out that Nickel-62 has the highest binding energy per nucleon [1]. With higher and lower atomic masses, the binding energy per nucleon decreases. A higher binding energy also entails that the mass defect is higher: The mass of the nucleus is smaller than the sum of the single nucleons masses, the difference being the binding energy. When two light atomic cores are combined to one heavy core in a fusion reaction, the total mass decreases. This mass defect is transformed into kinetic energy and can be used as an energy source.

To achieve the fusion of two positively charged cores, their repulsive force has to be overcome by the addition of energy into the system. For a power plant, the corresponding energy yield has to be positive, otherwise the fusion reaction is not producing net energy. To reach a positive yield, the triple product  $nT\tau$  [2] of density ( $n$ ), temperature ( $T$ ) and confinement time ( $\tau$ ) has to reach a certain minimum value, depending on the type of fusion reaction. This means there are different ways of realizing energy production by a fusion reaction. If the confinement time is short, the density must be very high. This method is represented by so-called inertial-confinement fusion reactors [3]. However, with magnetic confinement fusion, the density does not need to be as high, because the confinement time is increased. In fusion power plants, the two hydrogen isotopes deuterium and tritium will be used for the fusion reaction, because they reach the highest reaction rate at relatively low temperatures [4]. The products of this reactions are one helium nucleus and one neutron, both with high kinetic energies (He: 3.5 MeV, n: 14 MeV). Although the D-T reaction is the optimal one in terms of the required temperature and reaction

rate, the elements still have to be heated up to 10 keV for reaching a sufficiently high reaction rate.

At these energies, the deuterium and tritium are in the state of a plasma. This has the advantage that the plasma can be confined by magnetic fields. For the best confinement, the plasma is formed in a torus-like shape (Tokamak- or Stellarator-design). With the Tokamak design, some key points for a nuclear fusion reactor have been reached: The plasma can be confined well enough to reach temperatures and densities which are required for a positive power yield. In the Tokamak JET, the energy output from the fusion reaction almost reached the energy input in the plasma for the first time in 1997. The ITER project is believed to show that a positive energy yield can be maintained for a longer time.

One of the open questions of magnetic confinement fusion concerns the wall material of the inner reactor vessel. Although the plasma is well confined by magnetic fields, it still has to be in contact with the wall. This is due to the products of the fusion reaction. While the neutrons are not confined by the magnetic field and can reach the wall undisturbed, the helium ions are confined by the magnetic field in the same way as the deuterium-tritium plasma. However, there must be a steady removal of helium to prevent the accumulation of helium in the plasma. This is realized by a plasma-wall-contact at the divertor, a section of the inner wall specially designed to take up the heat and particle load from the plasma. The divertor is visible as the w-shaped element at the bottom of the Tokamak cross section in figure 1.

In this area, additional magnetic coils open the magnetic field lines and guide the plasma onto the divertor wall elements. At the current state of research, the wall material for the divertor will be tungsten. Tungsten has the highest melting point of any metal and low deuterium retention compared to other possible materials like carbon. Experiments have shown that the deuterium retention in a tungsten-tokamak is reduced by a factor of ten compared to tokamaks with carbon wall elements [5]. The contact of the wall materials (with temperatures

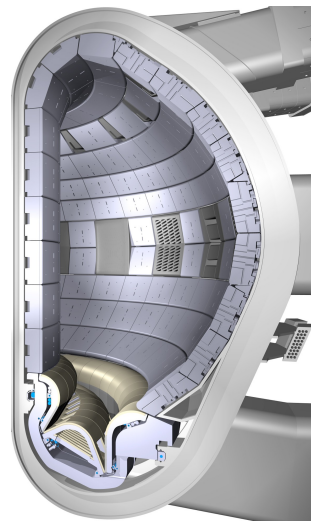


Figure 1: Divertor in ITER

of around 200°C to 1000°C depending on the specific region) with the plasma leads to trapping of deuterium, tritium and impurities in the wall material. This raises the problems of fueling efficiency and safety of the reactor. Tritium permanently retained in the wall is lost for the fusion process, and it increases the total content of radioactive material which is present in the reactor. Also, it is possible that tritium diffuses through the whole bulk material of the plasma-facing component. Then tritium can get in contact with i.e. the coolant, which leads to contamination of outer parts of the reactor.

Therefore, the research on hydrogen isotope retention in fusion reactor wall materials is important for the success of the fusion reactor as a power plant. Since there are numerous factors which influence the retention, a study of the principal mechanisms behind the retentions can be difficult. In linear plasma devices, many factors like the exposure conditions and plasma parameters are much easier to control than in an actual Tokamak. Keeping in mind that no linear plasma device can fully recreate the conditions in a tokamak, the linear plasma devices have proven to be a good tool for the research on hydrogen isotope retention.

One aspect which influences the hydrogen retention is the presence of impurities in the fusion plasma. One unavoidable impurity is helium, as it is one of the reaction products of the D-T fusion reaction. Other impurities might be seeded into the plasma to achieve radiation cooling of the plasma, which reduces the risk of local overheating of wall elements [6]. In this thesis, besides helium, argon is investigated as a possible seeded impurity.

The experiments were performed at the linear plasma generator PSI-2 at Forschungszentrum Jülich. Here, sample materials can be exposed to a steady-state deuterium plasma, while parameters like the ion energy, ion fluence, sample temperature and plasma composition can be changed independently. For safety reasons, tritium cannot be used for the experiments. But the results from studies on deuterium are also valid for tritium [7]. A detailed description of PSI-2 and its diagnostics is given in section 3.

The first part of the experiments in section 4.1 is about plasma diagnostics by optical emission spectroscopy. Here, methods to measure the electron density, electron temperature and especially the impurity ion content are presented. Because the spectroscopic systems were not yet fully implemented at PSI-2 prior to this thesis, the realization of these measurements is a critical factor required for the subsequent exposures of samples to mixed plasmas. The ratio of the impurity ions to deuterium ions can only be measured with the optical emission spectroscopy, and not by the Langmuir probe.

---

The second and third part of the experiments are exposures and subsequent analysis of tungsten (section 4.2) and aluminium (section 4.3) samples. Aluminium will not be used in a fusion reactor, but it is used as a proxy material for beryllium (which will be the first wall material in ITER) in some plasma-wall-interaction facilities which cannot handle beryllium. The results of the aluminium exposures shown in this thesis are compared to comparable exposures of beryllium samples from literature, to figure out if the substitution of beryllium by aluminium is reasonable for these experiments. The results show which similarities or differences between aluminium and beryllium are existing regarding the deuterium retention, surface morphology and sputtering yields.

For tungsten, it is already known from literature that helium impurities reduce the deuterium retention by the formation of helium nanobubbles in the tungsten surface. But impacts of other exposure parameters, like the deuterium fluence to the material or the material temperature, are not yet studied as broadly as for pure deuterium exposures. The effect of argon impurities on the deuterium retention has not yet been studied systematically at all. But the effects of plasma impurities on the deuterium retention are important to make conclusions and predictions on the deuterium retention in future fusion reactors.

In this thesis, it is investigated if the helium nanobubbles can also be detected and lead to reduced deuterium retention for low sample temperatures of 380 K. Also, the influence of the plasma fluence on the reduction in total deuterium retention by helium is investigated experimentally. Similar exposures are performed with argon impurities, to find out the influence of argon on the total deuterium retention and compare it to the effects of helium.

The experimental results are compared with a diffusion model developed for this thesis in section 5. The model calculates the diffusion of deuterium in metals in one dimension and under the influence of certain impurities, which locally change the diffusion and trapping behaviour of deuterium. The model helps to interpret the experimental results and gives a more detailed image of the influence of helium and argon impurities on the deuterium retention.

## 2 Basics of deuterium retention in metals

The following section gives an overview of the mechanisms behind the diffusion and trapping of hydrogen/deuterium in metals, particularly in tungsten. Also, the influence of helium and argon on the deuterium retention is described.

### 2.1 Diffusion and trapping of deuterium in tungsten

As it was mentioned in the introduction, the inner wall of a fusion reactor is under bombardment of deuterium/tritium, helium and impurity ions as well as neutrons. In this section, the focus is on the deuterium ions. When a deuterium ion reaches the surface of the wall, it can get retained inside the wall material. Figure 2 shows a schematic overview of this situation: On the left side is the incident flux of atomic

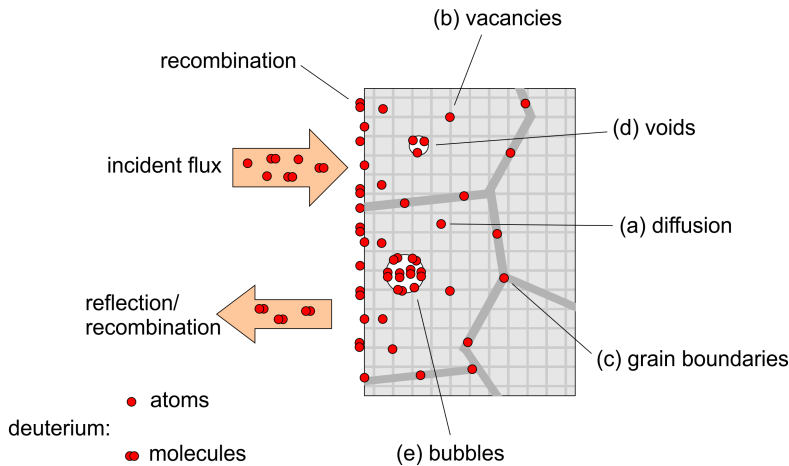


Figure 2: The different forms of deuterium retention in metals

and molecular deuterium ions. They can either get reflected from the surface, be adsorbed at the surface, or penetrate the surface. The latter is only possible for atomic ions, while molecular ions first have to be adsorbed and dissociated before they can get into the lattice [8]. The initial implantation depth is depending on the ion energy, for divertor conditions with 10-100 eV ion energies it is typically in the range of a few nm [9].

Once the deuterium atomic ions are soluted in the implantation zone, they are - for the case of tungsten - typically occupying the tetrahedral interstitial sites in the bcc lattice [7]. The location of the tetrahedral sites is shown in figure 3. In the case of tungsten, the solution of deuterium is endothermic, which means energy has to be added to the system for the deuterium to be soluted. A scheme of the energy levels of deuterium in tungsten is shown in figure 4. The figure shows the interstitials in tungsten as minima in the potential energy; the deuterium can diffuse from one interstitial to another with the diffusion energy barrier  $E_D$  either thermally activated or, at low temperatures, by quantum-mechanical tunneling [7]. The temperature depen-

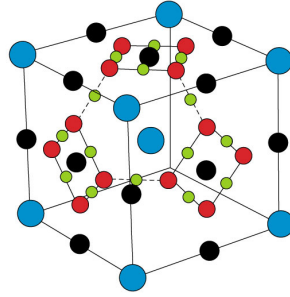


Figure 3: Tetrahedral (red), trigonal (green) and octahedral (black) interstitials in the bcc lattice (blue) [10]

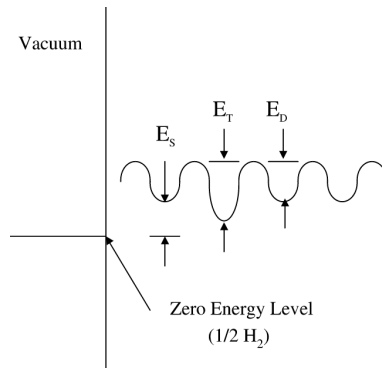


Figure 4: Energy levels for the solution ( $E_S$ ), diffusion ( $E_D$ ) and trapping ( $E_T$ ) of deuterium in tungsten [11]

dence of the diffusion is given by the diffusion coefficient  $D = D_0 \cdot \exp(-E_D/kT)$ . Actual values for the pre-factor  $D_0$  and the diffusion energy  $E_D$  are typically taken from experiments, the best-known example being the Frauenfelder diffusion  $D = 4.1 \cdot 10^{-7} \text{ m}^2\text{s}^{-1} \cdot \exp(-0.39 \text{ eV}/kT)$  [12]. The diffusivity of deuterium in tungsten is relevant even at room temperature [11]. Therefore, in a ideal tungsten lattice without defects, the deuterium atoms could diffuse through the whole tung-

sten sample without being retained. This implies that for the long-term retention of deuterium in plasma-exposed tungsten surfaces, defects, which act as trapping sites for deuterium, play the major role. In figure 4, they are indicated with their trapping energy  $E_T$ . Because the trapping energies  $E_T$  are larger than the diffusion energy for interstitials  $E_D$  [11], the traps decrease the effective diffusion if the temperature is low enough that the majority of the deuterium can get trapped. There are different forms of trapping sites for deuterium in tungsten besides the interstitials (a) (as indicated in figure 2):

- (b): Vacancies in the lattice structure, which are single missing tungsten atoms, whose positions can be taken by deuterium atoms. The missing tungsten atom can be located at another position in the lattice which is normally not occupied by a tungsten atom; this is called a Frenkel defect.
- (c): Grain boundaries, in which the density of vacancies and lattice defects is much higher than in the grains itself.
- (d): Voids, areas in which a larger number of related tungsten atoms is missing and can be occupied by deuterium atoms.
- (e): Bubbles, large voids which can not only be populated by soluted deuterium atoms, but actually filled by deuterium gas molecules. This can lead to high pressures in the MPa range, resulting in the growth of the bubbles and eventually blister formation on the surface [8].

The origin of the different trapping sites can be intrinsic defects due to the production and preparation of the samples (grain boundaries, surface damages), or defects induced by different kinds of particle fluxes during the experiment (high energy neutrons, alpha particles, hydrogen or impurity ions). The density of the trapping sites can be up to 10% of the material's atomic density for ion-induced traps [8]. All these trappings sites have trapping energies in the range of 1-2 eV [11]. The trapping energy of deuterium trapped in exposed tungsten samples can be measured by thermal desorption spectroscopy. The methods to deduce the trapping energy from the temperature spectrum are described in section 3.5. From the knowledge of the trapping energies, one can draw conclusions about the type of trapping in the experiment.

## 2.2 Exposure parameters influencing the deuterium retention

Several factors influence the deuterium retention in tungsten. The following section gives a short overview from literature about some of the factors which can influence the deuterium retention. The knowledge of these dependencies is also important for the interpretation of the results from this thesis.

### Sample temperature

Studies on the temperature dependence of the deuterium retention in tungsten have shown that the retention of deuterium has a maximum at about 500 K sample temperature [13]. At lower temperatures, the diffusion of implanted deuterium into deeper regions of the sample is smaller than at 500 K, because the diffusion coefficient is proportional to the temperature. As a consequence of the lower diffusion, the concentration of deuterium in the implantation zone directly below the surface increases, which leads to higher surface losses due to recombination at the surface. However, the total deuterium retention also decreases with temperatures above 500 K, although the diffusion is increasing. This can be explained by detrapping of deuterium from trapping sites, which starts to occur at temperatures above 500 K. The deuterium can no longer stay effectively trapped in the trapping sites and can diffuse to the surface, where it leaves the sample. This is the same effect which is used for the measurement of deuterium retention by thermal desorption spectroscopy (section 3.5), but here it is already appearing during the exposure of the sample.

### Ion fluence

The ion fluence is the integrated amount of deuterium flux to the sample over the exposure time. The influence of the ion fluence is strongly dependent on the sample temperature. As explained above, at low temperatures (300 K) the diffusivity of deuterium in tungsten is lower than at high temperatures, which leads to high deuterium concentrations near the surface and higher losses due to surface recombination. This causes the deuterium retention to saturate at fluences above  $10^{23} \text{ m}^{-2}$  [14]. At higher temperatures (500 K), the diffusion is high enough to distribute the deuterium more evenly and deeper into the material. At this temperature, no saturation is observed [13, 14]. Typically, the deuterium content increases with the square root of the incident fluence.

### Ion flux

A minimum ion flux of  $10^{18} \text{ m}^{-2}\text{s}^{-1}$  was found to be required for a relevant amount of deuterium retention [13]. The suggested explanation is that low fluxes do not produce high enough deuterium concentrations to cause lattice distortions in the tungsten sample. Assuming these to be the main trapping sites, there are less trapping sites available and the deuterium can diffuse faster to the surface and recombine. With higher fluences, there is no dependence of the deuterium retention on the ion flux. However, in [15] it was found that for high fluxes ( $10^{24} \text{ m}^{-2}\text{s}^{-1}$ ) and low sample temperatures, the deuterium retention can be lower than for the same total fluence at a lower flux. This is correlated to the very high density of deuterium caused in the implantation region due to the high flux, which, together with the relatively low diffusion, leads to high surface losses from recombination.

### 2.3 Helium and argon effects on deuterium retention

When the plasma contains impurities such as helium or argon, which will also be the case for the plasma in future fusion reactors, the impurities can be retained in the samples and/or induce damages as well. There has already been much research on this topic regarding helium, less so on argon. In this section, the influence of helium on the deuterium retention is explained, and also possible differences for the influence of argon are mentioned.

It can be assumed that impurities can increase the deuterium retention if their ion energies are high enough to sufficiently increase the number of trapping sites by ion-induced damages. The higher trapping site density will increase the deuterium retention [16]. However, at lower ion energies, when helium does not influence the tungsten lattice directly by displacement damage, one can also observe a reduction in the deuterium retention [17]. This is due to effects which the implanted helium has on

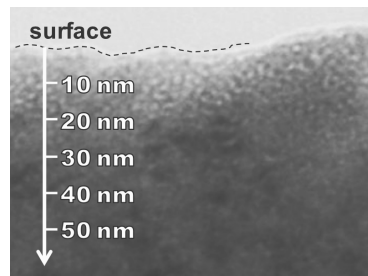


Figure 5: TEM images of helium nanobubbles by helium plasma exposure at 570 K [17]

the implanted deuterium.

To explain this, one first has to look at the differences between helium and deuterium trapped in tungsten. One of them is the different depths at which deuterium and helium are retained in tungsten: While the implantation depth of deuterium and helium is similar (below 10 nm for low ion energies below the threshold energy for sputtering [18, 19]), the actual depth at which deuterium and helium is retained, is different [19, 20]. In the cited works this is connected to a faster diffusion of deuterium in tungsten, and also a stronger self-trapping of helium. Helium is trapped by already existing helium impurities in tungsten, which is not the case for deuterium [21].

This also leads to the observed strong surface modifications of tungsten by helium implantation (nanobubbles, tungsten fuzz). The nanobubbles are the first sign of the surface modifications, and they evolve into bigger bubbles and tungsten fuzz as shown in [21, 22] with high sample temperatures and ion fluence [23]. The formation of the helium nanobubbles does not depend on the incident energy of the helium ions [21]. From this, it can be concluded that the helium nanobubbles are formed due to the high helium concentration in the metal, and not by damages induced by the impinging ions. An example for helium nanobubbles observed at moderate temperatures (570 K) from [17] is shown in figure 5.

When hydrogen and helium are implanted simultaneously, experiments show that also the deuterium does not diffuse as deep into the material as with pure deuterium exposures [24]. This can be explained by the trapping of deuterium in or at helium nanobubbles, which was shown in [25]. The deuterium is preferably trapped in these strong trapping sites, which reduces the diffusion of deuterium into deeper regions of the tungsten sample. But, with these additional trapping sites created in the tungsten lattice, one would assume an increase in the total deuterium retention, which is in conflict to the experimental observations. The explanation for the reduced deuterium retention by helium impurities in the plasma lies in the density of the helium nanobubbles. If these bubbles reach a certain volume density, they connect and can build paths from bubbles inside the tungsten lattice to the surface. This is effectively increasing the surface area of the tungsten sample, and the trapped deuterium can recombine and leave the surface. This is obvious for tungsten fuzz, where the surface area is drastically increased. But also for the case of only the formation of helium nanobubbles, and no apparent change of the top surface, an influence of the porous structure can be assumed. As mentioned in [26], a volume density of only 16% is sufficient for the interconnection of helium nanobubbles. For the case of argon implantation in tungsten samples, no modifications like nanobubbles or fuzz

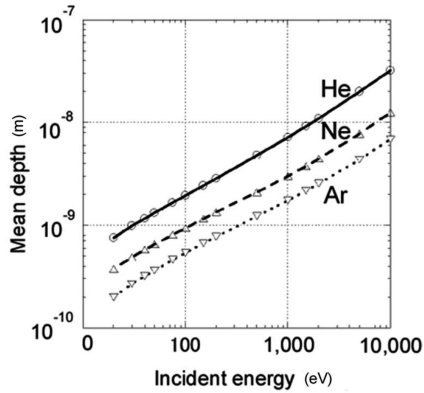


Figure 6: Implantation depth of noble gas ions in tungsten in dependence of the incident energy [27]

are observed in literature. This can be explained by the differences in penetration depths and sputtering yields for helium and argon [27]. In figure 6, calculated penetration depths of helium, neon and argon are shown. It is clearly visible that at the same ion energy, helium is implanted five times deeper than argon. But, it is assumed in [27] that the creation of helium nanobubbles requires a certain minimum implantation depth of helium; because for very low incident energies ( $< 20$  eV), no helium nanobubbles or fuzz can be observed. For argon to reach the same implantation depth as helium at 20 eV, the required incident ion energy is 200 eV. This is already above the sputter threshold energy for argon on tungsten. Therefore, it can be assumed that for tungsten exposed to argon, the surface erosion is dominating and nanobubbles cannot be formed or are directly eroded again.

## 3 Experimental setup

### 3.1 Linear plasma generator PSI-2

The Linear Plasma Generator PSI-2 Jülich is the main experiment for plasma-wall-interaction research at the IEK-4 institute of Forschungszentrum Jülich. It is in operation since 2011 [28], priorly the experiment was located at the Humboldt-University in Berlin [29].

PSI-2 has two main purposes: First, it acts as a "pilot-experiment" for the JULE-PSI project. The latter is a linear plasma generator similar to PSI-2, which will be located in a hot cell environment. Hence it is capable of handling radioactive substances, in particular neutron activated materials like tungsten, for plasma-wall-interaction research. Since the wall materials in a fusion reactor will also be strongly activated due to the fast neutrons produced in the fusion reaction, this topic is of great interest. The role of PSI-2 in this project is to get insight and experience in the operation of a linear plasma device, and to support the planning and construction of JULE-PSI. Second, it also contributes to the ongoing plasma-wall-interaction research at IEK-4, like liquid wall materials, surface morphology of tungsten, or the deuterium retention discussed in this thesis.

PSI-2 produces a plasma column of 6 cm in diameter and 2,5 m in length. The plasma parameters which can be reached in the target area of PSI-2 are shown in table 1 for a typical deuterium plasma discharge. One has to keep in mind that these numbers can vary considerably depending on the discharge power, the type of gas or the neutral gas pressure in the chamber. For example, with helium elec-

electron density	$1 \cdot 10^{18} \text{ m}^{-3}$
electron temperature	10 eV
ion temperature	3 eV
ion flux	$1 \cdot 10^{22} \text{ m}^{-2}\text{s}^{-1}$
neutral pressure	$5 \cdot 10^{-2} \text{ Pa}$
magnetic field	100 mT

Table 1: Typical deuterium plasma parameters in PSI-2

tron temperatures much higher than 10 eV are easily reached, while typical electron temperatures in argon plasmas are around 3 eV.

In image 7, the general layout of PSI-2 is shown. In this scheme, the main plasma chamber of PSI-2 is shown without the two sample manipulators, which are described in section 3.4.

The plasma source is found on the left side of the picture. Here, the plasma column

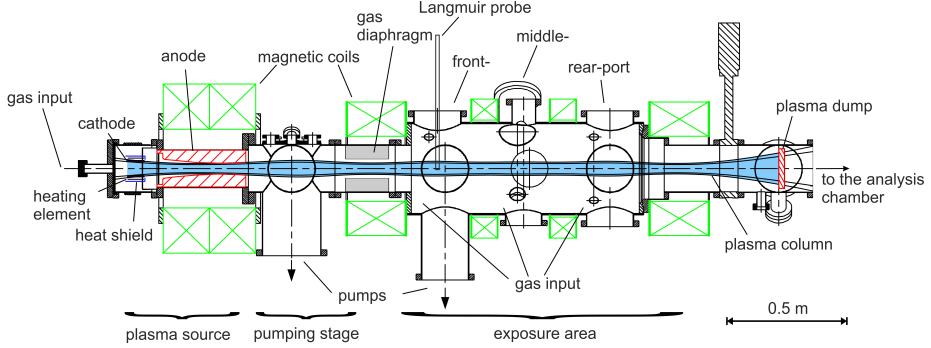


Figure 7: Layout of PSI-2 [30]

is produced by an arc discharge and extends into the main chamber. A relatively high gas pressure of several Pa in the source is required for a proper operation of the plasma source. Therefore, there is a pumping stage located between the plasma source and the main chamber: It consists of a gas diaphragm, which only allows the plasma column to pass, while the surrounding neutral gas is predominantly blocked and pumped away by a turbomolecular pump in this area.

In the exposure area the samples are exposed to the plasma. The plasma diagnostics, consisting of the Langmuir probe (section 3.2) and the optical emission spectroscopy (section 3.3), are also located here. The target chamber has 3 planes (front, middle, and back) with several ports for diagnostics at each plane. The side target manipulator is located at the middle plane, while the target station manipulator can be moved to each point along the axis in the target chamber. To keep the profile of the plasma exposure constant at each plane, which is important if the target station manipulator is used at different locations, the magnetic coils are set up to produce a constant magnetic field along the axis in the target area (figure 9, with the target area between 1.8 and 2.5 m). If the target station manipulator is not in use, the plasma dump (a cooled copper plate at floating potential) must be used to terminate the plasma at the end of the chamber. When the target station manipulator is used, a separate plasma dump is not needed because of the size of the target station manipulator. There, the complete plasma column is terminated at the manipulator head.

### Plasma source

In PSI-2 an arc discharge is used as the plasma source. It consists of a cylindrically shaped cathode and anode. Figure 8 shows a picture of the cylindrical cathode. Around the inner cylinder, which is the actual cathode, the heating element is located, which is cylindrical as well. It is surrounded by heat shields to protect the vacuum vessel. The cathode is heated to up to 1700 °C, and it is made of lanthanum hexaboride ( $\text{LaB}_6$ ), which is well suited for the use as the cathode material due to its very low work function (2,7 eV). The discharge current is typically between 100 and 300 A, resulting in a discharge power between 6 kW and 21 kW.

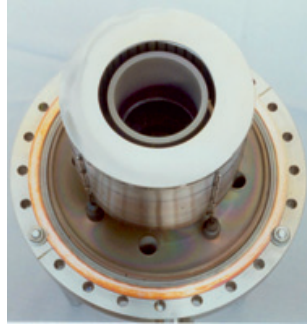


Figure 8: Cylindrical cathode

An important factor for the PSI-2 plasma is the shape of the plasma source. The reason for the cylindrical shape is the higher surface area of the cathode compared to a flat cathode: With the cylindrical shape, also the inner part of the cylinder contributes to the plasma production by the release of electrons. The drawback is the resulting profile of the plasma column, which is a hollow cylinder with high density and temperature in the edge and low density and temperature in the center. The size and shape of the hollow plasma column can be understood by simulating the magnetic field lines and tracking their position from the cathode to the target area.

In figure 9, a plot of the magnetic field lines, calculated with a simulation introduced in [31], is shown. The x-axis is the axis of the plasma column, with  $y=0$  as the center of the plasma column. It is assumed that the magnetic field lines are rotationally symmetric. The red rectangle is a crosssection of the cylindrical cathode, its quadratic appearance is due to the different scales in the plot. The magnetic field lines touching the edges of the cathode are indicated in red. As the plot shows the magnetic field lines touching the cathode propagate to the same area where the peak in the hollow plasma profile appears, between  $r=2$  cm and  $r=3$  cm. A Langmuir probe measurement which shows the location of the maximum flux is shown in figure 10. The right plot also shows a comparison to the planar cathode (figure 11). It consists of a  $\text{LaB}_6$  disk instead of a cylinder, and was designed to improve the plasma profile in PSI-2. As the plot indicates, the shape of the profile is indeed improved.

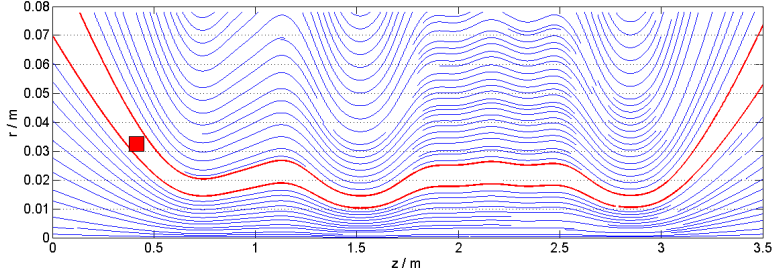


Figure 9: Magnetic field lines in PSI-2, cathode cross-section indicated in red

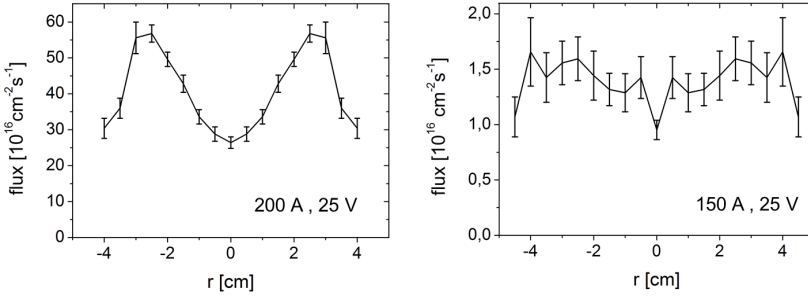


Figure 10: Ion flux profiles with cylindrical and planar cathode for argon plasmas

But the absolute flux is much lower, despite the comparable discharge parameters. The lower performance of the planar cathode is mainly caused by insufficient heating of the cathode by the used heating element. The construction of a planar cathode with a uniform plasma profile together with adequate plasma production is ongoing, but for this thesis, only the cylindrical cathode was used for plasma diagnostics and sample exposure experiments. For the plasma diagnostics by optical emission spectroscopy, the hollow profile can be transformed to a spatially resolved signal with an inverse Abel transformation (section 3.3). For sample exposure experiments, the high flux values in the edge of the plasma profile are important to reach conditions closer to reactor-relevant fluxes and to keep the duration of the plasma exposure to a reasonable time. Therefore, also the size of the sample is limited by the plasma profile; it should not exceed more than 1.5 cm in front surface diameter.



Figure 11: planar cathode

### 3.2 Langmuir probe

The main tool for the measurement of the plasma parameters (electron density and temperature) in PSI-2 is the Langmuir probe. It is a double probe design with two cylindrical tungsten electrodes of 1,55 mm in diameter and length. The electrodes are embedded in a cylindrical probe body made out of ceramic material. Alternatively, the probe can also be used as a single probe for measuring the plasma potential [32].

For the standard case with the double probe setup, the probe is connected to a AC power supply which applies a voltage of -40 to 40 V at 50 Hz to the double probe. This voltage and the resulting current are recorded by a data acquisition PC with a resolution of up to 100 kHz. While the data is recorded, the probe is either positioned at a fixed location in the plasma, or moved from outside the plasma to the center of the plasma column and back. The second method is preferred because it minimizes the time for the probe body being exposed to the plasma, which enables the Langmuir probe to measure plasma parameters also in high power discharges. If the probe is moved manually to a fixed position in the plasma, a high exposure time and the risk of overheating the ceramic body of the Langmuir probe is unavoidable.

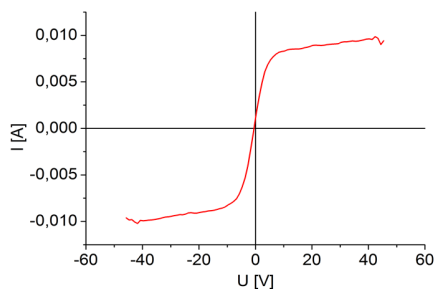


Figure 12: I-V characteristic

Each period of the recorded voltage and current represents one I-V characteristic of the Langmuir probe. An example of such a measured I-V characteristic is displayed in figure 12. From this characteristic the ion saturation current  $I_{sat}$  can be deduced. The slope of the curve at the origin is [33]:

$$\frac{dI}{dV} = I_{sat} \cdot \frac{e}{2k(T_e + T_i)} \quad (1)$$

With this equation the electron temperature can be calculated. The electron density follows as

$$n_e = \frac{I_{sat} \cdot e}{A} \cdot \sqrt{\frac{k(T_e + T_i)}{m_i}} \quad (2)$$

with  $m_i$  as the ion mass. The dependency on the ion mass results in an uncertainty if the ion mass is not known, which is the case for plasmas with molecular ions or mixtures of different elements. The relative concentrations of D, D<sub>2</sub> and D<sub>3</sub> were measured by an in-situ plasma mass spectrometer in PSI-2. The results from these measurements show that the deuterium plasma consists mostly out of atomic ions. The average ion mass used for the calculations is estimated to be 2.2 u based on these results. For mixed plasma species, the impurity ion content is measured as described in section 4.1.5 and by the ratio of ion species the average ion mass is calculated.

These simple equations for the analysis of the I-V characteristic do not take into account additional factors which could influence the Langmuir probe results, like the presence of a magnetic field [34]. Therefore a certain error in the calculated values has to be assumed. The calculation is automated by an IDL data evaluation program. This program first calculates fit curves for each period of the recorded voltage and current data. From these fit curves the plasma parameters are deduced with the formulas above.

An important value for plasma-wall-interaction experiments is the ion flux  $\Gamma_i$ , which can be measured either by the ion saturation current to the target itself, or also by the Langmuir probe. There are some reasons which make the calculation of the ion flux by the current to the target unpractical. First, the target has to be biased to a potential high enough for reaching the ion saturation current, which is not always desirable. Also, any parts of the target holder and the manipulator will contribute to the current if they are not isolated and get in contact with the plasma. This is especially the case for the target station manipulator, which is in electrical contact with the whole plasma profile. Since the plasma profile is not homogeneous, the partial ion flux cannot be calculated just by dividing the total ion flux by the ratios of the sample and target holder areas. For these reasons the Langmuir probe is

used to calculate the ion flux density. The IDL program mentioned in the previous paragraph calculates the ion flux with the following equation:

$$\Gamma_i = 0.5 \cdot n_e \cdot \sqrt{\frac{eT_e}{m_i}} \quad (3)$$

### 3.3 Optical emission spectroscopy

The passive optical emission spectroscopy is an important part of both the topic of this thesis as well as of the general purpose of PSI-2 described in section 3: The optical spectroscopy is a diagnostics method which does not need parts with contact to the plasma nor moving parts near the plasma generator. Therefore it is a preferable diagnostic for the JULE-PSI project, where maintenance inside the hot cell should be kept to a minimum. The spectrometer can be simply placed outside the hot cell, only a light path to the plasma generator is needed. The operation of the optical emission spectroscopy at PSI-2 can provide important conclusions for the usage at JULE-PSI.

On the other hand, the optical emission spectroscopy is also needed for some of the current topics investigated at PSI-2. For example, it can be used to measure surface erosion of samples from the light emission of eroded particles inside the plasma. But for this thesis, another advantage is of interest: While the Langmuir probe can measure the ion flux towards the sample, it cannot distinguish between different plasma species, which are present in plasmas with impurities. With spectroscopy, one can easily detect the different species because of their characteristic spectral lines, and also measure their relative ion concentrations in the plasma.

#### 2D imaging spectrometer

The 2D imaging spectrometer used at PSI-2 is an Acton SpectraPro-750, a 0.75 m grating spectrometer. It is equipped with an Andor Newton EMCCD Camera. The resolution of the camera is 1600x400 pixels, and the image covers 25.6 nm of the spectrum at 550 nm. Because the spectrum is reproduced along the long side of the image, the spectrum is recorded by the camera with a resolution of 25.6 nm/1600 px = 0.016 nm/px. The resolution of the Acton SpectraPro-750 spectrometer itself is 0.05 nm [35]. Due to the dispersion these values vary depending

on the selected wavelength. The spectrometer's resolution dependency on the wavelength is shown in figure 13.

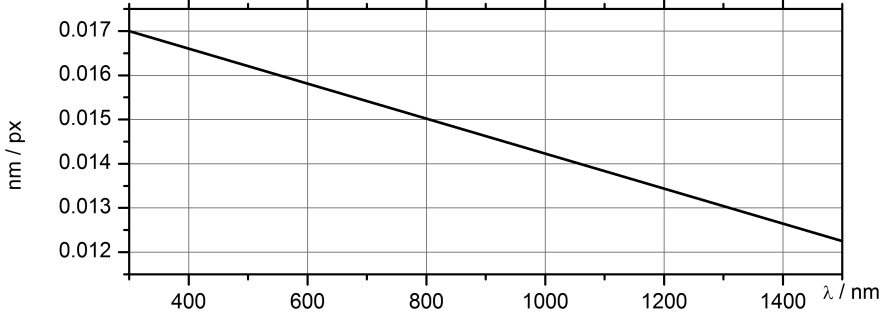


Figure 13: Dispersion of the 2D imaging spectrometer

Because the spectrometer uses a camera with a 2-dimensional sensor instead of a single row of CCD elements, there is also a spatial resolution. 10 cm in the radial direction are reproduced along the short side of the image (0.25 mm/px). The spectrometer's line of sight is perpendicular to the plasma column. This means that the whole diameter of the plasma column can be captured in a single image. An example of such an image is shown in figure 14.

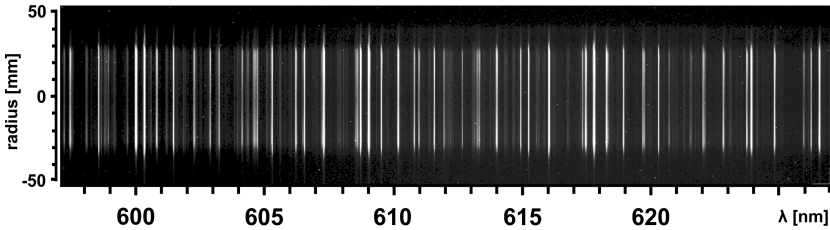


Figure 14: Fulcher Bands Q-Branch as an example for the spectrometer images

One can clearly see the extend of the plasma column from -3 to 3 cm. Alternatively, an additional mirror arrangement can be put into the line of sight, which rotates the image by  $90^\circ$ . Then, the spectrometer measures profiles along the plasma column axis, as shown in figure 15. This is especially useful when a target is introduced into the plasma. Possible applications for this arrangement are the measurement of penetration depths of eroded elements into the plasma, or the behaviour of plasma parameters directly in front of the target.

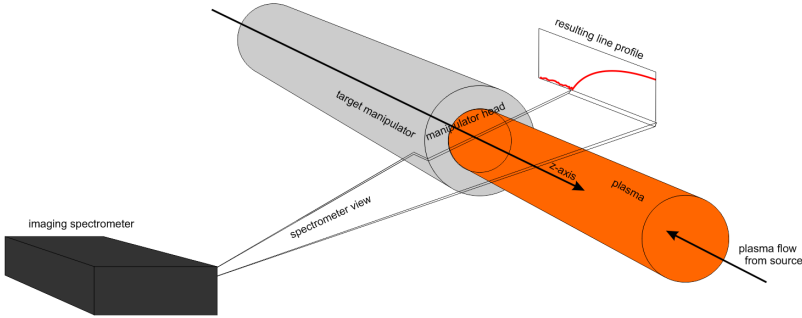


Figure 15: Spectrometer setup for the measurement of profiles along the plasma axis

### Inverse Abel transformation

A drawback of passive optical emission spectroscopy is that the measured line profiles are line-integrated intensity values. To calculate the spatially resolved profiles from the line-integrated profiles, an inverse Abel transformation method (matrix method) is used [36]. The principle of the Abel transformation is to divide the plasma column in shells. From the point of view of the spectrometer, at the top of the plasma column, only the outermost shell is touched by the line of sight. It is also touched only in one point. In this point it can be assumed that the line-integrated intensity equals the spatially resolved intensity. This intensity is then subtracted from all the inner shells. Now the shell below becomes the outermost shell, and with this its spatially resolved intensity is known. The process can be repeated until the center of the plasma column is reached. Three aspects are important for the Abel transformation:

First, the subtraction of each shell has to take into account geometrical effects. The line of sight in each shell is longer in the edge of the plasma, as compared to viewing through the center of the plasma (figure 16). With the matrix method, a triangular matrix  $A$  with the matrix elements  $\alpha_{ij}$  is constructed:

$$\alpha_{ij} = \begin{cases} 2\Delta R \left( \sqrt{j^2 - (i-1)^2} - \sqrt{(j-1)^2 - (i-1)^2} \right), & j \geq i \\ 0, & j < i \end{cases} \quad (4)$$

The matrix elements are also shown in figure 16 and represent the geometrical factors to consider the different widths of each shell at different radial positions. The spatially resolved intensity  $i$  is then obtained by multiplying the inverse of  $S$

with the measured, line integrated profile  $I$ :

$$i = S^{-1}I \quad (5)$$

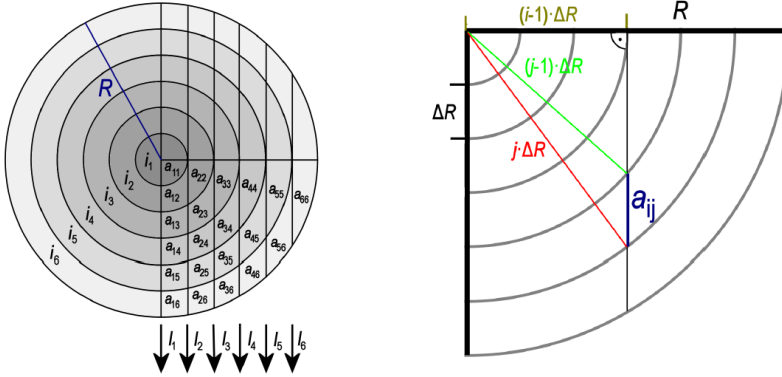


Figure 16: Inverse Abel transformation with the matrix method [37]

Second, the plasma column must be symmetric for rotations along the plasma axis, for the subtraction of the signals to give reasonable results. The plasma in PSI-2 is in general assumed to be rotationally symmetric, because all parts like the plasma source, pumping stage and magnetic field are also rotationally symmetric. But there are special situations where a non-symmetric plasma is apparent, like the non symmetrical light emission of the recombining plasma described in section 4.1.3. Thus every time when a non-symmetric plasma is appearing, the Abel transformation must not be used. Of course, this also means that the Abel transformation can only be used for radial profiles, not for measurements of profiles along the z-axis (as mentioned in the previous section).

And third, the error margins for each step of the calculations are adding up with the progression to the center of the plasma. Therefore the obtained intensity values for the center of the plasma have bigger uncertainties and noise than the values in the edge. Because of that, the line integrated plasma profile has to be a strong, low-noise signal to calculate a reasonable profile with the matrix-method.

Figure 17 shows the result of an inverse abel transformation of the  $D_\alpha$  line of a standard deuterium plasma in PSI-2. Even in the line integrated signal, the hollow profile of the plasma is already visible, but the local intensity result reveals that there is only low light emission in the center of the plasma. As mentioned earlier in

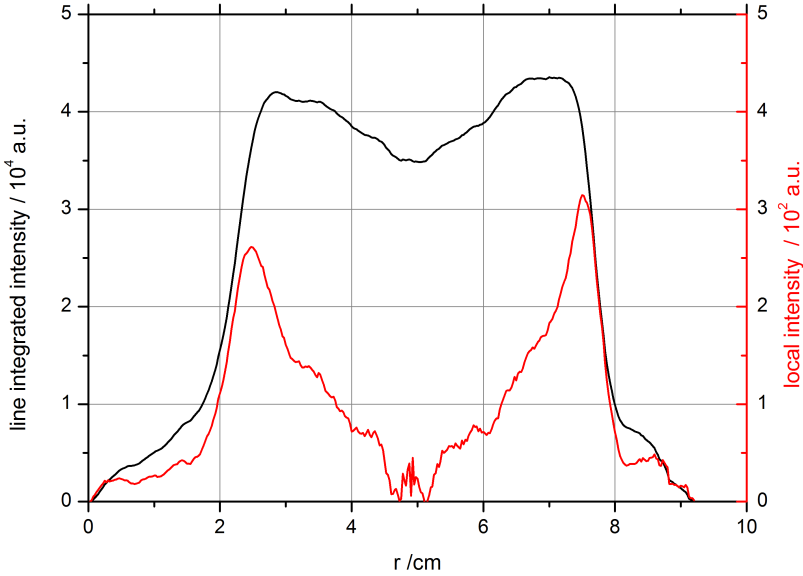


Figure 17: measured signal and inverse abel transformed signal of the  $D_\alpha$  line

this section, the matrix method only calculates the inverse abel transformation from the edge to the center of the plasma. To transform both sides of the plasma profile, the profile is splitted in two parts and both are transformed separately. The fact that both transformed parts can be merged together at the center, as well as the similar shape of both parts, show that the matrix method gives reliable results. But the amplitude of both edge peaks varies slightly. This might be due to a not exactly symmetric plasma. Although the inverse abel transformation needs a rotationally symmetric plasma, an asymmetry of such low extends might be still acceptable. Also, stronger noise effects are visible in the center of the plasma profiles. Here, a smoothing of the calculated profiles should be applied, because this effects are most likely not real fluctuations, but noise due to the inverse abel transformation, as it was predicted.

### Intensity calibration

For some of the spectroscopic methods described in the next sections, an absolute calibration of the measurements is required. This is done by a reference measurement with an Ulbricht sphere. This sphere gives a uniform light emission along its exit

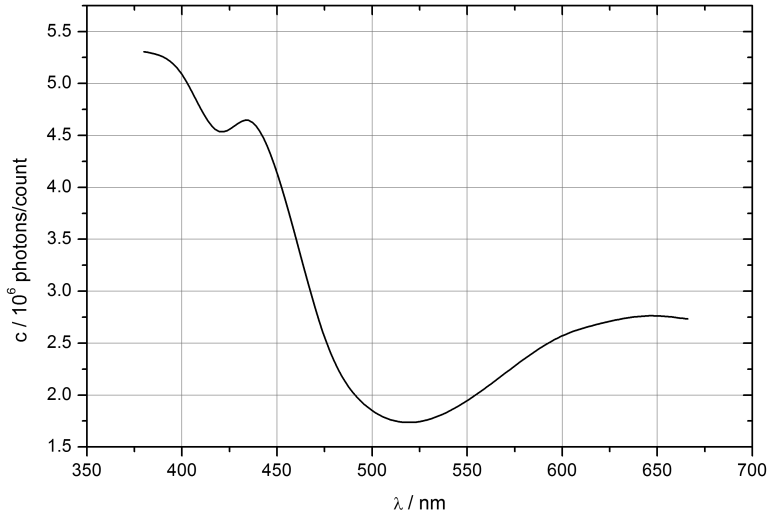


Figure 18: Calibration factors of the 2D imaging spectrometer

window, and more importantly, the emitted light intensity from 300 nm to 800 nm is known. With this, the sensitivity of the spectrometer system can be calculated from the reference measurement. Figure 18 shows the result of the calibration for the visible range.

### 3.4 Target manipulators

To bring the samples into contact with the plasma column, they have to be moved and held in the required exposure position with a target manipulator. Currently there are two target manipulators in use: The side manipulator and the target station manipulator. Both are described in detail in the next two sections.

#### Side manipulator

The side manipulator is the smaller sample manipulator at PSI-2 and is located at the middle position of the target area, opposite to the spectroscopy observation window (figure 19).

When the sample holder is moved out of the main chamber of PSI-2, the vacuum vessel of the side manipulator can be closed off with a gate valve and vented separately for the sample mounting/dismounting. The sample holder of the side manipulator consists of a small copper holder with internal water cooling, and a ceramic coating for isolation to the plasma. The samples for the side manipulator sample holder must have a small pin on their backside for mounting, as it is visible in figure 20, which shows a typical tungsten sample for the side manipulator.

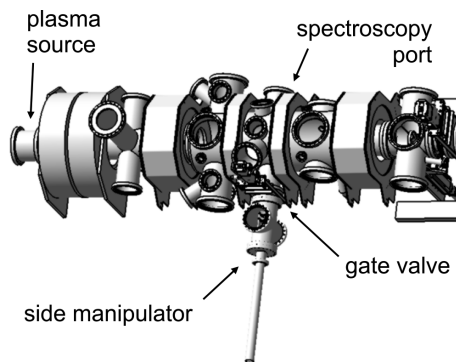


Figure 19: The position of the PSI-2 side manipulator

Figure 21 shows the holder with a sample in a deuterium plasma. As the name suggests, it is arranged perpendicular to the plasma column. Because of that, there is no possibility to change the distance from the sample to the plasma source, but on the other hand, it is very easy to change the radial position of the sample. This is a useful feature when aligning the position of the sample to the edge of the plasma column, where density and temperature are peaked. Although it is possible, it is not advisable to bring the samples to the center of the plasma column, because the

sample holder itself is then exposed to the edge of the plasma column and could be damaged. In figure 21, an orange glow in the plasma below the target holder can be observed.

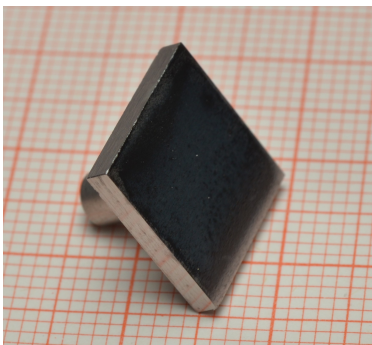


Figure 20: Tungsten sample for the side manipulator sample holder

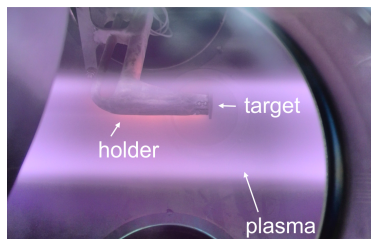


Figure 21: The PSI-2 side manipulator sample holder with a sample in a deuterium plasma

This is due to sputtering of the ceramic coating by the plasma. While the holder is mostly shadowed from the plasma by the sample, the bottom part of the holder has a more direct contact to the plasma flux because of the counter-clockwise (seen from the plasma source) rotation of the plasma. The holder is coated for electrical isolation in the case of a biased sample. The sample can be biased negatively to increase the energy of the ions hitting the sample surface. This is done by biasing the whole copper holder. The ceramic coating significantly reduces the current and power load on the holder. Also, with the current flowing only over the sample, which has a well-known surface, one can also calculate the ion flux onto the sample if the ion saturation current is reached. With only the ions contributing to the current flowing over the sample, one can simply calculate the ion flux based on the ion charge and surface area of the sample. Comparisons with Langmuir probe measurements have shown a good agreement on the calculated ion flux.

### **Target station manipulator**

The target station with its target manipulator is a major addition to PSI-2 which was added at FZ Jülich in 2012. Figure 22 shows a CAD drawing of PSI-2 with the new target station and target manipulator.

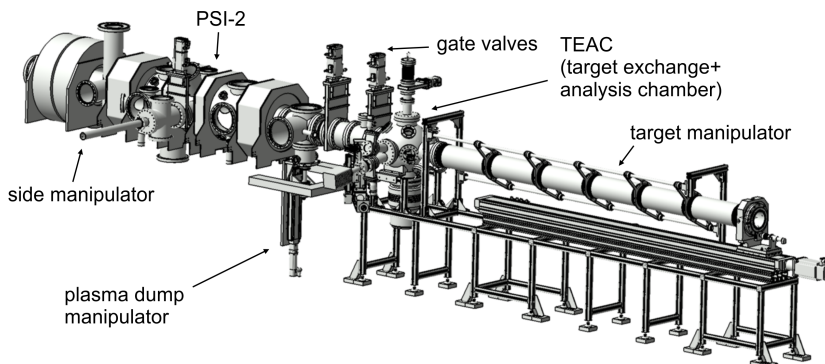


Figure 22: PSI-2 with the new target station + target manipulator

It has a range of advantages over the more simple side manipulator. The bigger target exchange and analysis chamber allows for analysis of the samples, for example by laser induced desorption, without breaking the vacuum. Also, it has a mechanism which allows the samples to be mounted to a separate holder plate, which is then plugged in a notch on the front of the sample holder, as seen in image 23. This mechanism was chosen considering the planning of JULE-PSI: It makes remote handling of the targets, which is required in the hot cell environment of JULE-PSI, considerably more simple.

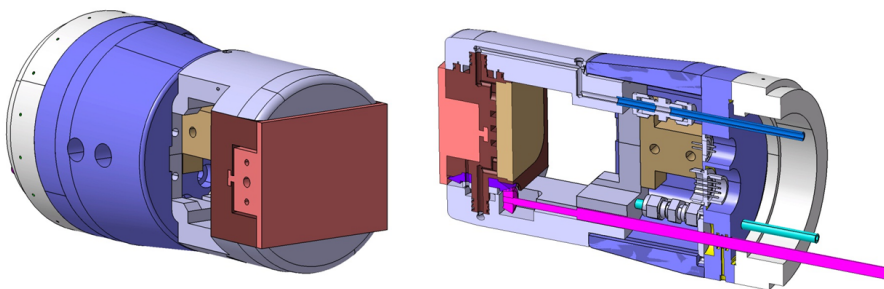


Figure 23: Target manipulator sample holder

Figure 23 also illustrates the various features of the sample holder. It can be rotated and the front part is tiltable up to  $90^\circ$ . This is primarily intended for the analysis chamber, where the samples might have to be facing towards diagonal or side ports for analysis methods. Because of the mounting mechanism described before, the removable holder plate is not directly watercooled. To ensure the thermal

contact between the cooled part and the removable holder plate, there are metal lamellae between them, which accomplish a good thermal contact without pressing the parts together by screw mounts. There are also electrical connections for thermocouples or heating elements on the holder plate, and a gas inlet which allows for example gas puffing experiments during the plasma exposure.

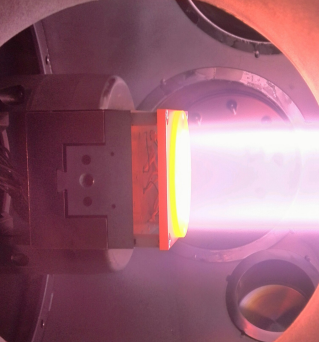


Figure 24: Sample exposure at 900 °C

With the heating element and the greater flexibility in mounting the samples, a bigger variation in the sample temperature can be reached than with the side manipulator. Even without using a heating element, high temperatures of more than 1000 °C can be reached by lowering the thermal contact between the samples and the holder. This can be done by changing the mounting pressure of the mask, decreasing the area of the graphfoil which touches the sample, or adding additional layers of graphfoil between the samples and the holder. There is also a special holder which has the mounting plate separated by the cooled part of the sample holder

with distance pins. A sample exposure with this sample holder is shown in figure 24.

## Bias voltage

A very important factor for the exposure of targets to a plasma is the incident ion energy. In most cases, the targets in PSI-2 are biased. This allows to provide a defined and mono-energetic incident ion energy. In the sheath in front of the sample, the plasma ions are accelerated towards the sample because of the potential difference of the plasma ( $\Phi_p$ ) and the sample, which might be at floating potential ( $\Phi_f$ ) or at an externally biased potential. The floating potential of the sample is always at a lower potential than the plasma. This is due to the higher velocities of the electrons in relation to the ions, which leads to a higher ratio of electrons reaching the sample. The electrons charge the sample, up to the point where the electron and ion current are equal, which is the floating potential. If the sample gets biased externally, the sample potential is decreased even more, which increases the incident ion energy and current (the current being limited to the ion saturation

current). But in contrast to the sample potential, the plasma potential cannot be directly measured with the standard plasma diagnostic at PSI-2, the Langmuir double probe. For this reason, the plasma potential is calculated with the following equation [38]:

$$\Phi_p - \Phi_f = -\frac{kT_e}{2e} \ln \left( 2\pi\gamma \left( 1 + \frac{T_i}{T_e} \right) \frac{m_e}{m_i} \right) \quad (6)$$

This gives the difference between the plasma potential and the floating potential, with  $\gamma = 5/3$  as the adiabatic coefficient. The ion temperature for a standard deuterium plasma in PSI-2 ( $n_e = 1 \cdot 10^{12} \text{ cm}^{-3}$ ,  $T_e = 10 \text{ eV}$ ,  $p_{D_2} = 5 \cdot 10^{-2} \text{ Pa}$ ) is known from spectroscopic measurements to be  $T_i = 3 \text{ eV}$ . Also, the floating potential of the sample can be measured,  $\Phi_f = -50 \text{ V}$ . With these parameters, the plasma potential calculated with equation 6 is  $\Phi_p = -20 \text{ V}$ . Usually one would expect a positive plasma potential; but in PSI-2 with its arc discharge as the plasma source, negative plasma potentials can occur due to enhanced thermalization of the primary electrons in the plasma [39]. Now the ion energy can be calculated as the difference between the bias potential  $\Phi_b$  (or the floating potential) and the plasma potential:

$$E_i = z \cdot e \cdot (\Phi_b - \Phi_p) \quad (7)$$

For deuterium, the charge of the ions  $z \cdot e$  is always  $1e$ . The inertial thermal energy from the ions in the plasma can be neglected because it is low compared the bias potential applied for the experiments of this thesis.

### 3.5 Thermal desorption spectroscopy

To analyze the deuterium content of samples after plasma exposure, there are different methods available. In the scope of this thesis, the thermal desorption spectroscopy was the main tool to measure the deuterium content of exposed samples. With the TDS analysis, the exposed sample is placed into a small vacuum chamber which is equipped with a heating element. With this element the sample is heated up with a (ideally) linear temperature ramp. When the deuterium atoms in the trapping sites gain enough energy by this heating, they can get detrapped. Then the deuterium atoms are desolved in the metal lattice and can diffuse through the lattice. The diffusivity at the present elevated temperatures is much larger than at room temperature (see section 2.1). Therefore the deuterium atoms quickly reach the sample surface, where they can recombine and leave the surface as  $D_2$  molecules. This results in an increased deuterium concentration in the vacuum chamber, which

is detected by two quadrupole mass spectrometers. One of them is a high resolution mass spectrometer, which allows the separation of the small mass difference between  $D_2$  molecules and helium. By this method the amount of released deuterium, and by the temperature resolution also the desorption energy of the trapped deuterium, can be measured. All TDS measurements were performed with a heating ramp of 0.4 K/s from room temperature to 1000 °C. Figure 25 shows the raw data of the quadrupole mass spectrometer signal for mass 4 and the temperature measurement, recorded during the TDS measurement of a tungsten sample exposed to deuterium plasma (sample A-1 in table 2) The graph confirms that the heating ramp is suf-

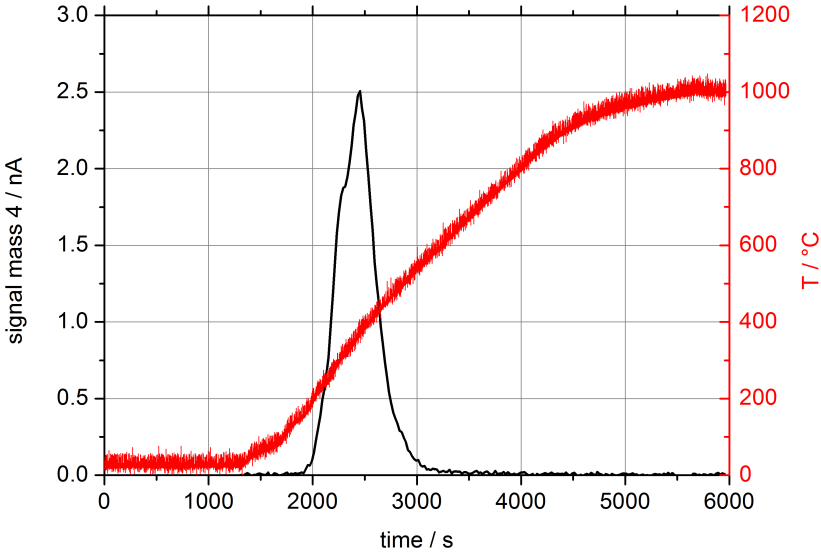


Figure 25: QMS signal for mass 4 and temperature versus time

ficiently linear in the range between 100 °C and 700 °C. For all other samples the same heating ramp was used.

While the total amount of deuterium is easily calculated by the integrated deuterium desorption, the calculation of the trapping energy is more complicated. In [40], several methods to deduce the trapping energies from TDS spectra are compared. The general equation for the deuterium desorption rate in the TDS system with a linear heating ramp is

$$\frac{dN(T)}{dT} = -\frac{\nu_0}{\mu} (N(T))^m \exp(-E_D/k_B T) \quad (8)$$

as given in [40].  $N$  is the number of trapped deuterium,  $\nu_0$  is a rate constant for the desorption,  $\mu$  is the heating rate in K/s,  $T$  is the temperature and  $m$  is the order of reaction.

The method which appears to be most accurate is the variation of the heating rate. Here the TDS spectra are recorded with different heating rates, which results in a variation of the peak temperature. The resulting desorption activation energy  $E_D$  can be calculated by the following equation [40]:

$$\ln\left(\frac{T_p^2}{\mu} / \frac{T_{p,0}^2}{\mu_0}\right) = \frac{E_D}{k_B} \frac{1}{T_p} + \frac{E_D}{k_B \nu_0} / \frac{T_{p,0}^2}{\mu_0} \quad (9)$$

As the equation shows,  $E_D$  can be deduced from the slope of the plot of  $\ln\left(\frac{T_p^2}{\mu} / \frac{T_{p,0}^2}{\mu_0}\right)$  vs.  $1/T_p$ . Here,  $T_p$  is the temperature at which the peak in the TDS spectrum occurs.  $\frac{T_{p,0}^2}{\mu_0}$  is a normalization factor which is needed to form a dimension-less value for the natural logarithm. It can be chosen freely for the calculation of the desorption energy by the slope of the plot, because the factor has no influence on the slope:  $\ln(a/c) - \ln(b/c) = \ln(a) - \ln(b)$ .

This method is expensive in that it requires several samples which have been exposed under identical conditions. This is not always possible and would also increase the effort for experiments which involve exposures with variation of certain exposure parameters dramatically. So in this case, methods which only require a single TDS spectrum may be preferred. There are several methods to analyze a single TDS spectrum. In [40], the so-called peak area analysis has been identified as the most accurate one. Here, two temperatures are chosen with  $T_1 < T_p < T_2$  and an equal desorption rate (equation 8) for both temperatures:

$$\nu_0 N_1^m \exp(-E_D/k_B T_1) = \nu_0 N_2^m \exp(-E_D/k_B T_2) \quad (10)$$

An example for a single peak desorption spectrum is given in figure 26. This gives the desorption energy as follows:

$$E_D = \frac{m k_B T_1 T_2}{T_1 - T_2} \ln\left(\frac{N_2}{N_1}\right) \quad (11)$$

Although this method is identified as relatively accurate, it only works for single peaks. In reality, often more than one peak appears in a thermal desorption spectrum, and they are also overlapping. If the single peaks are still separable, the single peaks can be reproduced by peak fitting. The peak fitting can introduce additional errors which increase the error of the desorption energy.

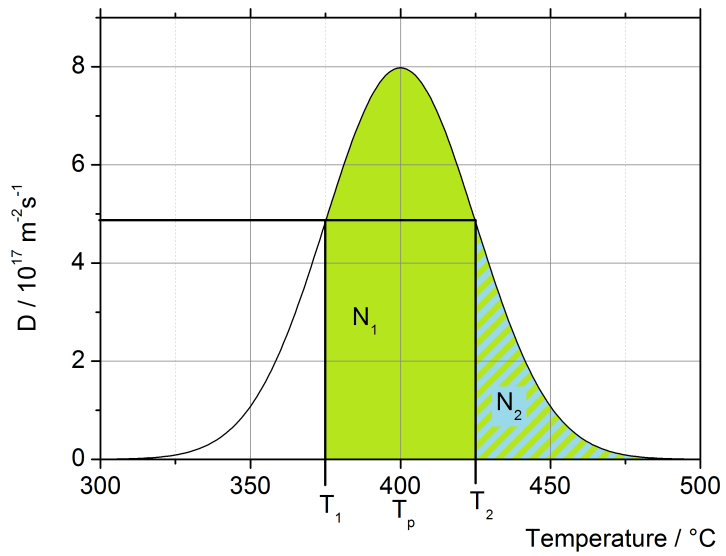


Figure 26: Graphic representation of the parameters required for the peak-area method

## 4 Experimental results

### 4.1 Plasma characterization by optical emission spectroscopy

In the following sections, the results of the optical emission spectrometry measurements regarding electron temperature, electron density (also in comparison to Langmuir probe measurements) and impurity ion concentrations are shown.

#### 4.1.1 Electron density: Balmer line ratios

The spectral lines of the Balmer series are the most prominent spectral lines in a hydrogen- (respectively deuterium-) plasma. They originate from the transition of atomic shell electrons from the energy levels  $n = 3, 4, 5, \dots$  to  $n = 2$ . They are also called  $H_\alpha$ ,  $H_\beta$ ,  $H_\gamma, \dots$  for the transitions  $n = 3, 4, 5, \dots \rightarrow 2$  respectively.

The measurement of the electron density by Balmer line ratios relies on the fact

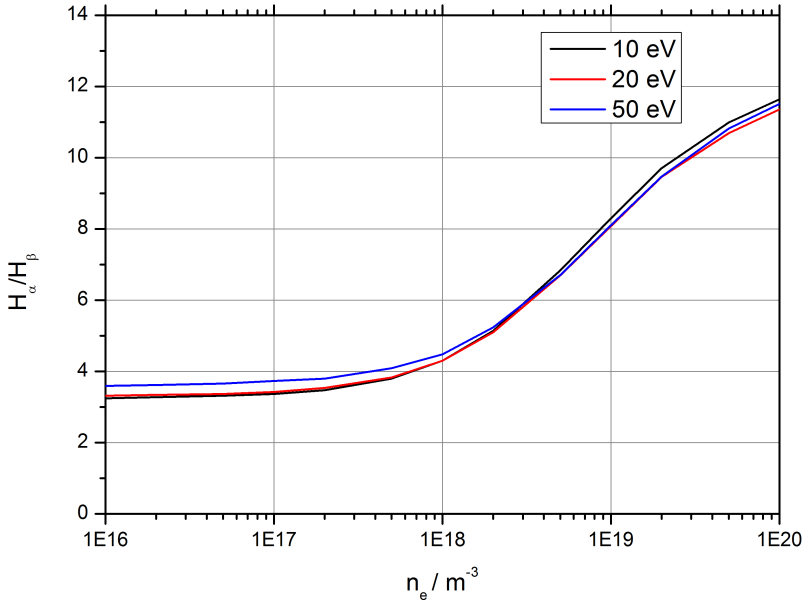
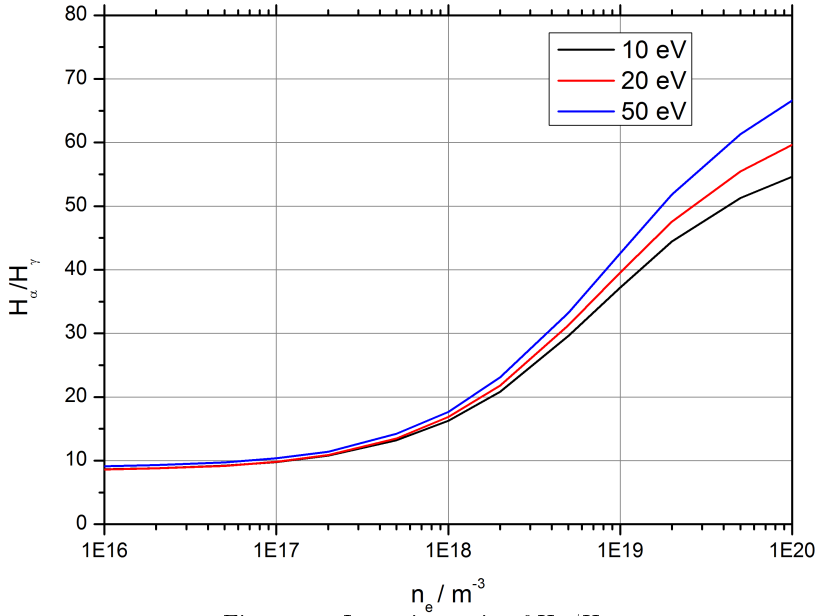
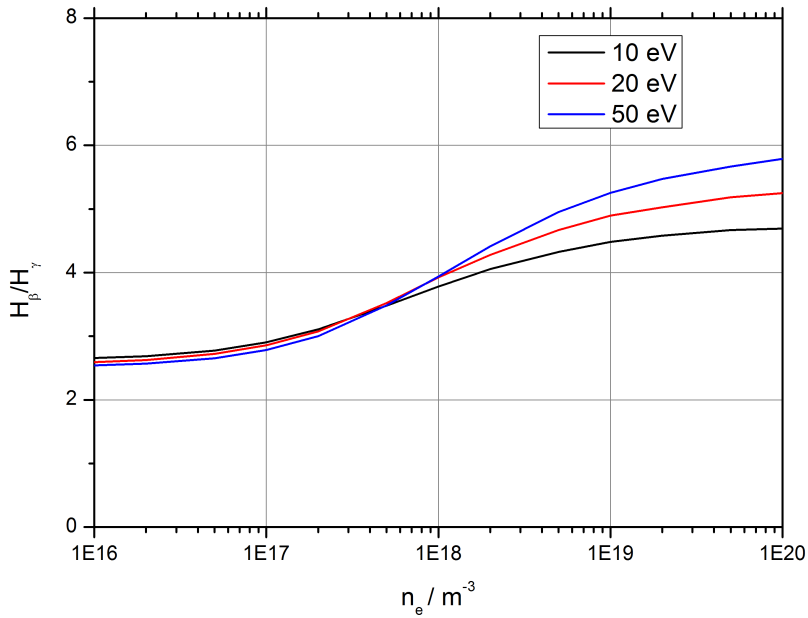


Figure 27: Intensity ratio of  $H_\alpha/H_\beta$

that the ratios are dependent on the electron density and temperature of the plasma.

Figure 28: Intensity ratio of  $H_{\alpha}/H_{\gamma}$ Figure 29: Intensity ratio of  $H_{\beta}/H_{\gamma}$

The measurements of the line ratio  $D_\alpha/D_\gamma$  are compared with theoretical values. These values are deduced by calculating the ratios of PECs (photon emissivity coefficients) from the ADAS database, which contains values for  $H_\alpha$ ,  $H_\beta$  and  $H_\gamma$  calculated by a collisional-radiative model [41]. Preferably, a ratio which depends not or only slightly on  $T_e$  is used, because then the knowledge of the exact electron temperature is not needed to calculate the electron density. While all ratios of  $H_\alpha$ ,  $H_\beta$  and  $H_\gamma$  are depending on the electron density in the region of interest ( $n_e = 10^{17} - 10^{19} \text{ m}^{-3}$ ,  $T_e \approx 10 \text{ eV}$ ), the ratios  $H_\alpha/H_\gamma$  and  $H_\beta/H_\gamma$  are not depending on the electron temperature.

Figure 27, 28 and 29 show the theoretical values for the intensity ratios of  $H_\alpha/H_\beta$ ,  $H_\alpha/H_\gamma$  and  $H_\beta/H_\gamma$ . One can see that  $H_\beta/H_\gamma$  is not suited to calculate the electron density without knowing the exact value of  $T_e$  also. Although  $H_\alpha/H_\gamma$  shows some dependency on  $T_e$  for  $n_e \geq 10^{18} \text{ m}^{-3}$ , it was chosen over  $H_\alpha/H_\beta$  because of its stronger variation with  $n_e$  for  $n_e \leq 10^{18} \text{ m}^{-3}$ . In figure 30, the results for the electron density profiles (lines) in a deuterium plasma with 4 different discharge powers are shown and compared to Langmuir probe measurements (points). As expected, the electron density rises with increasing discharge power. The comparison with the Langmuir probe measurements shows that the calculation of the electron densities by the  $H_\alpha/H_\gamma$  ratio gives results which are in good agreement with the Langmuir probe, especially in the edge of the plasma where the density is at the maximum. In the center of the plasma column the deviations are bigger, supposedly because of the required inverse Abel transformation of the line profiles, which leads to bigger errors in the center of the plasma (see 3.3). There are no datapoints available in the center of the plasma column for the high power discharges. This is because the Langmuir probe was operated with a fixed location in the plasma for these measurements, which leads to overheating of the ceramic probe body if the langmuir probe is put to deep into the plasma.

In general, the Balmer line ratios method gives reliable informations about the electron density profiles in standard deuterium plasmas in PSI-2 ( $n_e \approx 10^{18} \text{ m}^{-3}$ ,  $T_e \approx 10 \text{ eV}$ ). However, there are special cases like recombining plasmas with very low electron temperatures, in which the calculations from the ADAS database are not valid anymore. For these cases, another method for determination of the electron density is introduced, which is described in section 4.1.3.

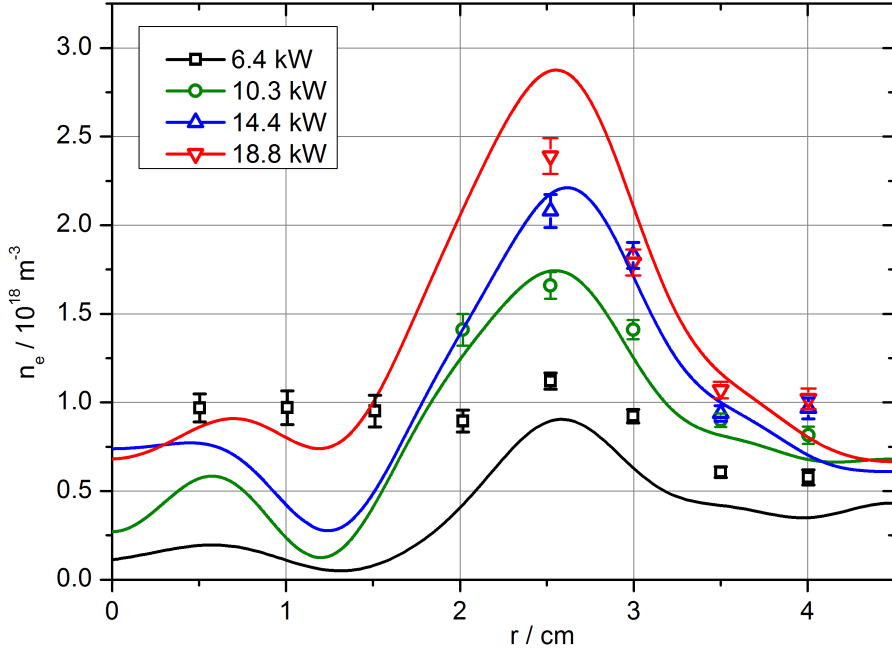


Figure 30: Electron density profiles by  $H_\alpha/H_\gamma$  (lines) and Langmuir probe (points)

#### 4.1.2 Electron density: Fulcher band lines

The following method for determination of electron density was already used at the TEXTOR tokamak. Here it was experimentally shown that the rotational temperature  $T_{rot}$  of  $D_2$  excited molecules ( $3p^3\Pi_u$ ) depends linearly on the electron density [42]:

$$T_{rot}[\text{K}] = 3.0(\pm 0.4) \cdot 10^{-11} n_e [\text{cm}^{-3}] + 0.5 \cdot T_{gas}[\text{K}] + 137, \quad (12)$$

with  $T_{gas}$  as the neutral gas temperature. If  $T_{gas}$  and the rotational temperature of the  $D_2$  molecules  $T_{rot}$  is known,  $n_e$  can be calculated. The rotational temperature is deduced from the Fulcher- $\alpha$  band emission lines at 600 nm, which occur due to the transition between the excited molecular states  $3p^3\Pi_u \rightarrow 2s^3\Sigma_g^+$  [43]. An example of these lines measured in PSI-2 is given in figure 31. To calculate the rotational temperature, a Boltzmann plot is used, as shown in figure 32. Therefore it has to be assumed that the population follows a Maxwell-Boltzmann distribution. In this case the temperature is a measure of the population.

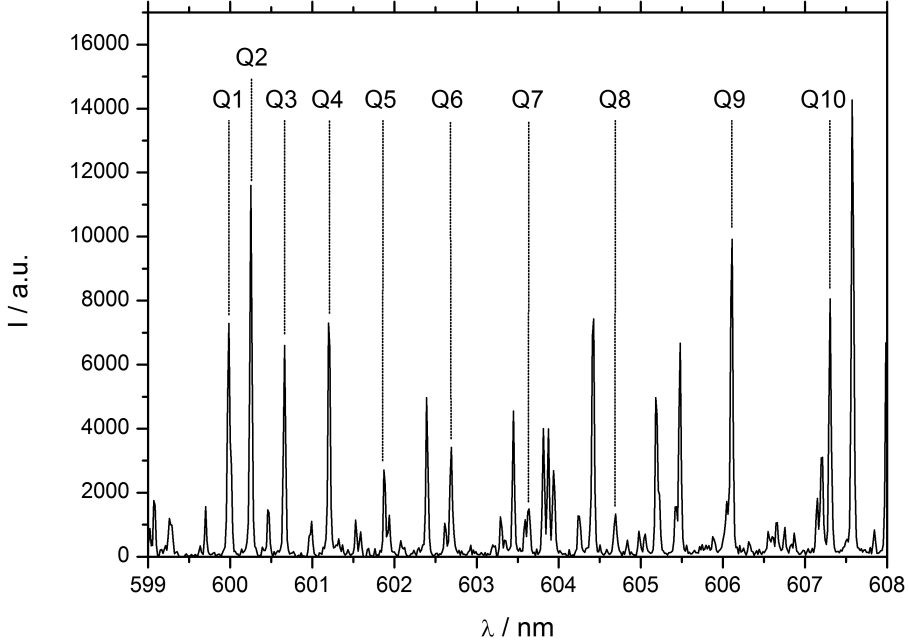


Figure 31: Fulcher Q(0-0) band emission lines

After the calculation of  $T_{rot}$  for the plasma in PSI-2, the linear dependency as found in TEXTOR can be checked. Because the gas temperature depends on the conditions in the plasma source and is not measured, the electron density cannot directly be calculated with equation 12. Instead a separate relationship between  $T_{rot}$  and  $n_e$  is shown for PSI-2, by measuring both  $T_{rot}$  (as described before) and  $n_e$  (by Langmuir probe) and plotting the relation. Figure 33 shows this plot and the comparison to the linear relation in TEXTOR [44], calculated with two different gas temperatures. The plot gives only the peak values of the density in the edge of the plasma. A full radial profile of the electron density could not be given with this method, because the inverse Abel transformation of the radial line profiles of the Fulcher band emission lines revealed that there is no light emission of these lines in the center of the plasma. This is due to the lower electron density and temperature (the upper level ( $3p^3\Pi_u$ ) of the Fulcher band transition is at 14 eV) in the center of the plasma. The comparison shows that there is no linear relation between  $T_{rot}$  and  $n_e$ . Two factors might lead to a more complicated relation: First, the gas temperature is not known and might also change with increasing discharge power,

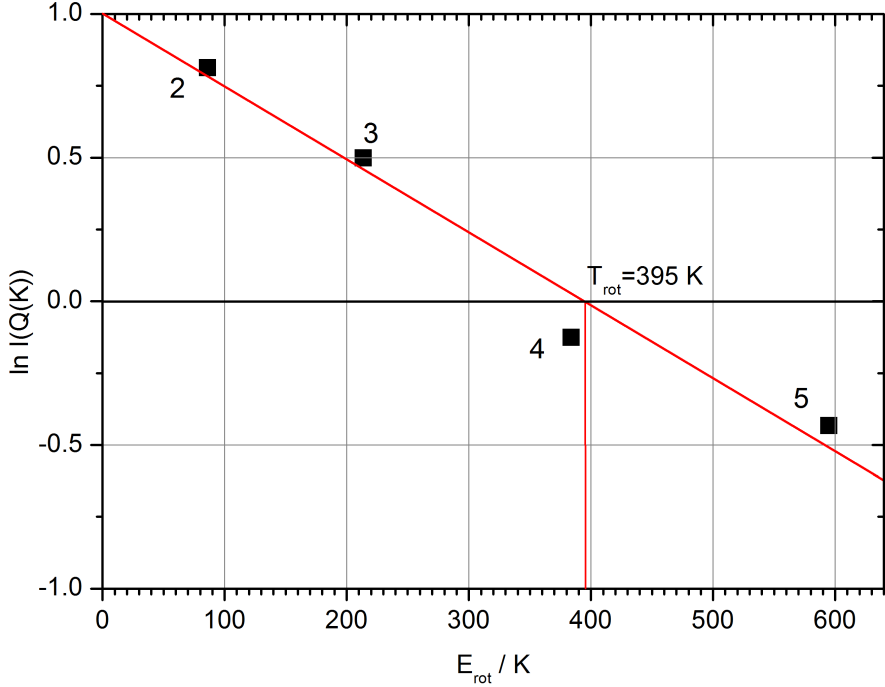


Figure 32: Boltzmann plot of the Fulcher Q2 - Q5 lines

with the discharge power being the factor which was varied in this experiment to get the different electron densities. In fact,  $T_{rot}$  is often used to calculate the gas temperature in plasmas with low electron temperatures [45]. Therefore, the result from figure 33 supports the assumption that the gas temperature changes and cannot be assumed constant in this range, as it was done for the TEXTOR measurements. And second, as mentioned before, the upper level of the Fulcher band transition ( $3p^3\Pi_u$ ) is at 14 eV, therefore in plasmas with  $T_e = 10$  eV and less, the electron temperature might also have a big impact on the calculated rotational temperature. For the TEXTOR experiments that showed the linear relation between rotational temperature and electron density, the electron temperatures were always above 30 eV. These temperatures are not reached in the experiments at PSI-2 shown here. In conclusion, the results show that the rotational temperature of deuterium molecules cannot be used to calculate the electron density for standard deuterium plasmas in PSI-2. Eventually, future experiments at PSI-2 will allow to increase the operational range to higher electron temperatures, where this method could yield suitable results.

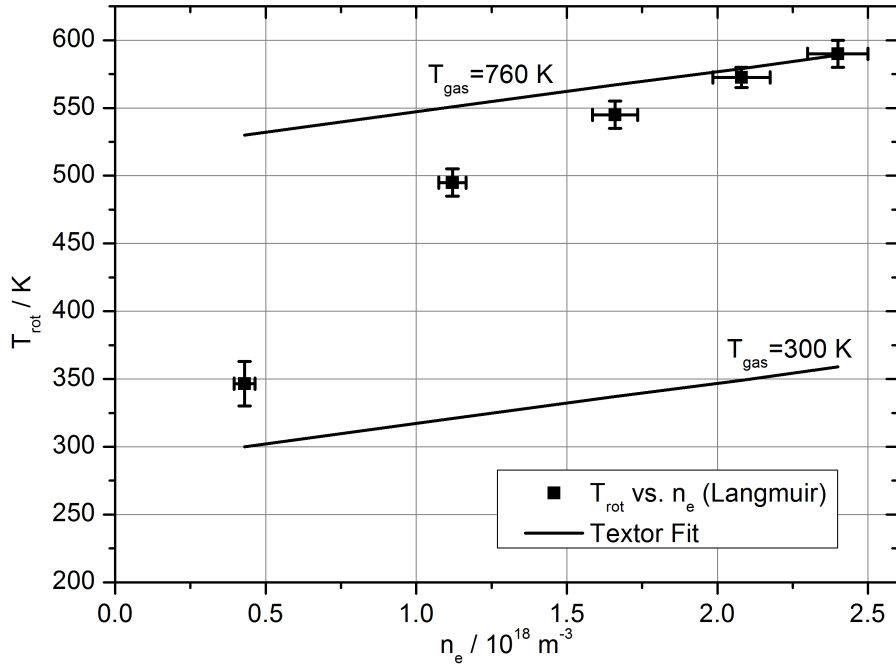


Figure 33: Rotational temperature as a function of electron density for TEXTOR and PSI-2

#### 4.1.3 Electron density: Paschen line Stark broadening

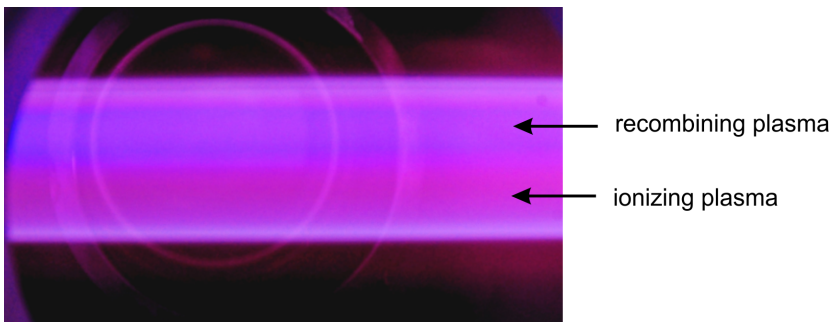


Figure 34: Recombining deuterium plasma in PSI-2

In this section, a method to measure the electron density in a recombining plasma is introduced. In a recombining plasma the recombination rate of ions and electrons

to neutral atoms is particularly high relative to the ionization rate, this is achieved by low electron temperatures and high densities in the plasma. Because of the high recombination rate and low electron temperatures, spectral lines like the Paschen series ( $n = 4, 5, 6, \dots$  to  $n = 3$ ) get more intense. When an ion is recombining, it captures an electron at an excited state, followed by a de-excitation of the electron to the ground level. One of these steps might be a transition of the Paschen series, and because in a recombining plasma the recombination and thus the population of the high energy levels is increased, also the emission of light from the Paschen series lines is increased. This also results in stronger emission from Balmer series lines with high energy levels (=shorter wavelength), thus shifting the colour of the plasma from pink to blue (figure 34).

The electron density is now calculated with the relation between the Stark broadening of the Paschen line  $10 \rightarrow 3$  and  $n_e$  [46]:

$$\Delta\lambda \text{ [nm]} = 6 \cdot 10^{-11} n_e \text{ [cm}^{-3}]^{\frac{2}{3}} \lambda \text{ [nm]}^2 u^2 \frac{1}{Z} \quad (13)$$

The Stark broadening is the broadening of spectral lines due to the presence of electric fields, in this case electric microfields by electrons and ions. In equation 13, it is shown that the Stark broadening  $\Delta\lambda$  depends on  $n_e$ , the wavelength of the observed line  $\lambda$ , the principal quantum number of the upper state  $u$  and the atomic number  $Z$ . It is obvious why a Paschen line was chosen: Due to its longer wavelength it has a more pronounced Stark broadening than Balmer lines. Likewise, the application to a recombining plasma allows to apply the method to a line with a higher principal quantum number of the upper state, also increasing the Stark broadening. Under this circumstances the Stark broadening with electron densities of  $10^{18} \text{ m}^{-3}$  is bigger than the resolution of the spectrometer (0.016 nm/px), making the Stark broadening observable. A possible additional mechanism for the line broadening is the Doppler broadening, depending on the temperature of the plasma. For temperatures below 1 eV (see section 4.1.4) the Doppler broadening is sufficiently smaller than the Stark broadening and therefore being neglected in the following results. Figure 35 shows the results for the electron density in recombining plasma in PSI-2. The recombining plasma was produced by puffing neutral deuterium gas into the target chamber, which leads to a loss of electron energy by inelastic collisions between electrons and molecules. The cold electrons then show an enhanced recombination rate. The plot shows the variation of the electron density in the recombining area with the increasing neutral gas pressure in the target chamber. It is observed that the density decreases with increased recombination, as one would expect. The measurements were done at 2 different z-Positions of the target chamber, with  $z=1.5 \text{ m}$

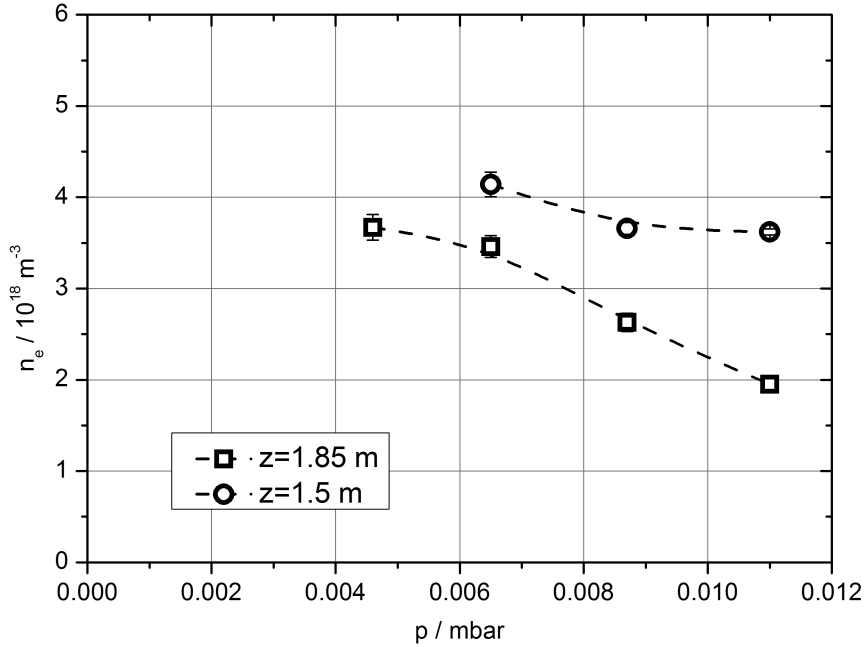


Figure 35: Electron density in a recombining deuterium plasma in PSI-2 under variation of the neutral gas pressure and at 2 different axial positions

and 1.85 m as the distance to the plasma source. For the closer position, a higher electron density is expected, because the recombination effect progresses also along the  $z$ -axis, increasing with the distance to the plasma source. The results confirm this assumption. The data point for  $z=1.5$  m and the lowest pressure is missing because the treated Paschen line was not observable under this circumstances.

#### 4.1.4 Electron temperature: Paschen lines ratio

This method for calculating the electron temperature from Paschen line ratios works in the same way as calculating the electron densities from balmer line ratios in section 4.1.1. Several of the Paschen line ratios show a steep dependency on the electron temperature for low electron temperatures. Figure 36 shows the line ratios for the Paschen lines  $n = 9 \rightarrow 3$  and  $n = 7 \rightarrow 3$ , calculated from photon emissivity coefficients for the recombination process from the ADAS database [47]. The plot

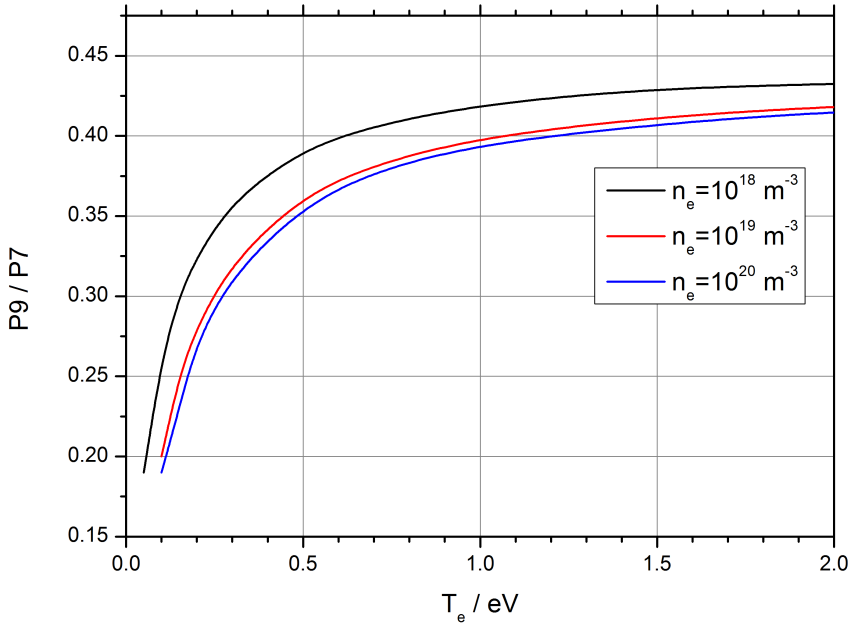


Figure 36: Ratios of the P9 and P7 line emissions for different electron densities

also shows a small dependence on the electron density. Thus, for the recombining plasma in PSI-2 with electron densities around  $1 \cdot 10^{18} \text{ m}^3$  an error due to the variation of the electron density has to be taken into account. Because the datapoints from the ADAS database only go down to 0.2 eV, the values below that temperature are extrapolated. The results in figure 37 show the calculated electron temperature for different neutral gas pressures and at the different axial positions as described one section earlier in 4.1.3. Again the temperature is higher at the position closer to the plasma source ( $z=1.5 \text{ m}$ ). The electron temperature also decreases with increasing neutral pressure, although this effect is not observed at  $z=1.5 \text{ m}$ . At this position, there were again only 2 datapoints assessable, because for lower pressures

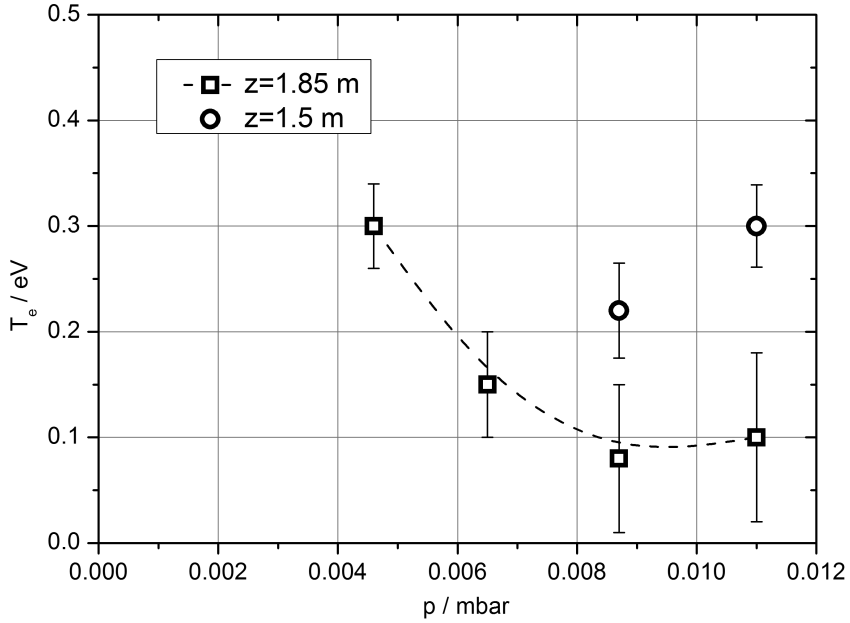


Figure 37: Electron temperature in a recombining plasma in PSI-2 under variation of the neutral gas pressure and at 2 different axial positions

the respective Paschen lines were not visible at the position close to the source. The big error bars for the very low temperatures are due to the bigger uncertainties in this range. The uncertainty in electron density has a bigger impact for very low temperatures (see figure 36), and also the Paschen ratios itself are only interpolated below  $T_e = 0.2$  eV.

### 4.1.5 Argon ion concentration

The ion flux onto plasma facing targets is an important quantity for plasma-wall interaction. While the total flux can be simply measured by the Langmuir probe, in plasmas with more than one species the individual ion flux of each species cannot be distinguished. This means that for the measurement of the impurity ion concentration another method needs to be applied. The methods described in the following two sections rely on the measurement of ion ratios by the absolute intensity of a single optical emission line of the respective plasma impurity. The method for measuring the argon ion content used here was already used at the linear plasma generator PISCES-B, as described in [48]. The observed emission line is the  $\text{Ar}^+$  line at 434,8 nm ( $4^4\text{P}-4^4\text{D}$ ). The local emissivity can be described as

$$I_{\text{Ar}^+} = \frac{\langle \sigma v \rangle_{\text{pec}} \cdot n_e n_{\text{Ar}^+}}{4\pi} \quad (14)$$

Here,  $n_{\text{Ar}^+}$  is the argon ion density, and  $\langle \sigma v \rangle_{\text{pec}}$  is the photon emission coefficient. This coefficient relates the ion density and electron density to the intensity of the respective transition. The data used for this coefficient is from the ADAS database and was particularly calculated for the application of the argon ion ratio measurements in PISCES-B [49].

One can easily see how to calculate the argon ion ratio from equation (14):

$$\frac{n_{\text{Ar}^+}}{n_e} = \frac{I_{\text{Ar}^+} \cdot 4\pi}{\langle \sigma v \rangle_{\text{pec}} \cdot n_e^2} \quad (15)$$

Thus, besides the spectral line intensity, also the electron density and the photon emission coefficient needs to be known. The photon emission coefficient itself depends also on the electron density and electron temperature. The electron density and temperature were measured with the Langmuir probe. The photon emissivity coefficients for different electron densities in dependence of the electron temperature are shown in figure 38. The graph shows a very steep dependence of the photon emissivity coefficient on the electron temperature for electron temperatures lower than about 5 eV. The uncertainty of the electron temperature measurement with the Langmuir probe is typically in the range of 1 eV. This suggests that the calculated argon ion density might show very large error bars if used on plasmas below 5 eV, where an error in the temperature measurement of 1 eV leads to a difference in the photon emissivity coefficient of more than one order of magnitude. The typical temperature for deuterium plasmas is 10 eV in PSI-2, but for pure argon plasmas it is typically below 10 eV.

This leads to an issue for this method in the next step, where equation (15) is applied

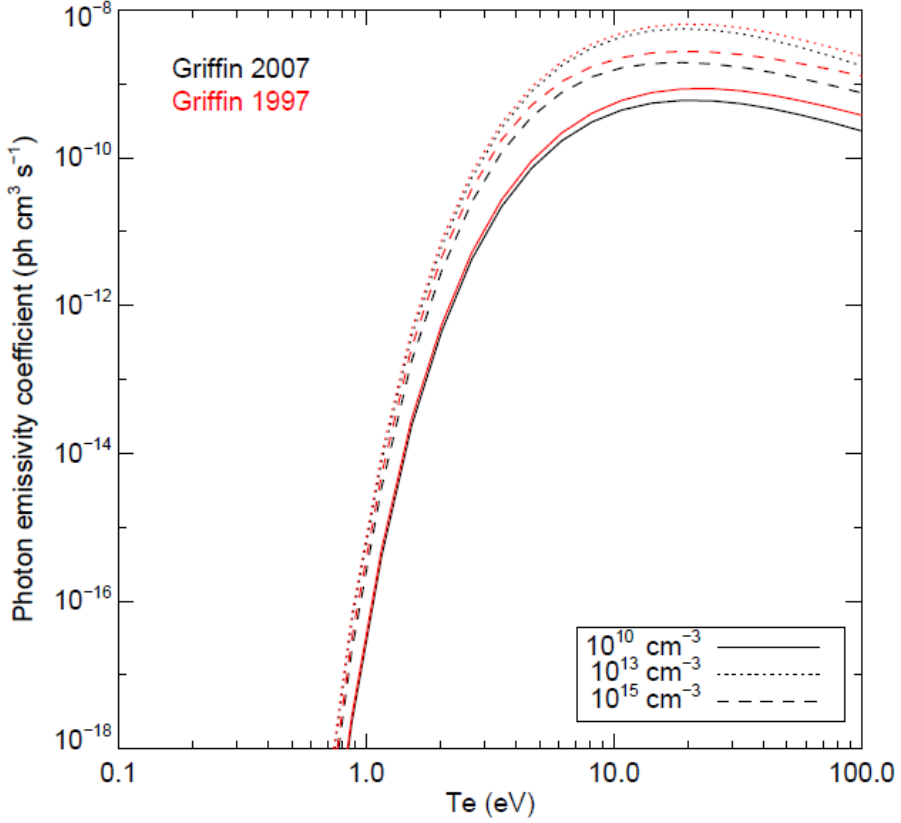


Figure 38: Photon emissivity coefficients for the 434,8 nm transition of Ar<sup>+</sup> [49]

to a pure argon plasma. With the assumption of only singly ionized argon ions in the plasma, the result of the argon ion ratio is trivial:  $n_{\text{Ar}^+}/n_e = 1$ , because of the quasineutrality of the plasma. Therefore the pure argon plasma can be used to test the validity of equation (15). Figure 39 shows the measured results of equation (15) for pure argon plasmas with a variation in electron density and temperature. Of course, the measured argon ion ratio should ideally be 1, and constant for all electron temperatures. The graph shows two problems: For low electron temperatures, the uncertainty of the values is very big; and the calculated argon ion ratio is not equal to 1. The big error bars are caused by the strong change of the photon emissivity coefficient for low electron temperatures, as mentioned before. The calculated ion ratio not being equal to 1 can have several reasons: There could be systematic errors in the calculation of the photon emissivity coefficients, respectively their ap-

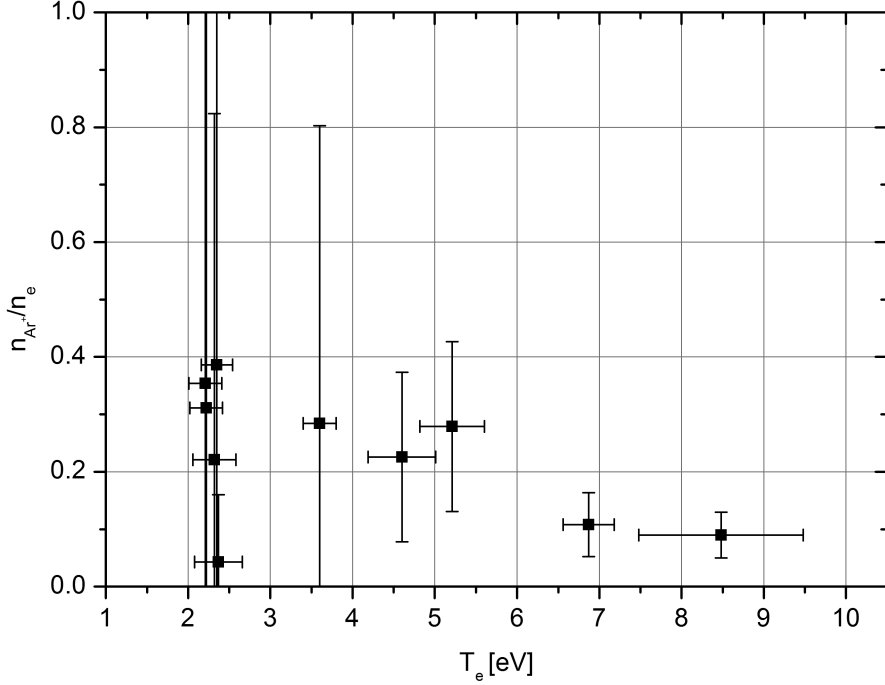


Figure 39: Argon ion ratios for a pure argon plasma, calculated with (15)

plication to the PSI-2 plasma. Or, there could be errors in the measured variables, especially in the measurement of the absolute intensity of the  $Ar^+$  line. At the end of this section, the method is calibrated by multiplying equation (15) with a certain calibration factor, to achieve a result of 100 % argon ions in a pure argon plasma. To determine this factor, only the datapoints at high electron temperatures above 6 eV are used, because they are more consistent and also more relevant for the application to mixed D+Ar plasmas. This calibration factor treats all the possible errors and effects which cause the calculated argon ion ratio to be less than 1.

A critical effect is also the presence of  $Ar^{2+}$  in the plasma, which was neglected by the previous assumption  $n_{Ar^+}/n_e = 1$ . Measurements with an in-situ mass spectrometer in PSI-2 have shown that also  $Ar^{2+}$  is present in the plasma. The ratio of  $Ar^+$  to  $Ar^{2+}$  depends heavily on the discharge power, neutral density and electron temperature. If the ratio of  $Ar^+$  to  $Ar^{2+}$  varies significantly in the parameter range which is of interest for the application to mixed D+Ar plasmas, this variation has to be taken into account for the measurements with the method introduced here. Un-

fortunately, the in-situ mass spectrometer was only available temporally and could not be used to measure the plasma composition for every condition. Therefore, the amount of  $\text{Ar}^{2+}$  which is present in the plasma under various conditions has to be estimated by theoretical calculations.

If only the ionization and recombination rates are taken into account, large ratios of  $\text{Ar}^{2+}$ , and even  $\text{Ar}^{3+}$  are expected [50]. This assumes the so-called Corona-equilibrium [51], where the ions are confined long enough to reach a stable ionization state distribution only influenced by ionization and recombination rates. This is not the case for plasmas in linear plasma generators like PSI-2: Here, the confinement time is so low that the loss of ions due to limited confinement is bigger than the loss by recombination.

To get an insight into the charge distribution of argon ions in a deuterium plasma, the transport of argon trace impurities in a deuterium background is simulated by a Monte-Carlo procedure developed at the IEK-4 institute [52]. The argon neutrals are assumed to enter a one-dimensional domain representing PSI-2 at  $z = 0$ , and the target where the particles are lost is located at  $z = L$ . The neutral particles are assumed to be cold ( $T_0 = 0.1$  eV) giving an initial velocity towards the target. Traveling along the  $z$ -direction parallel to the magnetic field the argon particles undergo ionization events, recombination events and friction with the deuterium background. Also included are the radial losses in the form of a loss rate  $\nu_{loss} = D_{\perp}/L_{\perp}^2$ , where  $D_{\perp}$  is the standard Bohm diffusion coefficient  $D_{\perp} = \frac{T_e[\text{eV}]}{16B_0}$  and  $L_{\perp}$  the radius of the plasma column (3 cm). The estimation of radial losses by Bohm diffusion was chosen based on the findings on the radial confinement time in section 4.1.6. The background plasma is assumed to be Maxwellian and constant along  $z$ , characterized by a density  $n_e = 10^{18} \text{ m}^{-3}$ , electron temperature  $T_e$  and a plasma flow velocity of  $v_i = 0.5 \sqrt{k_b(T_e + T_i)/m_i}$ , where  $m_i$  denotes the deuterium mass. In the simulations the temperature  $T_e$  is varied between 5 eV and 12 eV.

The friction due to Coulomb collisions with the background is described by a Fokker-Planck collision model with drift and diffusion coefficients taken from [53]. The Coulomb collisions accelerate the argon ions and give rise to thermalization. The ionization and recombination events are simulated again using rate coefficients from [54, 55]. Finally the stationary spatial profiles of particle density, flow velocity and temperature of argon particles are obtained. It is found that the recombination processes do not play a role in the temperature range considered. With the 1-dimensional resolution of the simulation, also the spacial development of the ion charge distribution can be investigated. In figure 40, the results of the simulation for the ratio of  $\text{Ar}^{2+}$  to  $\text{Ar}^+$  in dependence of the electron temperature and the position

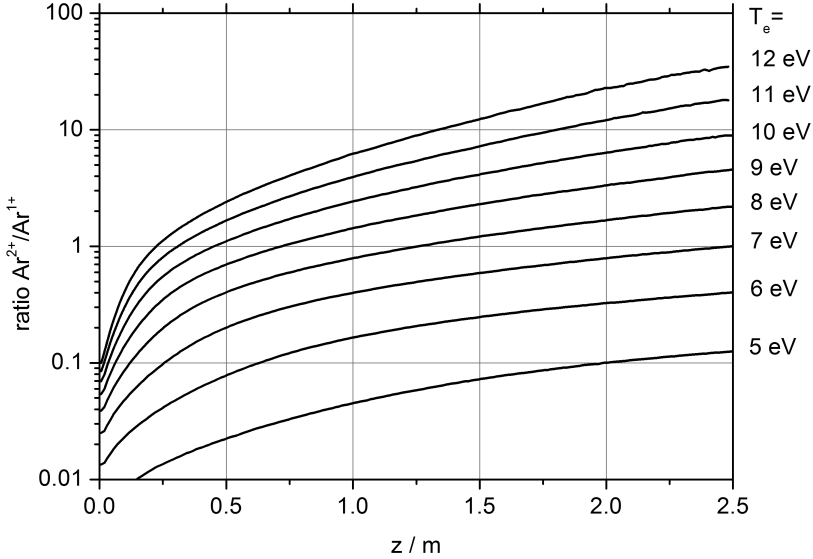


Figure 40: Simulated argon ion charge ratio for  $T_e=5-12$  eV along the z-axis

on the z-axis are plotted.

It is obvious that the ratio changes significantly between 5 and 12 eV. Also, there is a distinct dependency of the  $\text{Ar}^{2+}/\text{Ar}^+$  ratio on the z-axis position, but this variation is not critical if the location of the spectroscopic measurement is fixed. Not shown in this graph is the concentration of  $\text{Ar}^{3+}$ . At electron temperatures of 10 eV and less,  $\text{Ar}^{3+}$  has no significant influence, as its concentration is below 10 % of the total argon ions.

The variation in the charge distribution has to be taken into account when calculating the total ion content, because the method described in this section is only sensitive to  $\text{Ar}^+$ . As mentioned before, for the calibration of the method, a simple factor  $x$  is introduced to bring the calculated ratio between the argon ions and the electrons to 1 for the case of a pure argon plasma (figure 39):

$$\frac{n_{\text{Ar}^+}}{n_e} = \frac{I_{\text{Ar}^+} \cdot 4\pi}{\langle \sigma v \rangle_{\text{pec}} \cdot n_e^2} \cdot x = 1 \quad (16)$$

To achieve a precise calibration, the calibration factor should be given as a function of the electron temperature, because of the variation of the argon ion charge distribution with the electron temperature. However, for mixed D-Ar plasmas at PSI-2, the electron temperature variation is very limited (8-10 eV, table 2). The simulation

results in figure 40 show a ratio of 1:1 up to 4:1 for this electron temperature range at the z-axis position  $z=1.5$  m, where the spectroscopic observation is located. If only  $\text{Ar}^+$  and  $\text{Ar}^{2+}$  are taken into account, this translates to an  $\text{Ar}^+$  ratio of 20 to 50 % of the total argon ion content. This would lead to a possible error by a factor of approximately 2, if the calibration factor is set constant instead of as a function of the electron temperature. The results for the pure argon plasma in figure 39 also show that  $x \approx 10$  for electron temperatures of 8.5 eV as well as 7.5 eV, which indicates that the matching changes not as much with the electron temperature as the simulation results would suggest. This could be an evidence that the  $\text{Ar}^{2+}/\text{Ar}^+$  ratio is not changing as much in the experiment as it was predicted by the simulation. As a consequence, the matching factor is set to be constant at  $x=10$  for this narrow electron temperature range. With the application of the matching factor, the total Ar ion content including  $\text{Ar}^{2+}$  is measured from the emission of the  $\text{Ar}^+$  emission line. It has to be noted that this factor does not influence the results in any way other than matching them to the simple requirement of 100 % argon ions for a pure argon plasma. The matching factor treats all fixed, systematic errors which lead to the calculated result of the argon ion ratio not being 100 % in a pure argon plasma. These errors can be caused by the presence of  $\text{Ar}^{2+}$ , deviations between the calculated  $\langle \sigma v \rangle_{pec}$  values and the real-world plasma, and systematic errors in the measurement of the plasma parameters or the intensity of the  $\text{Ar}^+$  line emission. The matched equation is now applied at mixed plasmas with different argon ratios and discharge powers.

Figure 41 shows the results of the measurements. The x-axis shows the percentage of argon on the total gas input of deuterium and argon, while the y-axis shows the percentage of argon ions on the total ion amount of deuterium and argon. As one would expect, there is an increase in the argon ion concentration with higher argon gas input. Interestingly, for low concentrations of argon impurities, the ratio between the argon gas flow and the argon ion concentration is 1:1. For the high discharge power, it is even bigger than 1:1. But as the argon gas input is increased, the argon ion concentration rises slower than the respective gas input. This can be explained by the higher ionization energy of argon (15,8 eV) compared to deuterium (13,6 eV). With the addition of higher amounts of argon gas, the electron temperature decreases, as a pure deuterium plasma in PSI-2 has a typical electron temperature of 10 eV, while it is 3 eV for a pure argon plasma. The decreased electron temperature might lead to the slower rise of the argon ion ratio compared to the argon gas ratio. Accordingly, the increase in discharge power also increases the argon ion ratio. As the error bars and the variation between single datapoints

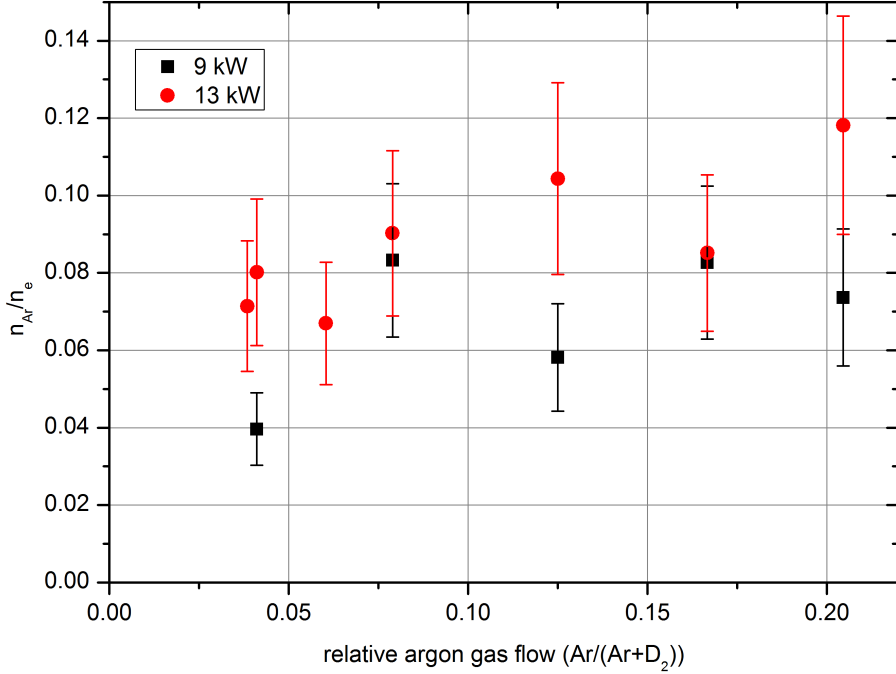


Figure 41: Argon ion ratios for mixed deuterium-argon plasmas with variation in discharge power and argon gas ratio

show, there are some uncertainties in the determination of the absolute values. They are partly due to statistical errors in the plasma parameter measurements, which are amplified by the strong dependence of the photon emissivity coefficient on the electron temperature in particular. Also, the uncertainty in the argon ion charge distribution, which was discussed before, plays a role. But, if one considers that the argon ion ratio should be strictly monotonically increasing, and the argon gas input is well known, one can find a reliable relation between argon gas input and argon ion concentration with this method.

#### 4.1.6 Helium ion concentration

In this section, two different methods for measuring the helium ion concentration are introduced. The first one is the same method which was also applied to argon in the previous section. The possible presence of  $\text{He}^{2+}$  ions is no issue in this case.

Because of its high ionization energy,  $\text{He}^{2+}$  is not expected in the plasma. This was also confirmed by in-situ mass spectrometer measurements. The  $\text{He}^+$  line at 468,6 nm ( $n=4-3$ ) is used for the observation of the line intensity. The energy levels of this transition are at 51 eV and 48 eV respectively, it is also the  $\text{He}^+$  line observable by the 2D imaging spectrometer with the lowest energy levels. Still, the intensity of the  $\text{He}^+$  line was found to be very low, especially for the case of mixed D+He plasmas. Here, the typical electron temperature is lower than in pure helium plasmas. For a pure helium plasma, with typical electron temperatures of 15-20 eV, the  $\text{He}^+$  is visible and a calibration of equation (17) could be performed in the same way as it was described in the previous section for argon.

$$\frac{n_{\text{He}^+}}{n_e} = \frac{I_{\text{He}^+} \cdot 4\pi}{\langle \sigma v \rangle_{\text{pec}} \cdot n_e^2} \cdot x \quad (17)$$

The matching factor could be determined as  $x = 3$  by the application of this method to a pure helium plasma. In mixed plasmas, the helium line emission was not visible below a helium gas fraction of 80 % of the total gas input. The background, which is mostly consisting of deuterium molecular lines, is too high to identify the  $\text{He}^+$  line even when the integration time is increased. Figure 42 shows the results of these measurements; the hollow symbols show the cases in which the  $\text{He}^+$  line was not visible and thus the result for the helium ion ratio had to be 0. The plot of the corresponding photon emissivity coefficients (figure 43) shows that the photon emissivity coefficients are quite low for electron temperatures of 10 eV, which results in a low light emission of this line. This is due to the high energy levels of this transition, which leads to a very low population of this level in cold plasmas. The result is the light emission below the detection limit. Therefore this method might be applicable for plasmas with higher  $T_e$ , but not for deuterium plasmas in PSI-2 with  $T_e = 10$  eV.

However, to measure the helium ion density in PSI-2, a second method is used which was already applied at PISCES-B [56]. Here, a neutral helium line is used, which is still well visible in low temperature plasmas because of the low energy levels of the respective transition. But the relation between the neutral helium line intensity and the helium ion concentration is somewhat more complicated.

The starting point is a continuity equation for helium ions in the notation of [56]:

$$\frac{\partial n_{\text{He}^+}}{\partial t} = \langle \sigma v \rangle_{\text{He} \rightarrow \text{He}^+} \cdot n_e \cdot n_{\text{He}} - \frac{n_{\text{He}^+}}{\tau_{\text{He}^+}^{\text{perp}}} \quad (18)$$

The source term is the ionization rate coefficient  $\langle \sigma v \rangle_{\text{He} \rightarrow \text{He}^+}$  times the electron density and neutral helium density  $n_{\text{He}}$ . The losses are represented by the helium

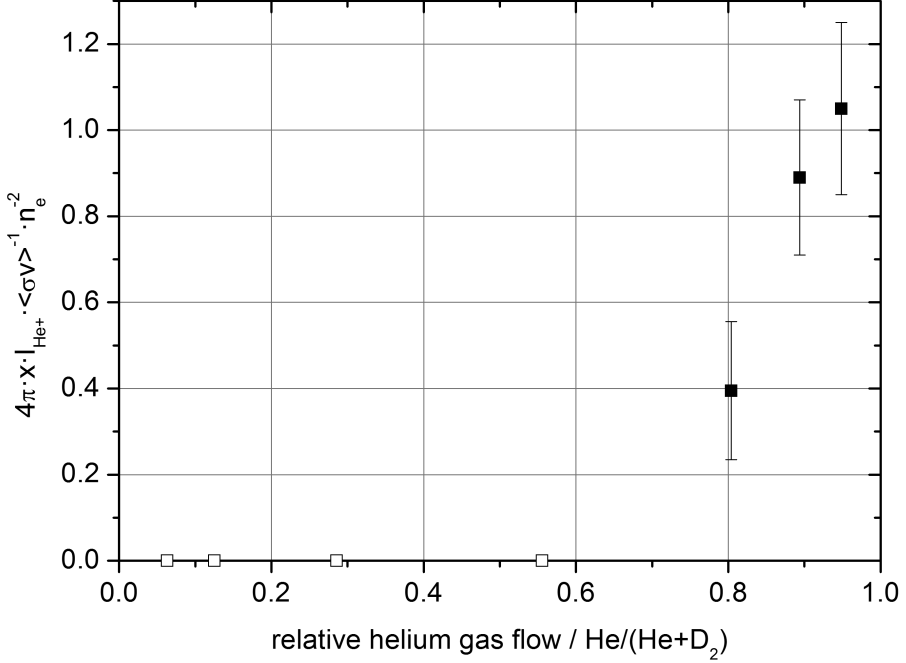


Figure 42: Results for  $n_{He^+}/n_e$  calculated with equation (17) for mixed deuterium-helium plasmas with variation in helium gas ratio

ion density  $n_{He^+}$  over the confinement time perpendicular to the magnetic field. Other processes like the recombination or ionization of  $He^+$  and  $He^{2+}$  are neglected, because their respective rate coefficients are much smaller [57]. In [56] it is also shown that the axial losses can be neglected in PISCES-B. Their axial confinement time  $\tau_{He^+}^{\parallel}$  is estimated by

$$\tau_{He^+}^{\parallel} = \frac{l}{v} \quad (19)$$

, with  $l$  as the plasma length and  $v$  the flow velocity of the helium ions. With a mach number of 0.1 at 10 eV [58] and a plasma length of 1.5 m, a parallel confinement time of 1 ms is estimated for PISCES-B [56]. For PSI-2, with plasma length of 2.5 m, the parallel confinement time is in a similar range. Even if the ion velocity is estimated at 50 % of the sound speed, the confinement time is still at 0.33 ms. This is one order of magnitude bigger than the radial confinement time, which is calculated later in this chapter (figure 44).

In equilibrium the time derivative of equation (18) is equal to zero and the helium

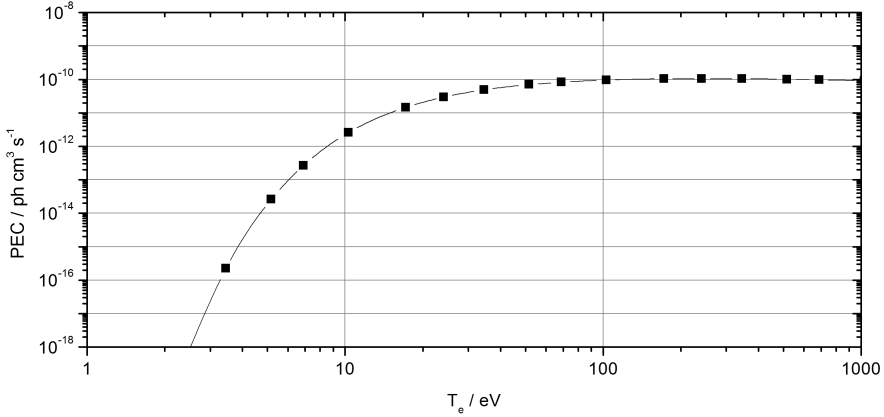


Figure 43: Photon emissivity coefficients for the 468,6 nm transition of  $\text{He}^+$  for  $n_e = 10^{12} \text{ cm}^{-3}$  [56]

ion density gets:

$$n_{\text{He}^+} = \tau_{\text{He}^+}^{\text{perp}} \cdot \langle \sigma v \rangle_{\text{He} \rightarrow \text{He}^+} \cdot n_e \cdot n_{\text{He}} \quad (20)$$

The ionization rate coefficient times the electron and neutral helium density can be written as an ionization flux:

$$n_{\text{He}^+} = \tau_{\text{He}^+}^{\text{perp}} \cdot \frac{\Gamma_{\text{He} \rightarrow \text{He}^+}}{L} \quad (21)$$

Here,  $\Gamma_{\text{He} \rightarrow \text{He}^+}$  is the line-integrated ionization flux, which is observed perpendicular to the plasma column with the imaging spectrometer. To account for the line-integrated measurement, the flux is divided by the length of the line of sight in the plasma  $L$ . The line-integrated flux is connected to the measured line-integrated light emission of a neutral helium spectral line  $I_{\text{HeI}}$  by:

$$\Gamma_{\text{He} \rightarrow \text{He}^+} = 4\pi \frac{S}{XB} I_{\text{HeI}} \quad (22)$$

The  $S/XB$ -factor gives the number of ionizations per photon for a single spectral line. In this case the line at 447.1 nm ( $2^3\text{P}-4^3\text{D}$ ) was used, and the required  $S/XB$  factors are obtained from the ADAS database [59].

For a pure helium plasma, the helium ion density can again be replaced by the electron density in equation (20) and the confinement time can be calculated:

$$\tau_{\text{He}^+}^{\text{perp}} = \frac{n_e}{\Gamma_{\text{He} \rightarrow \text{He}^+}/L} \quad (23)$$

This confinement time can be compared with calculated confinement times like a classical confinement time or the Bohm confinement time. The specific nature for

the radial losses can be numerous. Besides the classical diffusion across the magnetic field lines because of collisions and the enhanced Bohm diffusion, other diffusion mechanisms are imaginable. The losses could also be increased by ambipolar diffusion, where electrons increase the diffusion of ions in the same direction due to electric fields. Another model is the Simon diffusion [60], where electrons are moving in axial direction while ions are moving in radial direction. The resulting space charge is neutralized by a current over the plasma chamber wall. And finally, bursts of plasma transport in radial direction driven by turbulences are known to exist in PSI-2 [61]. However, in the scope of this thesis, the radial confinement time is just needed as a value for calculating the helium ion density from the intensity of the neutral helium line. The detailed nature of the diffusion mechanism is not included in this method. The following comparison with the classical and Bohm diffusion is carried out to check the results of the calculated confinement times from equation (23) for consistency. In [56], the classical confinement time is expressed as  $\tau_{He^+}^{perp}(\text{classic}) = r^2/D_{\text{classic}}$ , with  $r$  as the plasma radius and  $D_{\text{classic}}$  as the diffusion coefficient. The diffusion coefficient is calculated by dividing the ion Larmor radius  $\rho_{He^+}$  by the ion-neutral collision time  $\tau_{i-n}$ . The Larmor radius is calculated for helium ions at  $T_i = 0.1 \cdot T_e$  and has a value of  $\rho_{He^+} = 6 \text{ mm}$  for  $T_i = 1 \text{ eV}$ . The ion-neutral collision time is calculated as

$$\tau_{i-n} = \frac{1}{\langle \sigma v \rangle_{i-n} n_{He}} \quad (24)$$

with the neutral density  $n_{He}$  and the rate coefficient  $\langle \sigma v \rangle = 2 \cdot 10^{-15} \text{ m}^3/\text{s}$  [57]. With this, the classical confinement time can be calculated as:

$$\tau_{He^+}^{perp}(\text{classic}) = \frac{r^2 \tau_{i-n}}{\rho_{He^+}^2} \quad (25)$$

The Bohm confinement time is written as  $\tau_{He^+}^{perp}(\text{Bohm}) = r^2/D_{\text{Bohm}}$ , with the Bohm diffusion coefficient  $D_{\text{Bohm}} = \frac{T_e}{16B}$  [62]. The corresponding confinement time is:

$$\tau_{He^+}^{perp}(\text{Bohm}) = \frac{16r^2 B}{T_e} \quad (26)$$

The calculations for the confinement times do not take into account geometrical effects because they are not known for the rather complicated shape of the PSI-2 plasma profile.

In figure 44, the measured confinement time from equation (23) is plotted together with the calculated classical confinement time and the Bohm confinement time. As figure 44 shows, the measured confinement time is in the same region as the

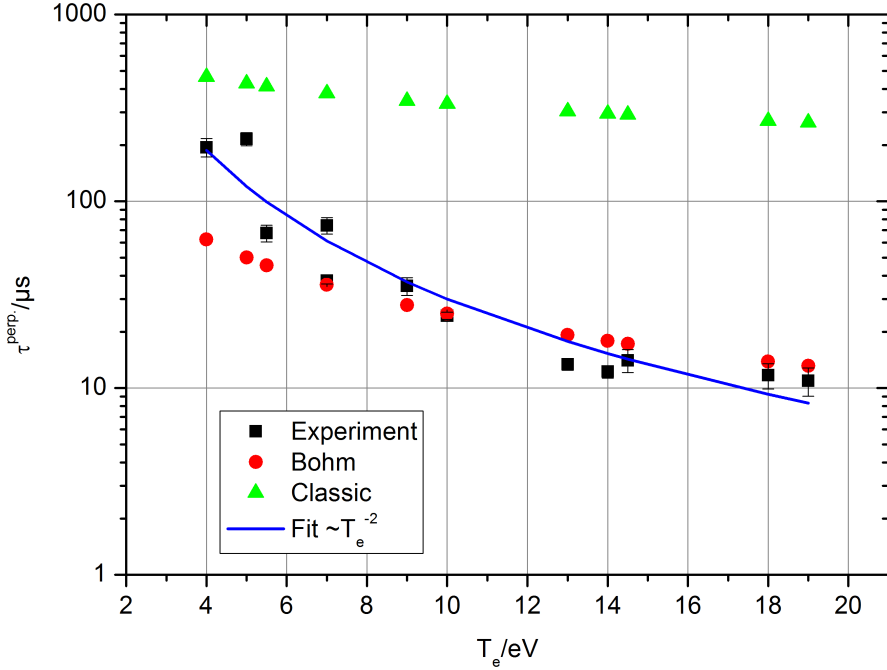


Figure 44: Measured perpendicular confinement time compared to classical and Bohm confinement time

calculated Bohm diffusion, as it was also observed at PISCES-B with very similar plasma properties. Only for lower electron temperatures, the measured confinement time is longer than the confinement time calculated by Bohm diffusion. Here, other processes might play a role which increase the confinement time. Therefore, a fit is applied to the datapoints, which gives a proportionality of  $\tau_{\text{He}^+}^{\text{perp}} \propto T_e^{-2}$ . In [56], this proportionality, together with the proportionality of  $S/XB$  on  $n_e$  and  $T_e$  is used to give a scaling law for the helium ion density in equation (21). But here it was found that also with the absolute values for  $S/XB$ ,  $\tau_{\text{He}^+}^{\text{perp}}$ ,  $n_e$ ,  $L$  and the absolute line intensity, the resulting helium ion ratio is 1, and no matching factor is needed. This can be explained by the calculation of the confinement time with equation (23). Because it is based on the condition  $n_{\text{He}^+} = n_e$  for the pure helium plasma, this calculated confinement time already matches the result for the helium ion ratio to 100 % for a pure helium plasma, similar to the matching factor which was required in section 4.1.5. Figure 45 shows the relation between the helium ion ratio and the helium gas input. The results show that this method is also suitable for low

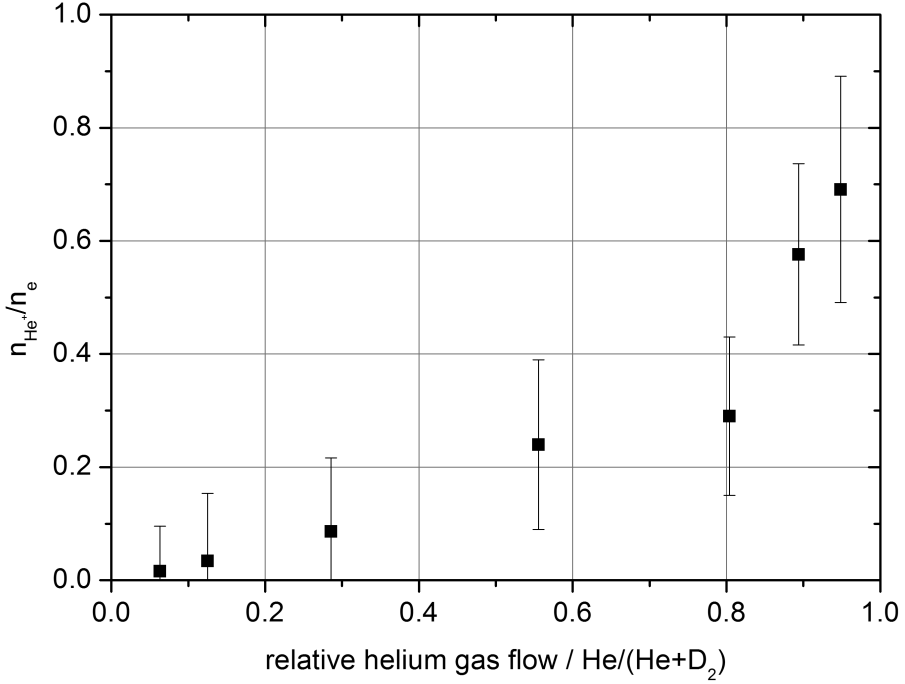


Figure 45: Helium ion ratios for mixed deuterium-helium plasmas with variation in helium gas ratio

helium gas input ratios. It is again found that the concentration of the impurity ion content is smaller than its corresponding gas flow ratio. The measurements in PISCES-B [56] show very similar results. This difference can be explained by the electron temperature of the plasma. In a deuterium plasma with small amounts of helium, the electron temperature stays at the typical value for pure deuterium plasmas (10 eV). This is lower than the typical electron temperature in a pure helium plasma in PSI-2 (around 20 eV), which leads to less ionization of helium atoms. Only for high fractions of helium gas, also the helium ion ratio strongly increases up to 100 % for the simple case of only a pure helium plasma. For the application in this thesis, the relevant concentrations of helium are below 10 %. Here, this method can give results which are more accurate than a simple estimation of the helium ion content by the gasflow ratios.

## 4.2 Studies of deuterium retention in tungsten

In this section, the results of experiments regarding the deuterium retention in tungsten under the presence of plasma impurities are shown.

The exposures of tungsten samples in PSI-2 were performed with a variation of certain factors, like the impurity content in the plasma or the fluence, while keeping all other factors constant. Especially the sample temperature is kept constant, as this factor has a great influence on the retention of deuterium in tungsten. A variation of these factors between experiments could obscure the influences of other factors on the deuterium retention.

Another important factor is the sample itself and its preparation. For technical reasons, in total 3 different kinds of tungsten samples were used. Here, they are called type A, B and C. Type A and B are samples for the side manipulator (13x13 mm rectangular shape, see figure 20), while samples of type C are for the target station manipulator (11 mm diameter circular shape). Type A and C were fabricated from tungsten rods which were available at the IEK-4 institute. It is so-called "ITER-grade" polycrystalline tungsten, with grain sizes from 0.5 to 3  $\mu\text{m}$ , which are elongated and oriented perpendicular to the plasma-facing surface of the samples. Type B is fabricated under the same specifications by an external company (Negele-Hartmetall). All samples have a mechanically polished mirror-finish surface and were annealed at 1270 K for 2 hours to desorb hydrogen trapped in the metal during the fabrication. While sample type A was polished by an external company, sample type B and C were polished at IEK-4. It turned out that the polishing quality of type B and C is better than the polishing of type A. This has to be taken into account when analyzing the surface structure in section 4.2.1. After the preparation of the samples, the initial surface morphology was investigated using SEM imaging. Then, the individual exposures to the plasma in PSI-2 were performed. In total 3 exposure series were conducted:

The first series were exposures of sample type A to a deuterium plasma with impurities, varying the species (helium or argon) and concentration (0-8 %) of the impurities. These experiments were performed to find out the general influence of helium and argon impurities and check the results for agreement with the literature. The second series were exposures of sample type B to a deuterium plasma with and without helium impurity with a fixed ratio, but a variation in total fluence. This series of exposures has the aim to investigate the influence of helium impurities on the relation between deuterium retention and fluence.

The third series of exposures were repetitions of exposures to deuterium plasmas with helium or argon impurities intended for TEM imaging of the surface. In table 2 the exposure parameters of all samples are summarized. The detailed results for the deuterium retention are discussed in the second part of this section.

no.	plasma	$n_e/\text{m}^{-3}$	$T_e/\text{eV}$	$\Phi/\text{m}^{-2}\text{s}^{-1}$	$\Gamma/\text{m}^{-2}$	$T_S/\text{K}$
A-1	D	$9.0 \cdot 10^{17}$	11	$1.2 \cdot 10^{22}$	$1.0 \cdot 10^{26}$	380
A-2	D + 4 % Ar	$1.0 \cdot 10^{18}$	10	$1.0 \cdot 10^{22}$	$1.0 \cdot 10^{26}$	380
A-3	D + 1 % He	$8.0 \cdot 10^{17}$	12	$1.0 \cdot 10^{22}$	$1.0 \cdot 10^{26}$	380
A-4	D + 5 % He	$9.5 \cdot 10^{17}$	13	$0.9 \cdot 10^{22}$	$1.0 \cdot 10^{26}$	380
A-5	D + 8 % Ar	$9.0 \cdot 10^{17}$	9	$1.0 \cdot 10^{22}$	$1.0 \cdot 10^{26}$	380
B-1	D	$5.5 \cdot 10^{17}$	10	$1.0 \cdot 10^{22}$	$5.0 \cdot 10^{25}$	380
B-4	D + 5 % He	$1.2 \cdot 10^{18}$	10	$0.9 \cdot 10^{22}$	$2.0 \cdot 10^{25}$	380
B-5	D + 5 % He	$1.2 \cdot 10^{18}$	11	$0.9 \cdot 10^{22}$	$5.0 \cdot 10^{24}$	380
B-6	D + 5 % He	$1.2 \cdot 10^{18}$	11	$0.9 \cdot 10^{22}$	$2.0 \cdot 10^{24}$	380
B-7	D	$1.5 \cdot 10^{18}$	11	$1.0 \cdot 10^{22}$	$2.0 \cdot 10^{24}$	380
B-8	D	$1.5 \cdot 10^{18}$	11	$1.1 \cdot 10^{22}$	$2.0 \cdot 10^{26}$	390
B-9	D + 5 % He	$1.4 \cdot 10^{18}$	14	$0.9 \cdot 10^{22}$	$2.0 \cdot 10^{26}$	390
C-1	D	$5.5 \cdot 10^{17}$	15	$4.5 \cdot 10^{21}$	$6.5 \cdot 10^{25}$	410
C-2	D + 8 % Ar	$7.0 \cdot 10^{17}$	8	$5.5 \cdot 10^{21}$	$6.5 \cdot 10^{25}$	400
C-3	D + 5 % He	$7.0 \cdot 10^{17}$	17	$6.0 \cdot 10^{21}$	$9.0 \cdot 10^{25}$	410

Table 2: Exposure parameters of all tungsten samples

During the exposures in PSI-2, the temperature of the samples was monitored with the infrared camera, or by the thermo element of the sample manipulator if the IR camera was not available. The plasma parameters given in table 2 were measured with the langmuir probe. One exception is the concentration of plasma impurities, which was measured by spectroscopy as shown in section 4.1, because the impurity concentration cannot be measured by langmuir probe diagnostics.

After the exposure, the samples were studied for their surface morphology by SEM imaging, and for their deuterium content by thermal desorption spectroscopy. With one test sample, the deuterium retention was also measured by laser-induced desorption. These measurements were only performed on one test sample because their purpose was to investigate the spacial distribution of the deuterium retention on the sample surface. Once this distribution was found, it was assumed not to change, because it only depends on the plasma profile, which stays constant. The result of this

test measurement showed no relevant spacial variation of the deuterium retention over the sample surface. Therefore, for all the other samples the thermal desorption spectroscopy was the standard method for measuring the deuterium retention, since it has advantages over the laser-induced desorption spectroscopy, as discussed in section 3.5.

#### 4.2.1 Surface modifications

This section discusses the surface morphology of the tungsten samples before and after plasma exposure. The first comparison of SEM images in figure 46 shows the sample surface before and after exposure to a deuterium plasma in PSI-2. The im-

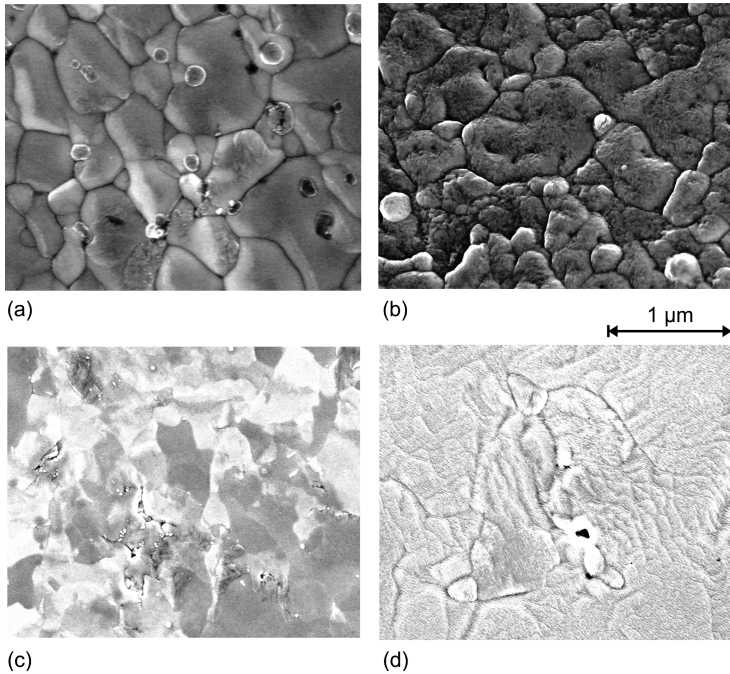


Figure 46: Surface of sample type A before (a) and after (b) deuterium exposure and surface of sample type B before (c) and after (d) deuterium exposure

ages (a) and (c) depict the samples of type A and B before exposure to the plasma. The images show that the grain size of both samples is in the range of  $1 \mu\text{m}$ . The surfaces of both sample types look different with respect to the grain boundaries. On sample type A, the grain boundaries are clearly visible as dark lines and even

seem to be indented. On sample type B, the grain boundaries are not directly visible. The grains can only be distinguished by the different shades of the grains itself. The different shades are an effect of the grain orientation observed by SEM imaging. Depending on the orientation of the grain and its lattice structure, the electron beam has a changing effectiveness in producing secondary electrons. This implies also an intact lattice structure close to the surface, which is an indicator for good polishing. The difference in the grain boundary appearance can have two different reasons: On the one hand, it could be due to variations in the tungsten production, which lead to more pronounced shapes of the grain boundaries for sample type A. On the other hand, the polishing of the surface could lead to differences in the appearance of the grain boundaries on the surface. As mentioned before, the samples of type B have a better polishing quality in terms of surface roughness and scratches on the surface. By grinding and polishing, the surface of the samples is not eroded uniformly: Certain tungsten grains are eroded faster than others, and more importantly, also the grain boundaries are eroded faster. These differences get more pronounced with a fast erosion by bigger grains in the polishing solution. With very small polishing grains, the erosion of the surface gets slower and a more uniform surface can be achieved. Therefore it is assumed that the differences in the surface structure are resulting mainly due to differences in the polishing, with the samples of type A simply not polished to the same degree of surface roughness as sample type B. This assumption is supported by some spots of sample type B, where the grain boundaries are still visible like in sample type A. This can also be seen in figure 46(c) as small cracks or trenches along some of the grain boundaries. These are the remains of the same surface structure as in sample type A, while the other parts are polished to a smaller surface roughness by very small polishing grains.

Now the surface morphology of the unexposed samples is compared to samples which were exposed to a deuterium plasma, namely sample A-1 (figure 46(b)) and sample B-1 (figure 46(d)). The exposure parameters for both samples can be found in table 2. The comparison shows a similar change in the surface structure for both sample types. While the global surface structure remains unchanged (the surface is still flat), there is a change of the surface of the single grains. It exhibits a certain surface roughness in the 10-100 nm-scale. Especially the sample in image (d) shows very fine grooves on its surface, with different grains showing different directions of these grooves.

Such changes of the surface morphology can be caused either by direct erosion of the surface by the deuterium plasma, or by effects induced by the implantation of deuterium into the sample surface. The sputtering threshold of deuterium on tungsten

of 244 eV [63] is well above the ion energy of 40 eV during the exposure. However, it could be possible that on the surface a layer of tungsten oxide is present, which can be sputtered more easily. The theoretical sputtering threshold for this case is 18 eV [64], but there are also experiments which suggest a noticeably higher value of 65 eV [65].

Surface morphology changes on the nm-scale due to deuterium implantation were also observed in other experiments, although only at higher ion fluxes in the range of  $10^{24} \text{ m}^{-2}\text{s}^{-1}$  [66]. The presence of these structures at lower ion fluxes could be explained by differences in the tungsten material.

The next images in figure 47 show the samples A-1(a), A-3(b) and A-4(c) after exposures to a deuterium plasma with different ratios (0 %, 1 % and 5 %) of helium impurities in the plasma. There is a distinct change in the surface morphology when

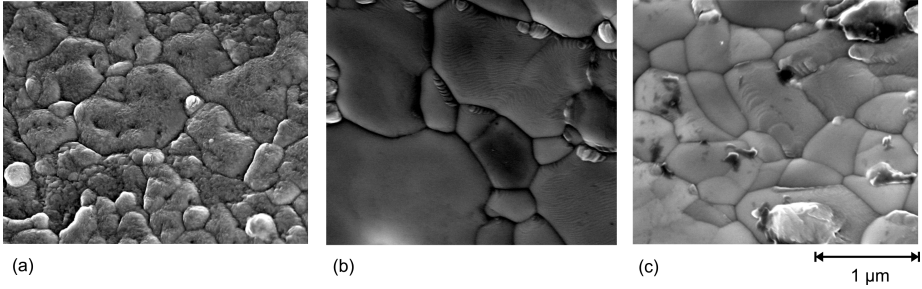


Figure 47: Surface of sample type A after deuterium exposure without (a) and with 1 % (b) and 5 % (c) helium impurity in the plasma

helium is present as a plasma impurity. While there are still some fine grooves visible on some grain surfaces especially in picture (b), overall the smoothness of the grain surfaces is increased when helium impurities are present in the plasma. The shape of the surface on the  $\mu\text{m}$ -scale and the appearance of the grain boundaries stays constant, which implies that the increased smoothness of the grain surfaces is not due to erosion. This is also backed up by the sputtering threshold energy of 140 eV for helium on tungsten [63]. The more probable explanation is that the helium content in the plasma reduces the surface morphology changes by deuterium retention. This was also observed in the literature, with the most prominent example being the suppression of blisters on the tungsten surface with the addition of helium impurities [17]. The same series of tungsten exposures, but with argon as the plasma impurity, is shown in figure 48. Here, the surface of the tungsten sample also appears smoother when impurities are present in the plasma. This is

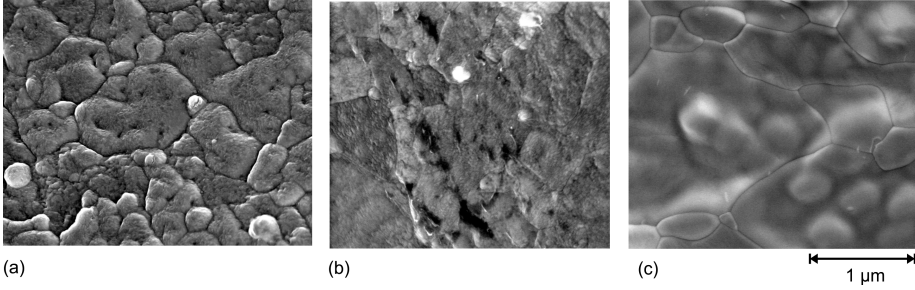


Figure 48: Surface of sample type A after deuterium exposure without (a) and with 4 % (b) and 8 % (c) argon impurity in the plasma

especially evident for the case with 8 % Ar impurity in the plasma. But in contrast to the helium case, the mechanism for the smoothing of the surface is erosion of the tungsten surface by Ar impurities in the plasma. Ar has a much lower sputter threshold energy of 30 eV [63] compared to deuterium or helium, which is also below the ion energy of 40 eV in these exposures. Also, due to the presence of  $\text{Ar}^{2+}$  ions, which was shown in section 4.1.5, the ion energy of these  $\text{Ar}^{2+}$  ions is 80 eV. The doubling of the ion energy in this range leads to a sputter yield increase of one order of magnitude [63]. Therefore the erosion of the tungsten surface by low concentrations of argon impurities is credible. The images in figure 48 also show that the bottom limit for the argon concentration which produces this distinct erosion and smoothing of the tungsten surface, is between 4 and 8 %.

For samples C-1, C-2 and C-3, which were exposed to a D, D+Ar and a D+He plasma respectively, cross-section images were made by TEM imaging. For the TEM images, a cross section of the sample surface is cut from the sample with a focused ion beam. The thickness of the slice is about 100 nm. Before cutting, the surface of the sample is coated with platinum to prevent the ion beam from damaging the sample surface in the slice. The cross-sections of the surfaces are shown in figure 49. The different appearance of the tungsten bulk in the three samples is caused by variations in the sample preparation with the focused ion beam and the sample thickness, as well as the possible difference in the grain orientation. For the D+He case, a layer of 10-15 nm thickness is visible on the surface of the sample. This layer is supposedly formed by the helium nanobubbles. They form a porous structure in the tungsten material, which is a critical factor for the reduction of deuterium retention in tungsten under the influence of helium impurities in the plasma. While the helium nanobubbles were also observed in literature, the detection of he-

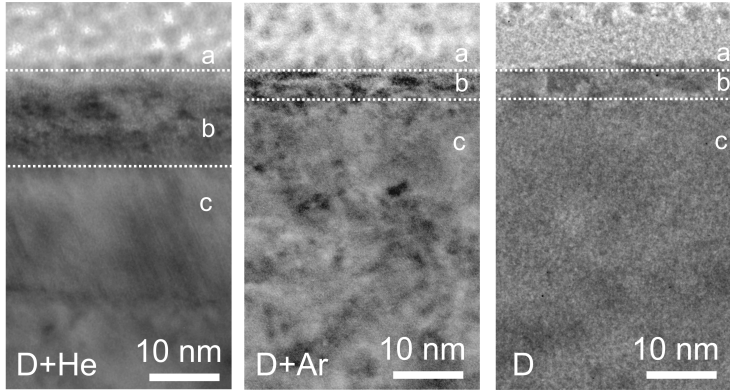


Figure 49: TEM cross-section images of sample type C exposed to deuterium plasmas with 8 % Ar, 5 % He and 0 % impurities. a) platinum coating, b) helium nanobubbles / defects, c) bulk tungsten

Helium nanobubbles in the samples treated in this thesis is a proof that the observed reduction in deuterium concentration is caused by helium nanobubbles as well. The image of the sample exposed to the plasma with argon impurities also exhibits a layer on the surface, although it is more shallow ( $<5$  nm) and not as clearly visible as the helium nanobubble layer. It is supposedly formed due to defects which are induced by the incident argon ions. Instead of reducing the total deuterium retention, this layer seems to slightly increase the total deuterium retention. This is shown by the TDS measurements in the next section, and explained in section 5, which explains the mechanism of the influence of both the helium nanobubble layer and the argon-induced layer. In the third image, which shows the sample exposed to the pure deuterium plasma, a damaged layer at the surface can be identified as well. It has the same depth as the layer produced by argon. This indicates that also deuterium is able to produce defects in the first few nm of the sample surface. But in contrast to argon, these defects are probably produced not directly due to collisions of the ions with the tungsten atoms, but indirectly by deuterium retention, as mentioned earlier in this section. Which mechanism leads to the damaged layer cannot be verified by the TEM images. But the change in the TDS spectra shape, as shown in the next section, proves that both layers have different origins and therefore also influence the deuterium retention differently.

### 4.2.2 Deuterium retention with plasma impurities

In this section, the results of TDS measurements for the samples which were exposed to a deuterium plasma with different concentrations of He- and Ar-impurities (sample type A) are given.

Figure 50 shows the results for helium as the plasma impurity. The graph shows

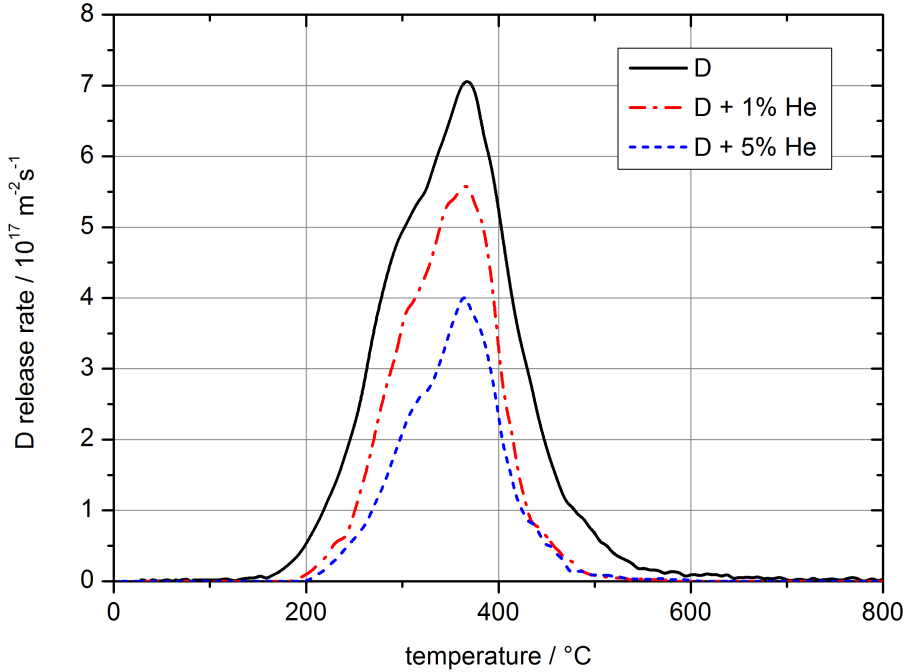


Figure 50: TDS spectra with different amounts of helium impurities during exposure

the desorption rate of deuterium in dependence of the sample temperature during the TDS measurement. The heating rate was linear at 0.4 K/s. With helium as a plasma impurity, also helium is present in the samples and gets desorbed during the TDS measurement. The high resolution mass spectrometer used for the TDS measurements can separate the two peaks from D<sub>2</sub> (4.003 amu) and He (4.028 amu). An integration of the deuterium desorption rate over time delivers the total desorbed deuterium content from the sample. Obviously the deuterium retention decreases with increasing helium impurities. The calculated values for the total deuterium retention are shown in table 3. While the total deuterium retention decreases with the presence of helium impurities, the shape of the TDS spectra does not change

plasma exposure	deuterium fluence	deuterium retention	helium retention
100 % D	$1.0 \pm 0.1 \cdot 10^{26} \text{ m}^{-2}$	$3.8 \pm 0.5 \cdot 10^{20} \text{ m}^{-2}$	–
99 % D + 1 % He	$1.0 \pm 0.1 \cdot 10^{26} \text{ m}^{-2}$	$2.5 \pm 0.4 \cdot 10^{20} \text{ m}^{-2}$	$1.8 \pm 0.4 \cdot 10^{19} \text{ m}^{-2}$
95 % D + 5 % He	$1.0 \pm 0.1 \cdot 10^{26} \text{ m}^{-2}$	$1.4 \pm 0.3 \cdot 10^{20} \text{ m}^{-2}$	$1.6 \pm 0.4 \cdot 10^{19} \text{ m}^{-2}$

Table 3: Deuterium retention in tungsten samples exposed to deuterium plasmas with helium impurities

significantly. This behaviour implies that the density of trapping sites or the amount of deuterium stored in the trapping sites is decreased, but the type of trapping sites stays constant. To get more information on the type of trapping sites, the shape of the TDS spectra has to be analyzed. In all 3 cases, a big peak at around 460 °C is visible together with a smaller peak at 300 °C. Both peaks are overlapping, therefore two single peaks have to be fitted to the TDS spectrum to give the original shape and position of both peaks. An example image for these two fitted peaks is shown in figure 51. To find out the desorption energies of the trapping sites, the peak area

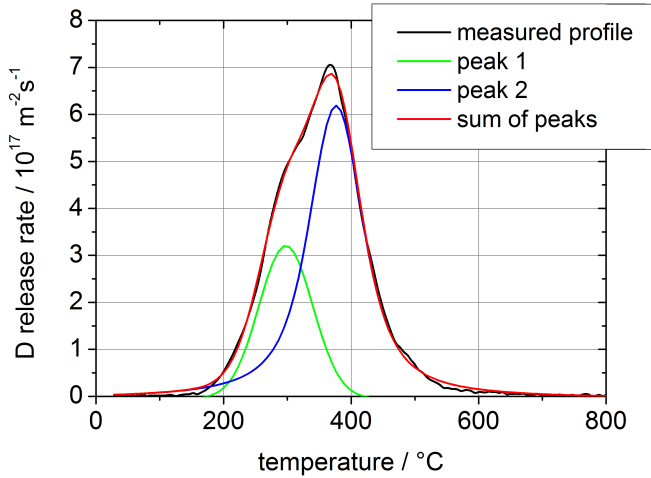


Figure 51: Two Voigt-shaped peaks fitted to the TDS spectrum for the case of pure deuterium exposure

method as described in section 3.5 is used. The calculated desorption energies are shown in table 4. The numbers indicate a small decrease of the desorption energy for the low temperature peak, and a small increase of the desorption energy for the high temperature peak. This indicates a change in the type of trapping sites. However,

plasma exposure	$E_D$ (P1)	$E_D$ (P2)
100 % D	$0.76 \pm 0.13$ eV	$0.52 \pm 0.12$ eV
99 % D + 1 % He	$0.62 \pm 0.15$ eV	$0.87 \pm 0.18$ eV
95 % D + 5 % He	$0.55 \pm 0.13$ eV	$0.76 \pm 0.17$ eV

Table 4: Calculated desorption energies for peak 1 and peak 2 from figure 51

it has to be taken into account that this method gives the desorption energy, and not the actual trapping energy, which would determine the type of trapping sites. The desorption energy is the sum of the energies required to detrapp the deuterium, and recombine it at the surface. If the surface does not change, this can be assumed to be constant. But as the results of section 4.2.1 have shown, the surface of the tungsten samples changes in that helium nanobubbles are formed in the first 20 nm below the surface. These structures may influence the recombination on the surface, and therefore alter the desorption energies. Another explanation for the changing desorption energies is the sensitivity of the calculation on the peak shape:

$$E_D = \frac{mk_B T_1 T_2}{T_1 - T_2} \ln \left( \frac{N_2}{N_1} \right) \quad (27)$$

Equation (27) shows that the method is especially sensitive to the temperature values. If the peak fitting exhibits an error in the peak position or width, the calculated desorption energies are not accurate. Especially for strongly overlapping peaks, as they are found here (figure 51), the peak fitting might be prone to such errors. In total, it has to be concluded that despite the (small) changes in the calculated desorption energies, the type of trapping sites is not changing. More precisely, the helium impurities do not cause additional trapping of deuterium in tungsten. This is also backed up by the decreasing total retention of deuterium.

In figure 52, the results of the TDS measurements for exposures to a deuterium plasma with argon impurities are shown. The integration of the TDS spectra reveals that the total deuterium retention (table 5) increases when argon impurities are present in the plasma. Unlike for the exposures with helium impurities, the shape of the TDS spectra in figure 52 is changing with the addition of argon impurities to the plasma. The additional peaks indicate that the argon exposure causes additional trapping sites, and that deuterium is permanently trapped in these newly formed trapping sites. This is in contrast to the picture of the helium nanobubbles, where almost no permanent trapping is assumed due to surface recombination losses in the porous structure of the helium nanobubbles.

When comparing the TDS spectra for 4 % and 8 %, it is obvious that the shape

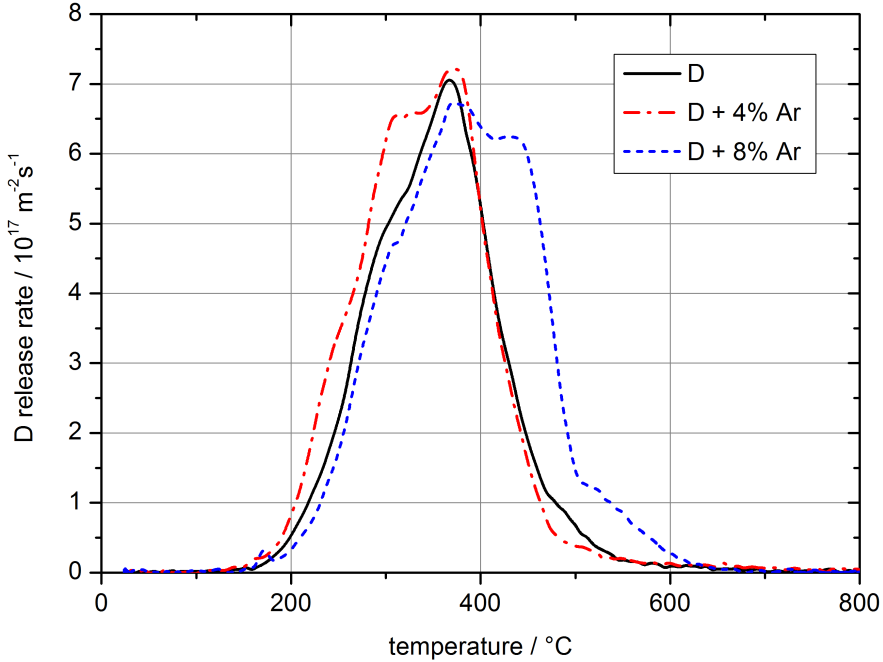


Figure 52: TDS spectra with different amounts of argon impurities during exposure

changes from additional peaks at temperatures below the main peak at 390 °C to additional peaks at temperatures above 390 °C. This behaviour is not intuitive as it is not easily understandable why an increase in the argon concentration leads to the formation of different types of trapping sites. However, the result matches the findings for the surface morphology: While the surface exposed to 4 % argon impurities still exhibits a surface roughness similar to the exposure with a pure deuterium plasma, the surface exposed to 8 % argon impurities appears very smooth. These differences in the surface structures might be reflected in the change of the TDS spectra shape.

The surface morphology also shows the appearance of blisters for the case of 8 % argon impurities. If it is presumed that these blisters are not hidden by the surface roughness for the cases of 0 or 4 % argon impurities, but actually only appear for the case of 8 % argon impurities, the blisters could be related to the TDS spectrum shape. Because deuterium in blisters has a different trapping energy than in other traps, the additional peak at 430 °C could be caused by the release of deuterium trapped in the blisters. The assumption that the blisters are only appearing in

plasma exposure	deuterium fluence	deuterium retention
100 % D	$1.0 \pm 0.1 \cdot 10^{26} \text{ m}^{-2}$	$3.8 \pm 0.5 \cdot 10^{20} \text{ m}^{-2}$
96 % D + 4 % Ar	$1.0 \pm 0.1 \cdot 10^{26} \text{ m}^{-2}$	$4.3 \pm 0.7 \cdot 10^{20} \text{ m}^{-2}$
92 % D + 8 % Ar	$1.0 \pm 0.1 \cdot 10^{26} \text{ m}^{-2}$	$5.0 \pm 0.7 \cdot 10^{20} \text{ m}^{-2}$

Table 5: Deuterium retention in tungsten samples exposed to deuterium plasmas with helium impurities

the case of 8 % argon impurities is not unreasonable: The blisters are an effect of increased deuterium retention. Voids are trapping more and more deuterium, and the increased pressure leads to an expansion which causes blisters. Eventually, the measured  $5.0 \cdot 10^{20} \text{ m}^{-2}$  of total deuterium retention are the onset of deuterium retention which is able produce blisters, and the lower deuterium retention for the other cases is not enough to cause blisters.

#### 4.2.3 Deuterium retention with variation of ion fluence

In this section, the results of the sample exposures with a variation of the deuterium fluence are given. After the results of the previous section have shown that helium reduces the deuterium content, while argon even increases it, the question arises if the advantageous decrease of deuterium retention due to helium changes with the fluence.

To answer this question, tungsten samples are exposed to a deuterium plasma with 5 % helium impurities or to a pure deuterium plasma, under variation of the total deuterium fluence to the sample. All other exposure parameters are kept constant. The different fluences are realized by different exposure times. The resulting upper and lower limits are in the range between  $1.0 \cdot 10^{24} \text{ m}^{-2}$  to  $2.0 \cdot 10^{26} \text{ m}^{-2}$ . Lower fluences are not possible because the resulting exposure times would be in the range of only a few seconds. Higher fluences are limited by the operation time of PSI-2. Figure 53 shows the results of the exposures. As the results show, the fluence dependency is similar for both cases. The linear fit gives the scaling between the fluence  $\Gamma$  and the total retention  $R$  as  $R \propto \Gamma^{0.35 \pm 0.1}$  for the pure deuterium exposure, and  $R \propto \Gamma^{0.4 \pm 0.1}$  for the exposure with 5 % helium impurities. With both scalings being similar, there is no detectable effect of the fluence on the reduction of deuterium retention by helium, like a possible saturation effect at higher fluences. As mentioned in section 2.2, literature shows that a saturation does not occur with sample temperatures above 500 K, while a saturation of the deuterium retention is observed

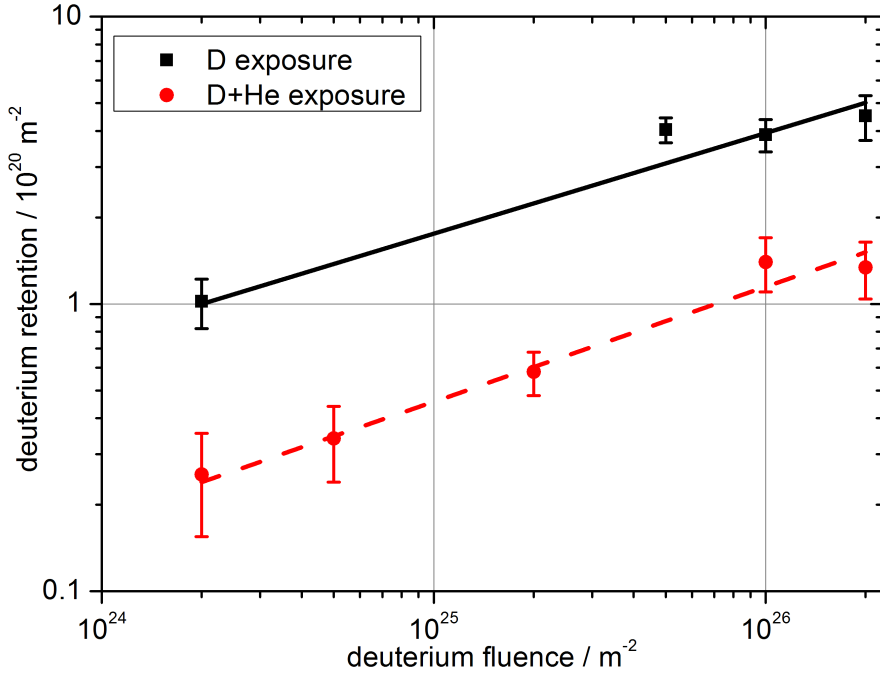


Figure 53: Deuterium retention in dependence of the deuterium fluence to the target with and without helium impurities

at fluences above  $1 \cdot 10^{23} m^{-2}$  when the sample is at room temperature. The results from figure 53 show that at 380 K sample temperature, also no saturation at fluences above  $1 \cdot 10^{23} m^{-2}$  is observed. But the retention might begin to saturate, or at least rise slower, at fluences above  $5 \cdot 10^{25} m^{-2}$ . However, for a definite statement on the saturation, datapoints at even higher fluences would be required.

These results are very important for the comparison with the diffusion modelling, which is shown in section 5. Here, the modelling can be benchmarked to show that the results confirm with the experimental results.

### 4.3 Studies of deuterium retention and erosion of aluminium and beryllium

In addition to tungsten also some other materials and elements, which are used in fusion reactors, are investigated regarding the deuterium retention. One of these elements is beryllium, as the proposed first-wall element of ITER. However, the toxicity of beryllium dust impedes studies in most of the existing plasma-wall-interaction experiments. Only few experiments like PISCES-B, a linear plasma device at the University San Diego, USA, are capable of handling beryllium. For this reason, some elements with properties similar to beryllium were selected as a proxy material for plasma-wall-interaction studies in machines which cannot handle beryllium. The following chapter is about aluminium samples exposed to a deuterium plasma with impurities in PSI-2. Although aluminium with its melting point of 660 °C is no candidate for a fusion reactor wall material, there have already been some experiments of the plasma-wall-interaction properties of aluminium in the scope of fusion research. This is due to some similarities of metals like aluminium or magnesium to beryllium. Aluminium has some similarities regarding its chemical properties because of its comparable electronegativity [67]. This leads to the formation of comparable hydrides and oxides. But on the other hand, many physical properties are different, like the density, melting point or crystal structure. The purpose of the experiments is to check how the differences in physical properties influence the behaviour regarding surface modifications, sputter yields and deuterium retention. While such tests were already performed for exposure to a pure deuterium plasma, the specific topic here is again the influence of plasma impurities. The comparison with beryllium is done with the help of results from experiments at PISCES-B [68]. There, experiments with beryllium samples exposed to a pure deuterium plasma and mixed deuterium + helium/argon plasmas were performed. The plasma parameters in PISCES-B are very similar to the parameters reached at PSI-2.

For the experiments in PSI-2, exposures with variation in the impurity type (helium or argon) and the impurity concentration (0-100 %) were conducted. Naturally the experiments with 100 % impurity concentration, in other words a pure helium or argon plasma, give no information on deuterium retention, but are reference measurements for the influence of the impurities on the surface modification and sputter yields.

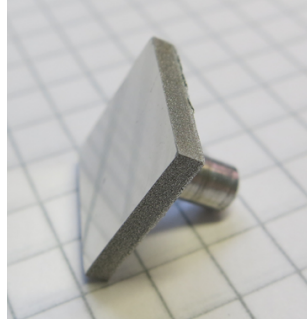


Figure 54: Aluminium sample

Other factors which were kept constant are the sample type (polished aluminium samples for the side manipulator, size 13x13x2 mm, see figure 54, outgassed at 500 °C), exposure temperature (380 K) and deuterium ion flux and fluence (for mixed plasmas,  $\Phi = 10^{22} \text{ m}^{-2}\text{s}^{-1}$  and  $\Gamma = 10^{26} \text{ m}^{-2}$ ). The exact exposure conditions for each sample are given in table 6. The samples were then ex-

no.	plasma	$n_e/\text{m}^{-3}$	$T_e/\text{eV}$	$\Phi_i/\text{m}^{-2}\text{s}^{-1}$	$\Gamma_D/\text{m}^{-2}$	$T_S/\text{K}$
Al-1	D	$1.0 \cdot 10^{18}$	11	$1.2 \cdot 10^{22}$	$1.0 \cdot 10^{26}$	380
Al-3	D + 4 % Ar	$1 \cdot 10^{18}$	11	$1.0 \cdot 10^{22}$	$1.0 \cdot 10^{26}$	380
Al-4	D + 8 % Ar	$8.0 \cdot 10^{17}$	8	$1.0 \cdot 10^{22}$	$1.0 \cdot 10^{26}$	380
Al-10	D + 15 % Ar	$1.5 \cdot 10^{18}$	5	$4.8 \cdot 10^{21}$	$1.0 \cdot 10^{26}$	380
Al-13	Ar	$5.5 \cdot 10^{18}$	3.5	$8.5 \cdot 10^{21}$	$1.0 \cdot 10^{26}(\text{Ar})$	380
Al-7	D + 1 % He	$1.5 \cdot 10^{18}$	10	$1.1 \cdot 10^{22}$	$1.0 \cdot 10^{26}$	380
Al-8	D + 5 % He	$1.5 \cdot 10^{18}$	10	$1.1 \cdot 10^{22}$	$1.0 \cdot 10^{26}$	380
Al-12	D + 15 % He	$1.6 \cdot 10^{18}$	10	$1.2 \cdot 10^{22}$	$1.0 \cdot 10^{26}$	380
Al-5	He	$1.5 \cdot 10^{18}$	15	$1.4 \cdot 10^{22}$	$1.0 \cdot 10^{26}(\text{He})$	380

Table 6: Exposure parameters of all aluminium samples

amined regarding the surface structure (by scanning electron microscope imaging), weight loss (for sputter yield calculations) and deuterium retention (by thermal desorption spectroscopy) (in this order). The results of the measurements are discussed and compared with PISCES-B results for beryllium in the next sections.

### 4.3.1 Surface modifications

In this section, scanning electron microscope images of the aluminium samples prior and after the various exposures are presented and discussed. The samples were polished and outgassed at 500 °C before the exposure to the plasma. Aluminium, as a relatively soft metal, is difficult to polish, and with contact to air, it forms an oxide layer which can be a few nm up to 100 nm thick. On the other hand, the surface preparation of aluminium is not as important as for tungsten, as it is demonstrated in figure 55: The unexposed aluminium sample shows some scratches

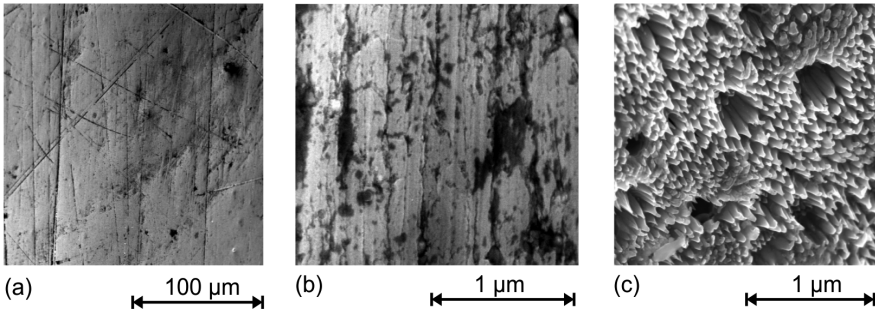


Figure 55: Aluminium sample surface before (a,b) and after (c) exposure to pure deuterium plasma

in the low magnification (a). The higher magnification (b) confirms that the polishing has provided a flat surface, but with many small scratches and edges on the nm-scale still present. Compared with the surface after exposure (c), it is clearly visible that the surface structure has changed. This proves that a larger thickness of the material was eroded during exposure than the characteristic size of the initial surface structures. The complete erosion of the first surface is confirmed by the weight loss measurements, which implies that about 1  $\mu\text{m}$  of the surface are eroded during the plasma exposure (see section 4.3.2). Therefore, scratches on the surface are no concern for the further investigation of the surface morphology.

In all images of this section, the surface is observed under an angle of 45° to the surface normal. Because of this, some areas in the edges of the images appear unsharp. The tilted sample position is required for observing certain surface structures. Figure 56 compares the surface structures on aluminium and beryllium samples after exposure to a deuterium plasma. The surface has a grass-like structure on both materials. This identical behaviour of aluminium and beryllium was also already confirmed by aluminium exposures at PISCES-B [68]. There are two different expla-

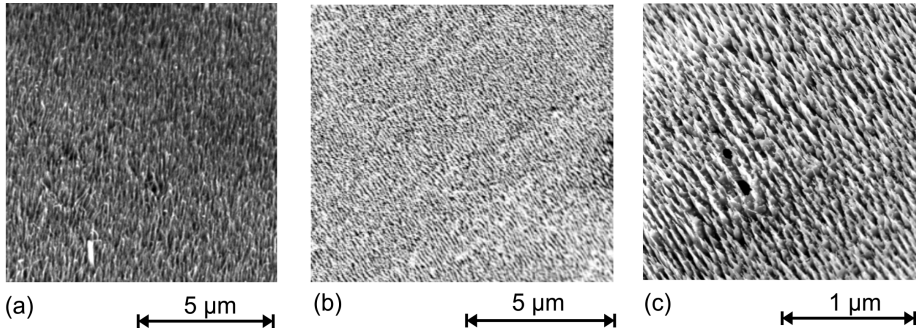


Figure 56: Beryllium (a) [68] and aluminium sample (b,c) after exposure to pure deuterium plasma

nations for this surface morphology. One possibility is the presence of impurities in the sample, which could be less efficiently sputtered than the actual sample material. If these impurities are present in nm-sized spots on the surface, they could suppress the erosion of the sample material below them, and therefore form grass-like structures. The other possible reason can be the angular dependence of sputtering yields. Since the surface is never perfectly flat, plasma ions hit some parts of the surface under a shallower angle than the standard incident angle normal to the surface. It is known that the sputtering yield can be increased if the incident ions are not hitting the surface perpendicular, but under a shallow angle. If the maximum sputtering yield is reached for very shallow angles, small surface irregularities can be "amplified" by the sputtering process, since the material is preferentially eroded in these regions. This is also the explanation given for the experiments at PISCES-B [69], and it is backed up by model calculations [70].

In the following parts of this section, first some further experimental results for the aluminium surface structure and comparisons to results with beryllium are given. Then, the possible causes for the observed surface morphology, which were mentioned above, are discussed in detail.

### Influence of plasma impurities

Figure 57 shows the aluminium exposures at PSI-2 with increasing argon impurities in the deuterium plasma. The argon concentrations given are always the impurity ion concentration, calculated with the method shown in section 4.1.5. It is clearly visible that argon has a great impact on the surface morphology. With only small

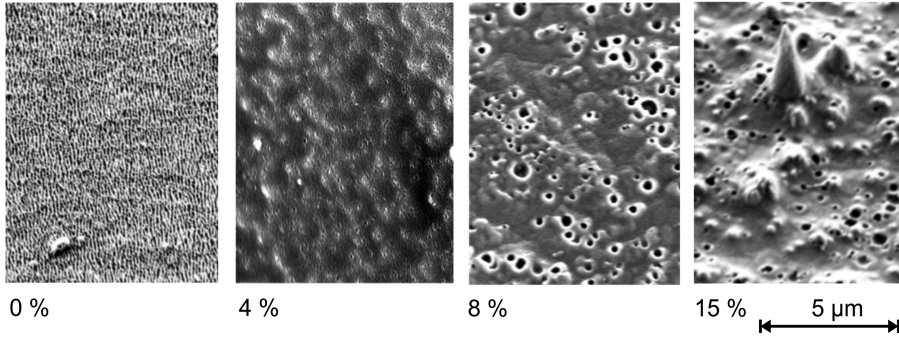


Figure 57: Aluminium samples after exposure with different argon impurity concentrations (all same magnification)

amounts of argon, the grass-like structure disappears and is replaced by a smoother, but slightly porous surface. With increasing argon impurity concentration, the pore size increases and also bigger structures, like the cone visible in the 15 % impurity case, appear. These cones can be up to  $5 \mu\text{m}$  high and therefore suggest a surface erosion of at least this depth. This is also confirmed by higher sputtering yields compared to the case with pure deuterium plasma, as it is later discussed in section 4.3.2.

A look at the surface with higher magnification reveals small spots, as seen in

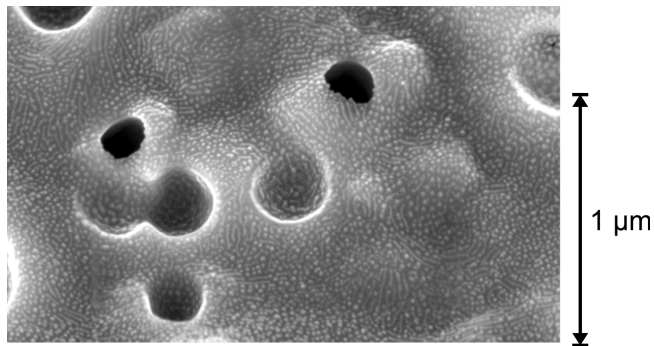


Figure 58: Aluminium sample after exposure to deuterium plasma with 6 % argon impurity

figure 58. The magnification being comparable to the high magnification picture of the pure deuterium exposure (figure 55) suggests that these points could be impurities in the material and act as the origins of the single grass-like structures. The

structures are just not developing under the presence of argon.

The comparison with the beryllium exposures to a mixed deuterium + argon plasma

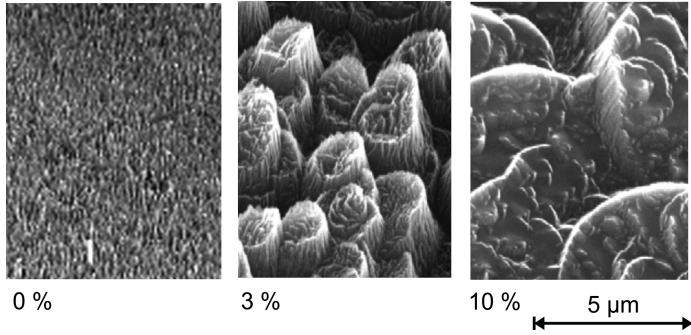


Figure 59: Beryllium samples after exposure with different argon impurity concentrations (all same magnification) [68]

at PISCES-B shows a similar suppression of the grass-like structure, but with different surface morphologies produced by the argon impurity. In figure 59, the surface morphology on beryllium with a low argon concentration exposure still has a coarse uneven structure. With higher argon concentrations, the surface gets flatter. There are no open pores or big cones visible, as it was the case with aluminium.

Figure 60 shows aluminium and beryllium samples after exposure to a pure argon

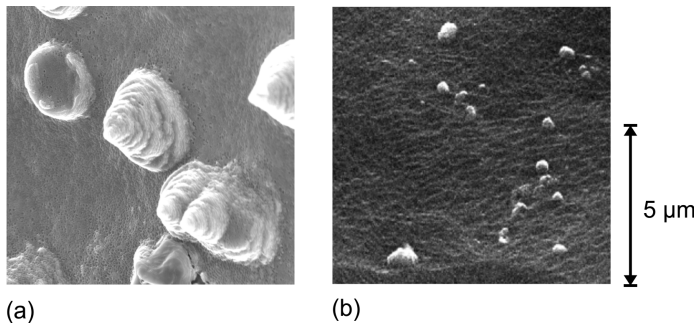


Figure 60: Aluminium (a) and beryllium (b) samples after exposure with pure argon plasma (all same magnification) [68]

plasma. Here, a smooth surface is visible for beryllium with a very low surface roughness. On the other hand, aluminium shows a smooth surface, which is interrupted by big cone structures.

The last image (figure 61) shows the surface morphology on aluminium for an exposure with helium plasma impurities. It is evident that there is no clear change in

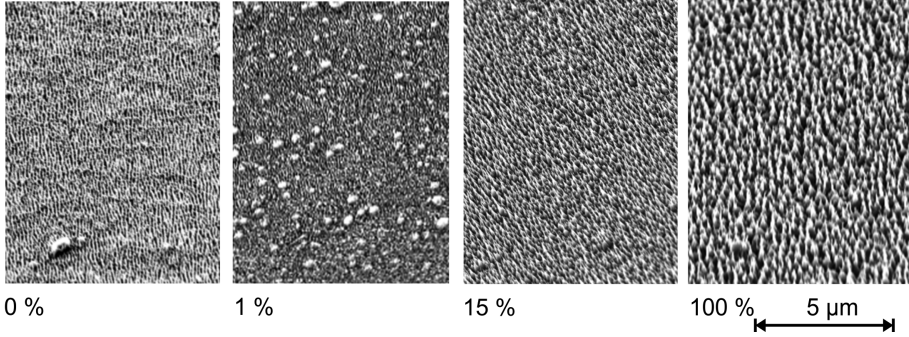


Figure 61: Aluminium samples after exposure with different helium impurity concentrations and pure helium plasma (100 %)

the surface morphology with helium impurities. Even for the pure helium exposure, the grass-like structure is still existing. The only visible difference is the change in the size of the structure: The thickness of the grass-like structures is increasing with increasing helium concentration. At PISCES-B, similar exposures were performed for beryllium samples to a pure deuterium and a pure helium plasma [69]. The results are similar in that also helium induces the grass-like structure on beryllium, but with an increasing thickness of the single structures.

### Causes for the development and suppression of the grass-like structure

To recap the results and explain the observed variation in surface morphology, one has to find out the reason for the development of the grass-like structure and its suppression by argon impurities. One explanation could be the presence of impurities in the sample material. Table 7 gives some sputter yields for aluminium, beryllium and probable impurities in the samples [71]. The difference in the sputtering yield for pure aluminium with deuterium or argon is only by a factor of two. This implies that the distinct change in surface morphology even with very little argon impurities is not originating from the difference in the sputtering yield for aluminium. This gets even more obvious when looking at beryllium, where the surface morphology changes in a similar way, but the sputtering yield for beryllium is much smaller with argon than with deuterium. Also, helium shows a higher sputtering yield than deuterium or argon for both materials, despite the surface morphology staying constant. That is why the variation in the sputter yields for aluminium alone cannot explain the change

	D	Ar	He
Al	0.004	0.008	0.018
Be	0.014	<0.001	0.029
Cu	<0.001	0.075	0.006
Si	<0.001	<0.001	0.004
Fe	<0.001	0.022	0.002

Table 7: Sputtering yields on Al, Be and some Al impurities for 40 eV incident ions

in the surface morphology. If one looks at possible impurities which could be present in aluminium, comparing the sputtering yields by deuterium for these materials reveals that their yields are much lower than the yields for aluminium or beryllium. On the other hand, the sputtering yield of argon is bigger for copper and iron than for aluminium and beryllium. This implies that argon impurities in a deuterium plasma could lead to a notable increase in the erosion of potential impurities in the target material. In contrast, helium is showing a similar behaviour like deuterium for the sputter yields on the different materials, and consequently shows a very similar surface morphology for deuterium plasmas with helium impurities.

Another explanation is the the angular dependency of sputtering yields for different incident ion species [69], which can cause the formation of the grass-like structure. It has been shown also by TRIM calculations [72] that the sputter yields have their maximum value not for an incident angle perpendicular to the surface, but for a more shallow incident angle. If the incident angle gets very shallow (closer to  $90^\circ$ ), a greater amount of incident particles will be reflected and cannot contribute to sputtering. If the incident angle is small (up to the perpendicular case for  $0^\circ$  incident angle), less particles are reflected, but the sputter yield is still not maximal. This is because the momentum of the incident particle is directed into the surface. To sputter a surface particle, the incident particle must cause a collision cascade which converts its momentum into the surface to a momentum of a surface particle out of the surface. This is more likely to happen for incident angles bigger than  $0^\circ$ , because the change of the direction of the momentum is getting smaller.

To calculate the optimal angle for maximum sputtering, an empirical formula for the angular dependence of the sputter yields by Yamamura [70] is used for the beryllium results [69]. The general formula is given in the following equation:

$$\frac{Y(\Theta)}{Y(0)} = \left( \frac{1}{\cos(\Theta)} \right)^f \cdot \exp \left[ -\Sigma \left( \frac{1}{\cos(\Theta)} - 1 \right) \right] \quad (28)$$

Here,  $Y(\Theta)$  is the sputtering yield by ions with an incident angle  $\Theta$ . Therefore the result of equation (28) is the ratio of  $Y(\Theta)$  over the sputtering yield with an incident angle perpendicular to the surface ( $\Theta = 0$ ).  $f$  and  $\Sigma$  are adjustable parameters which are used to fit the empirical formula to experimental data. The calculation of these values is described in reference [70] in detail. With the found dependencies of these values on factors like the sublimation energy or mass ratio of the substrate and impinging particles, one can apply the Yamamura formula to all elements. The model also distinguishes between sputtering by heavy and light ions. Heavy ions are supposed to sputter sample material by generating collision cascades in the sample when they hit the surface. With light ions, the sputtering is mainly caused by collision cascades generated from ions which are entering the surface and backscattered by the interior of the solid [73]. This difference has an influence especially for shallow incident angles and low ion energies.

Now the angular dependence of the sputtering yields is calculated for the cases

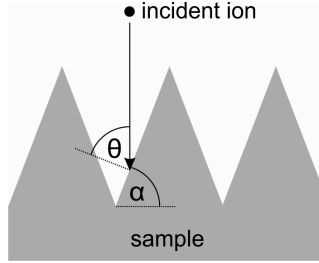


Figure 62: Relation between the angle of the grass-like structure ( $\alpha$ ) to the incident angle ( $\Theta$ )

which are discussed here. To find out if the optimal angle for sputtering has an influence on the formation and shape of the grass-like structure, the results are compared to the observed angles of the single grass structures, as shown in figure 62. Table 8 gives these experimental and theoretical values for beryllium as given in reference [69]<sup>1</sup>. and for aluminium. The results show a correlation between the optimal angle for sputtering and the angle of the grass-like structure. With an increasing mass of the sputtering ion species, the angle of the grass-like structure increases as well as the optimal angle for sputtering. However, the absolute values are not in a very good agreement. Probably a better way to compare the measurements with the model is not to find the angle for maximum sputtering yields, but

<sup>1</sup>The values given here are corrected. The original values in [69] are not correct due to an error in the application of the Yamamura model [74]

	Be (model)	Be (experiment)	Al (model)	Al (experiment)
Deuterium	72.6°	85.0°	69.9°	80.0°
Helium	61.9°	80.5°	57.0°	72.5°
Argon	53.6°	—	46.3°	—

Table 8: Calculated optimal angles (model) for sputtering vs. incident angle on the grass-like structure (experiment)

	Be (model)	Be (experiment)	Al (model)	Al (experiment)
Deuterium	84.7°	85.0°	83.7°	80.0°
Helium	80.1°	80.5°	78.0°	72.5°
Argon	74.2°	—	70.8°	—

Table 9: Calculated angles for  $Y(\Theta)/Y(0) = 0.5$  (model) for sputtering vs. incident angle on the grass-like structure (experiment)

the angle for a sputtering yield of a certain threshold value, for example 50% of the normal sputtering yield  $Y(0)$ . This could be interpreted as an angle at which the structures on the surface are less effectively eroded, while structures with smaller angles are preferentially eroded until they also reach the threshold angle. Therefore the resulting surface structure after the exposure is the grass-like structure with the threshold angle as its "steepness". The comparison of the angles is given in table 9. The results show that the calculated angles for  $Y(\Theta)/Y(0) = 0.5$  are much closer to the measured angles on the surface of the samples. Still, these calculations do not clearly explain the suppression of the grass-like structure for sputtering by argon, as the calculated angles are not very different to the calculated angles for helium. The plot of the angular dependence of the sputtering yields in figure 63 gives a more complete picture. The peak for the maximum sputtering yield is broader and has a lower amplitude for argon in comparison to helium or deuterium. Obviously, a certain increase between the maximum sputtering yield at the optimal angle and the sputtering yield at 0° incident angle is required for the formation of the grass-like structure. However, the plot also shows that the angular dependence of the sputtering yield for helium on aluminium is similar to the one for argon on beryllium. This suggests that not only the angular dependence of the sputtering yields is responsible for the suppression of the grass-like structure. An additional reason for the suppression might be the high mass of argon, which could lead to a stronger

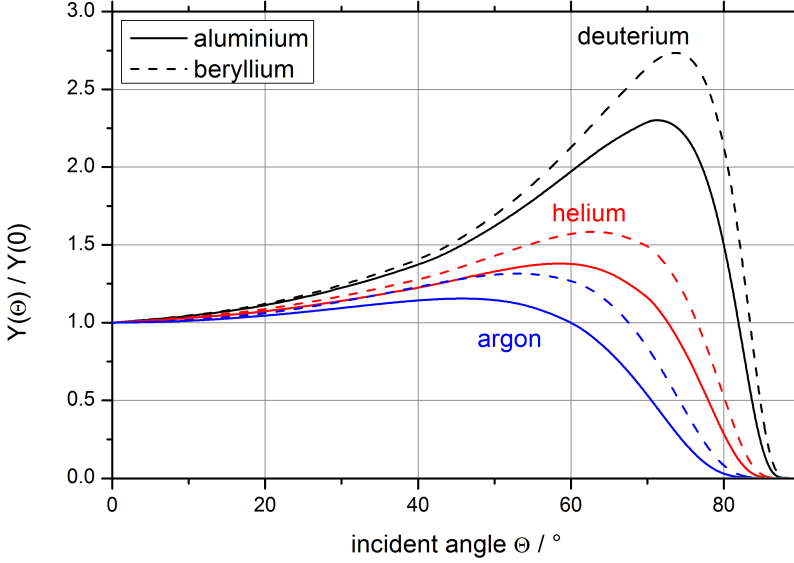


Figure 63: Angular dependence of the sputtering yields of deuterium, helium and argon on aluminium and beryllium

erosion of the tips of the grass structures. As mentioned earlier in this section, the sputtering mechanisms differ between light and heavy elements, and fine structures might be more prone to erosion by heavy elements. But to confirm this reason, more advanced TRIM simulations, with a 3-dimensional surface structure, would be required. Impurities in the aluminium sample, as mentioned in the first part of this section, could also play a role in the suppression of the grass-like structure by argon. However, a conclusion on the comparability between beryllium and aluminium can still be drawn: As the experimental results have shown, the surface morphologies of beryllium and aluminium are comparable regarding the formation of grass-like structures. The structures are formed when the samples are exposed to deuterium or helium plasma, and are suppressed by argon, with just a small amount of argon impurities in the plasma sufficient for the suppression of the structures.

#### 4.3.2 Sputter yields

For the aluminium samples, it has been found that the surface morphology and sputtering yields have a significant dependence on each other. In this section, the measurements for the sputter yields are presented and compared to numerical cal-

culations by the model SDTrimSP 5.00 [75]. The sputter yields were measured by weight loss of the aluminium samples. Figure 64 shows the results for all exposures in one plot. The plot shows that there is a notable increase in the sputtering

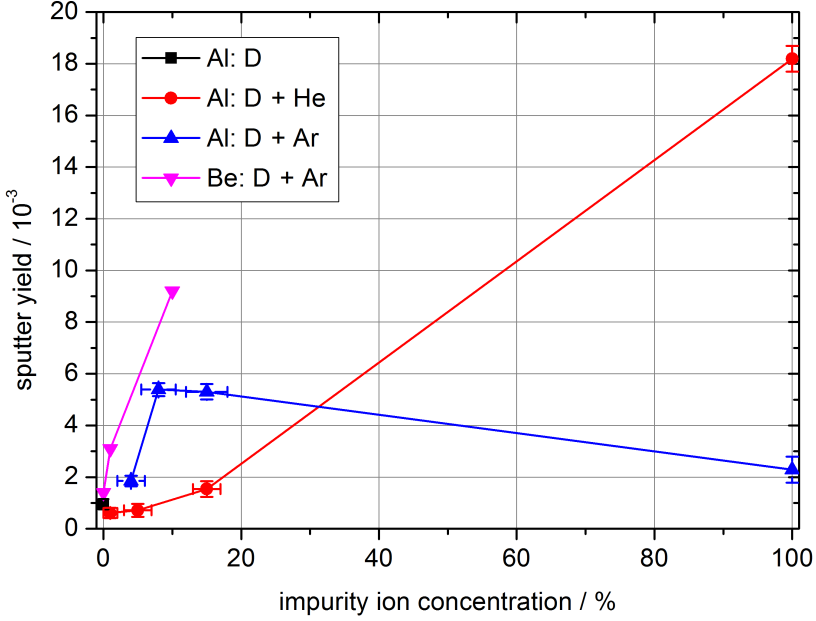


Figure 64: Sputter yields for exposures of aluminium and beryllium to deuterium plasmas with different impurities

yield with even small concentrations of argon impurities compared to the case with pure deuterium plasma. On the other hand, the sputter yield does not increase significantly for the cases of low concentrations of helium as an impurity. This is in contrast to the simulated values for the sputter yields given in the previous section. It is most obvious for the beryllium exposures, where the measured sputter yields rise, although the simulated sputter yields are much lower for argon on beryllium than for deuterium on beryllium. Therefore the total erosion has to be influenced by additional factors. As stated in the previous section, it is believed that impurities in the samples have lower sputter yields than the aluminium and beryllium. If argon is present as a plasma impurity, these sample impurities are sputtered more efficiently. But these sample impurities are only present as traces, and cannot be responsible for a rise in the total amount of sputter yields by factors of 5 to 10. However, the plasma impurities are also responsible for the surface morphology. The surface

morphology is supposed to be the main influence on the total erosion in this case: Figure 65 shows a simple model of the sample surface with a grass like structure and with a flat structure.

As it is pictured in this drawing, the effective erosion is much lower for the grass-

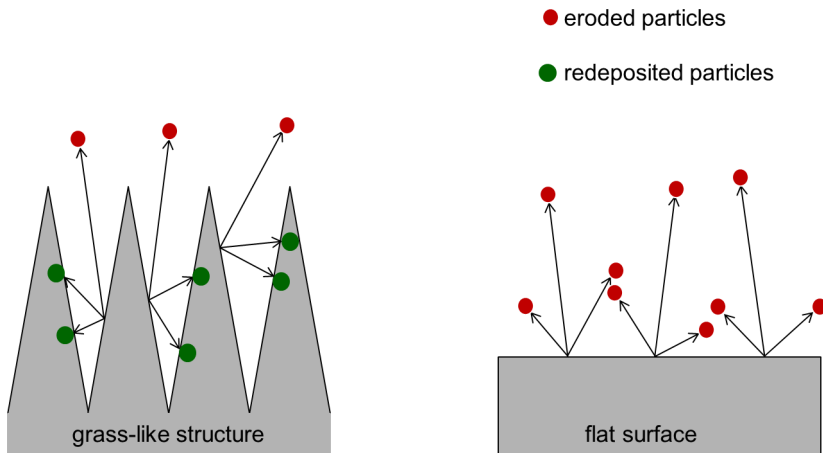


Figure 65: Erosion at a surface with grass-like structures and at a flat surface

like structure, because particles which are eroded on the sides of the structures, are easily redeposited on the protruding surface. On the flat surface, there are no such obstacles and the effective erosion is much higher.

This model is consistent with the measurements in figure 64: When the grass-like structure is present, like for the pure deuterium exposure or the exposures with helium impurities, the sputter yield stays low. But with argon as the impurity, the sputter yields rise. One exception is the case for the pure helium plasma. Here the sputter yield is very high, despite the presence of the grass-like structure. A possible explanation is the significantly higher sputter yield for helium on aluminium (compared to deuterium or argon). Probably for this case, the increased erosion due to the higher theoretical sputter yield exceeds the decreased erosion due to the grass-like structure. Also this aspect will be treated in the next figure: In figure 66, the theoretical values calculated with the TRIM code [75] for sputtering by deuterium, helium and argon are given. For these calculations, the ion impact energy is set to a mono energetic (which is valid due to the majority of the ion energy resulting from the bias voltage) value of 40 eV. The impact angle is perpendicular to the surface, and the composition of the impinging ions was set according to the measurements

for the plasma impurity concentrations (section 4.1.5). The plot shows that for a

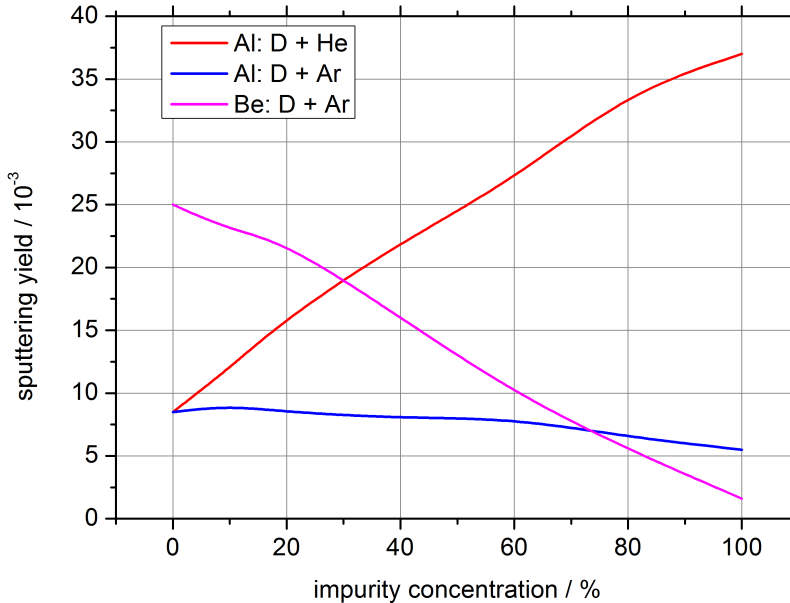


Figure 66: Sputtering yields by TRIM calculations for exposures of aluminium and beryllium to deuterium plasmas with different impurities

pure deuterium exposure, the measured sputter yields are lower than the predicted values by a factor of 10. With the addition of argon to the plasma, the measured sputter yields get much closer to the calculated values, especially for the aluminium samples. With an argon impurity concentration of 8 %, the measured sputter yield is already at 70 % of the predicted value. The data points for the beryllium samples show the same tendency, but the increase of the ratio is not so steep, reaching only 30 % for an impurity concentration of 10 %.

For the case of helium, the ratio stays at a low level for low impurity concentrations, with only a shallow increase even up to the case of a pure helium plasma. Remembering the data from figure 64, the measured sputter yield may be very high for the pure helium case, but this was also predicted by TRIM, as figure 66 shows. Therefore the grass-like structure, which is also visible for the pure helium exposure, still has the impact of reducing the sputtering yield even at high absolute sputter yields.

### 4.3.3 Deuterium retention

In the third part of the aluminium sample analysis, the deuterium retention of the aluminium samples is investigated. The aluminium samples were outgassed with a heating ramp of 0.6 K/s up to a temperature of 770 K. The data of the beryllium samples was provided by the TDS system at PISCES-B. To confirm the comparability of both systems, two aluminium samples were exposed at the same conditions at PSI-2 and outgassed, one in the local TDS system, the other one in the PISCES-B TDS system. The plasma exposure parameters are given in table 10: The resulting

no.	gas	$P_D$	$n_e$	$T_e$	$\Phi_i$	$\Gamma_i$	$T_S$
Al-1	D	9.8 kW	$1 \cdot 10^{18} \text{ m}^{-3}$	11 eV	$1.2 \cdot 10^{22} \text{ m}^{-2}\text{s}^{-1}$	$1 \cdot 10^{26} \text{ m}^{-2}$	380 K
Al-2	D	9.8 kW	$1.1 \cdot 10^{18} \text{ m}^{-3}$	11 eV	$1 \cdot 10^{22} \text{ m}^{-2}\text{s}^{-1}$	$1 \cdot 10^{26} \text{ m}^{-2}$	380 K

Table 10: Exposure parameters of samples Al-1 and Al-2

TDS spectra of both samples are given in figure 67. The shape and peak value of

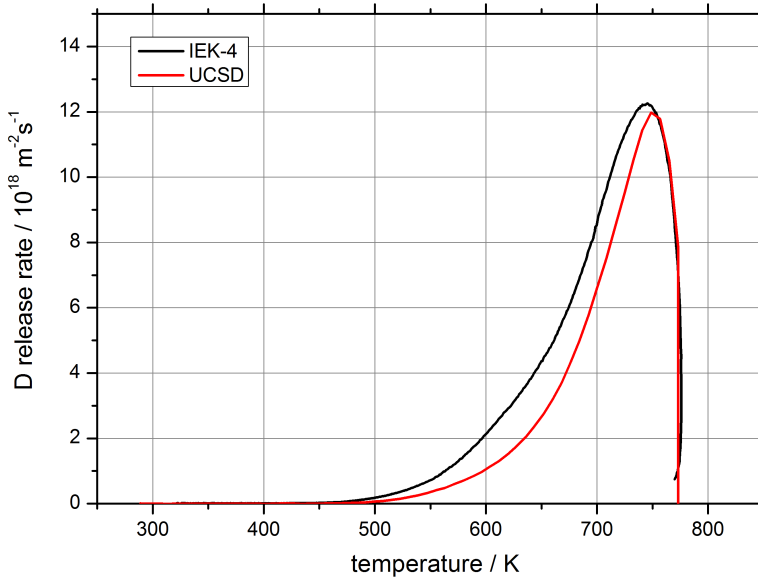


Figure 67: TDS spectra of aluminium samples Al-1 (black) and Al-2 (red) measured with the TDS systems at FZJ-IEK4 and UCSD respectively

the two TDS spectra are nearly identical, indicating a good agreement of both TDS systems. The shape of the spectra shows a steep decrease of the deuterium release at 770 K. This is solely an effect of the plotting versus temperature, because the heating ramp only goes up to a maximum temperature 500 °C. The ramp is stopped at this point to have some safety margin before the sample starts melting (melting point of aluminium = 660 °C). Hence all data points, after the maximum temperature is reached, are plotted at  $T = 780$  K. This is no issue for the calculation of the total deuterium retention, because this is done by integration over time, which is not affected by the heating ramp, assuming that there are no deuterium traps which need temperatures over 500 °C for detrapping. But for the evaluation of the temperature spectra, for example for the calculation of trapping energies, this part of the TDS spectrum must not be used. Figure 68 shows the TDS spectra for the

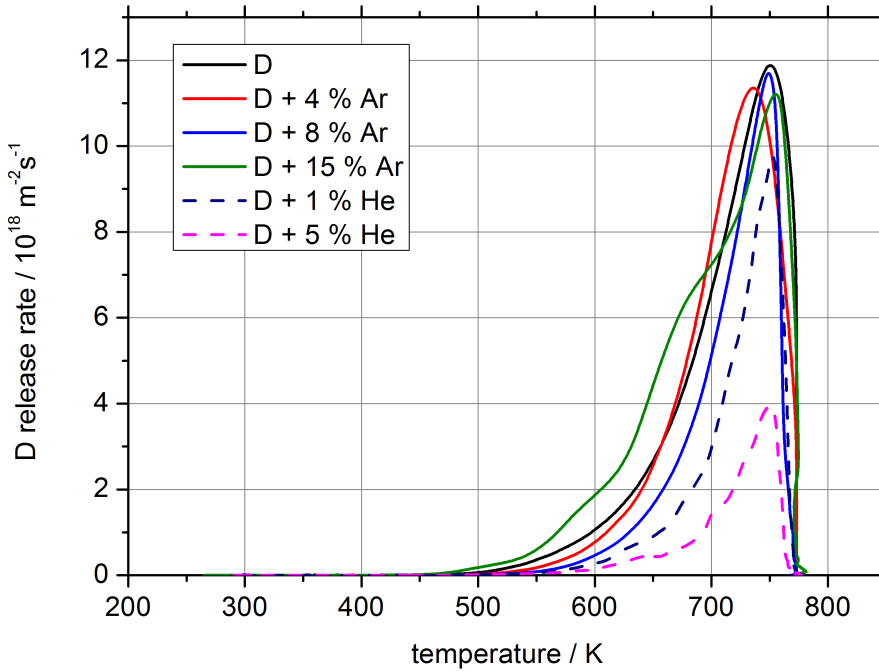


Figure 68: TDS spectra of aluminium samples exposed to deuterium plasma with different ratios of Ar or He impurities

aluminium sample exposures at PSI-2 regarding the variation of plasma impurity type and concentration. It is clearly visible that argon has no influence on the total deuterium retention, while helium leads to a decrease in deuterium retention.

no.	impurity	D retention	$E_{trap}$
Al-1	0 %	$2.45 \pm 0.25 \cdot 10^{21} \text{ m}^{-2}$	$2.16 \pm 0.32 \text{ eV}$
Al-3	4 % Ar	$2.26 \pm 0.23 \cdot 10^{21} \text{ m}^{-2}$	$1.37 \pm 0.35 \text{ eV}$
Al-4	8 % Ar	$2.71 \pm 0.31 \cdot 10^{21} \text{ m}^{-2}$	$2.45 \pm 0.41 \text{ eV}$
Al-10	15 % Ar	$2.09 \pm 0.30 \cdot 10^{21} \text{ m}^{-2}$	$1.05 \pm 0.42 \text{ eV}$
Al-7	1 % He	$1.69 \pm 0.28 \cdot 10^{21} \text{ m}^{-2}$	$2.47 \pm 0.31 \text{ eV}$
Al-8	5 % He	$7.32 \pm 0.25 \cdot 10^{20} \text{ m}^{-2}$	$2.57 \pm 0.32 \text{ eV}$

Table 11: Deuterium retention and trapping energies with different impurities

Besides the case of 15 % argon impurity, where there are some minor changes in the peak shape at the rising edge, all peaks show the same shape. In table 11, the results for the total retention and trapping energy are given. The trapping energies were calculated with the peak area method described in section 3.5. The trapping energy remains constant within the error margins. With argon, the total deuterium retention stays at a constant level. The trapping energy varies, but it is not clear if this is a definitive effect of a change in the trapping site type, or also an influence of the bigger errors due to the TDS spectra limit to 780 K.

The results imply that helium as a plasma impurity reduces the total deuterium retention. Because the shape of the TDS spectra are similar and the trapping energies are relatively constant, it can be assumed that helium impurities do not change the type of the trapping sites for deuterium. These effects were already discussed in section 4.2.2 in this work. Now the TDS spectra are directly compared to the corresponding beryllium exposures in PISCES-B. In figure 69, the TDS spectra of the beryllium samples are plotted. The TDS spectrum for the pure deuterium plasma exposure shows a very distinct peak at 500 K. This peak is caused by a supersaturation of deuterium in beryllium at high fluences [76]. In the cited publication it was shown that for low fluences ( $\Gamma_i \leq 10^{21} \text{ m}^{-2}$ ) deuterium trapping occurs at normal trapping sites with trapping energies at around 2 eV. This corresponds to a peak in the TDS spectrum at higher temperatures. This high temperature peak is hardly visible, but still present also in figure 69. If the fluence increases, a peak with lower trapping energy at around 500 K, as it is clearly visible in figure 69. This is explained in [76] by nanoscaled structural modifications due to the supersaturation of deuterium in beryllium. These modifications then bind the excess deuterium with a lower trapping energy.

With the addition of argon impurities, the single supersaturation peak splits into

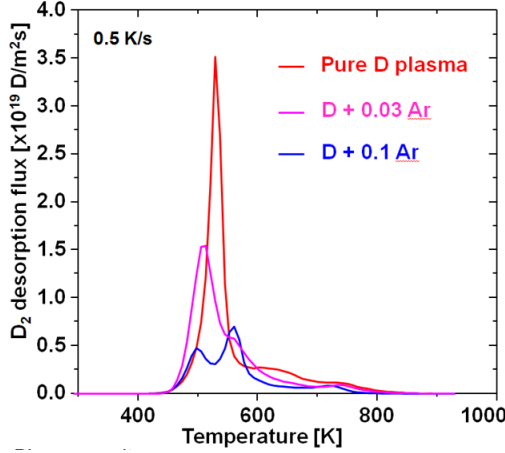


Figure 69: TDS spectra of beryllium exposures in PISCES-B with argon impurities [68]

two peaks, and the total amount of retained deuterium is decreased. The small peak at 750 K seems not to be affected by the argon impurities. It is assumed in [68] that the argon impurities influence the formation of the supersaturation binding states, and also reduce the total retention by ion-induced desorption.

The comparison of the results shows that the deuterium retention in beryllium at fusion-relevant fluences is dominated by supersaturation binding states, which are not present in the aluminium samples. Also, argon impurities distinctly influence the deuterium retention in those supersaturation binding states, while it does not influence the deuterium retention in aluminium. The conclusion of these findings is that aluminium is no suitable proxy material for beryllium with respect to hydrogen retention experiments. However, the results for the deuterium retention in aluminium can still be used for the interpretation of the results of the beryllium exposures. One possible explanation for the reduced deuterium retention in beryllium with argon impurities in the plasma is the reduction in the surface area by the suppression of the grass-like structure on the surface. The reduced surface area might simply provide less space for the deuterium to be trapped. But as the aluminium experiments showed, the reduction of the surface area did not decrease the deuterium retention in aluminium. This implies that also for beryllium, the reduced surface area by the suppression of the grass-like structures is not causing the reduction in the deuterium retention.

## 5 Modelling of deuterium diffusion in metals

Within the scope of this thesis, a diffusion model was developed. The aim of this model is to show the effects of helium or argon impurities in the deuterium plasma on the deuterium retention in tungsten. The results of this model can be compared to results of experiments presented in this work (total deuterium retention and surface modifications) as well as literature data like the implantation depth of deuterium. In contrast to models like TMAP [77] or CRDS [78], the model only focuses on the implantation and diffusion of deuterium, and not on the release of deuterium for example by TDS. Also, the trapping of deuterium is implemented by a local change of the diffusivity, with the one exception of trapping by helium in an additional trapping site profile. The model can only treat low-temperature sample exposures, where no thermal detrapping during the exposure can occur. While this is a more simple approach, it has to be noted that also codes like CRDS cannot directly simulate trapping sites and damages on a bigger scale than vacancies, like the porous structure by helium nanobubbles investigated here. Therefore, more complicated models would give no advantage in modelling the effects of helium nanobubbles on the deuterium retention.

The general purpose of this approach is to represent the deuterium diffusion in the most simple way, and then to implement the proposed effects of helium or argon impurities on the formation of additional trapping sites. The model uses free parameters for this implementation and can therefore not provide ab-initio calculations on the deuterium retention and helium/argon effects on the retention. First, the free parameters have to be matched in a way that the simulation results are comparable to particular experimental results, like the total retention and the reduction factor of the deuterium retention with helium impurities. But after this, single free parameters can be varied to test the influence of this single parameter. With these trends found by the model, predictions on the influence of certain factors on the deuterium retention, like the helium nanobubble layer thickness or the fluence, can be given. The central result of the diffusion model are one-dimensional density depth profiles of gas species in tungsten. The particles of density  $u$  diffuse according to the diffusion equation

$$\frac{\partial u}{\partial t} = \frac{\partial}{\partial x} \left( D(u) \frac{\partial u}{\partial x} \right) + R(u) \quad (29)$$

with  $D(u)$  as the local diffusivity.  $R(u)$  represents the reaction part with terms like the particle influx or loss, which are described later. The local dependence of the

diffusivity on the concentration  $u(x)$  is a simple way to implement the trapping of deuterium in tungsten. As pointed out in earlier works [7], the diffusivity of hydrogen in tungsten at low temperatures is smaller than the calculated Frauenfelder diffusion [12]. This is attributed to trapping sites in tungsten, which slow down the diffusion process and therefore reduce the effective diffusivity. Since the Frauenfelder diffusion is derived from experiments with high sample temperature ( $> 1000$  K), it is not affected by trapping effects, as deuterium in tungsten at this temperature has enough energy to stay untrapped. Hence, the trapping is implemented into the diffusion model as follows: First, the base diffusivity is set to a value some orders of magnitudes lower than the Frauenfelder diffusion. Then, the diffusion coefficient is set to increase linearly with the local deuterium density. This can be interpreted as a saturation of trapping sites, which lowers the effective density of trapping sites in the material and therefore increases the effective diffusion towards the Frauenfelder diffusion. Such a saturation of trapping sites can be assumed because modelling results of the hydrogen behaviour in tungsten have shown that the trapping energy of a vacancy decreases with an increasing number of hydrogen atoms already trapped at this vacancy [79]. This results in a certain maximum number of hydrogen atoms which can be trapped in a single trapping site. Of course this number might be exceeded in reality, for example by the formation of voids or blisters, which are able to trap a much higher number of hydrogen atoms or molecules. The formation of such blisters is not included in this model.

Other models like TMAP implement the trapping directly by a trapping-detrapping reaction in the reaction term  $R(u)$  and a fixed diffusivity for the mobile concentration  $u$  [80]. This incorporates the values for trapping site densities and trapping energies, which are required for the interpretation of TDS spectra with TMAP modelling. But as mentioned in the first paragraph of this section, the aim of the present model is to reproduce experimental results for the total retention and diffusion depth and profiles (when no impurities are present). As the results will show later, this is also possible with the more simple implementation without explicit trapping.

Of course, the actual value of the diffusion coefficient is difficult to measure and is also strongly dependent on the micro structure of the specific tungsten sample. Therefore, correct values for the base diffusivity and the increase of the diffusivity with the deuterium concentration are not chosen from literature or experimentally measured. Instead, the diffusivity is set to a value at which the simulation can reproduce the typical depth distribution of hydrogen in tungsten found in the literature. Here, results from [13, 81, 82] are used. The experimental results show a big scatter when the depth distribution of hydrogen is related to the total fluence, due

to variations of some orders of magnitude in the deuterium ion flux. As described in [15], with high deuterium flux, the deuterium concentration in the top surface of the samples will quickly rise to saturation, leading to higher surface losses. With low fluxes, a higher fraction of deuterium has enough time to diffuse into deeper regions of the samples, instead of recombining on the surface. This implies that the diffusion depth is actually depending on the exposure time of the sample, as it is also stated in the diffusion length derived from Fick's law,  $l = 2\sqrt{D\tau}$  [83], with  $l$  as the diffusion length and  $\tau$  as the time. When the diffusion depth from the experiments is plotted against their exposure time, this square-root dependency of the diffusion depth on the time is found, as shown in figure 70. In this graph, the depth

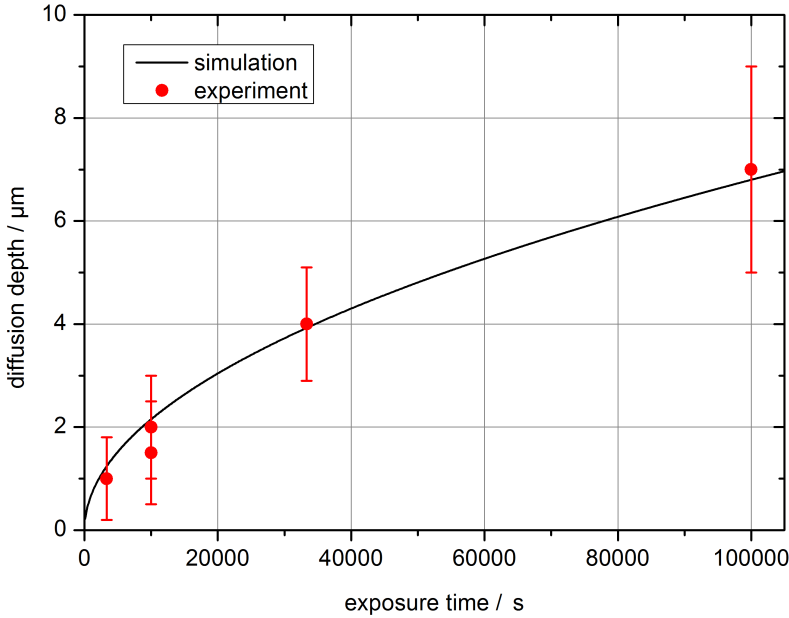


Figure 70: Calculated diffusion depth in comparison to experimental results from literature for deuterium in tungsten([13, 81, 82])

where the deuterium concentration reaches 1% of the deuterium retention on the top surface is plotted against the exposure time. The trend can be reproduced with the simulation when a diffusivity of  $1 \cdot 10^{-18} \text{ m}^2/\text{s}$  and an increase to  $1 \cdot 10^{-16} \text{ m}^2/\text{s}$  is used.

$R(u)$  contains the source and loss channels for deuterium. In this model, it consists of 2 parts: First, the input of deuterium into the sample. The depth profile of the

deuterium input is chosen to be one half of a Gaussian profile, with the peak at the surface of the sample. For the low energy exposures investigated in this work, the full width at half maximum is typically very shallow (a few nm) and depends also on the gas species. The integrated flux profile is the total flux. In the simulation, the flux represents the amount of deuterium which is actually penetrating the tungsten surface. This may be less than the total flux coming from the plasma, as deuterium can also be reflected on the surface. TRIM calculations give a reflection coefficient of 70 % [18] for deuterium at tungsten with 40 eV ion energies and an incident angle normal to the surface. But it has to be considered that the TRIM model is not very accurately representing the reflection factor at these low energies. TRIM uses a binary collision approximation, which is not valid anymore for such low energies. Other experimental results from [84] indicate that the reflection coefficient could be much higher, causing only a very small fraction of the incident ions actually penetrating the tungsten surface. In [84], it is assumed that this is caused by a chemisorbed layer of deuterium on the tungsten surface, which occurs at low sample temperatures and shields the tungsten from the incident deuterium ions. The effectiveness of this shielding depends on the incident ion energy. For unbiased samples, the results from [84] show that only  $10^{-3}$  to  $10^{-5}$  percent of the incident ions are penetrating the tungsten surface. For higher ion energies, the ratio is higher because the higher energy allows more ions to pass the chemisorbed layer. The reduction factor for the ion flux in the simulation is set by comparing the total deuterium retention from the exposures at PSI-2 (section 4.2) with the results of the simulation at different reduction factors. It was found that for the exposures at PSI-2 (with 40 eV ion energy), a reduction factor of  $1.32 \cdot 10^{-3}$  has to be applied on the ion flux to get the right order of magnitude for the total deuterium retention. This value fits between the results from [84] and the TRIM calculations. The model does not take the dynamic retention effects into account. Dynamic retention describes the release of deuterium directly after the exposure. It is mostly connected to solute deuterium in the sample, which can diffuse to the surface and leave the sample shortly after the exposure, while trapped deuterium stays in the sample. Most of this release occurs in the first hour after the exposure [85], therefore the TDS measurements from this thesis and also from most of the literature do not include this amount. The simulation does not distinguish between soluted deuterium and deuterium trapped in ordinary trapping sites, but its parameters like the diffusion coefficients and reflection factors are matched by comparison to TDS results which are only including the trapped deuterium. This leads to an uncertainty of the absolute value of these parameters. Eventually, the reflection factor

mentioned in the previous paragraph is actually higher than  $1.32 \cdot 10^{-3}$ , because the discrepancy between the simulation result and the TDS result for the deuterium retention is caused by the reduction due to dynamic retention. But the dynamic retention would require a full trapping-detrapping reaction implementation into the model [78]. As mentioned before, the aim of the simulation is not to reproduce or predict absolute values for, in this case, the reflection factor, but to give a simple representation of the diffusion of deuterium in tungsten. As a consequence, the dynamic retention is implemented only indirectly by a possibly higher reflection factor. The second part of  $R(u)$  is the trapping of deuterium in helium nanobubbles. As quoted in section 2.3, helium nanobubbles act as strong trapping sites for deuterium in tungsten. To implement this effect into the simulation, a second deuterium profile is introduced. This second profile does not diffuse in space but has a shape according to the shape of the helium profile. The population of the second deuterium profile is realized by a reaction in which deuterium flows from the original deuterium profile to the second deuterium profile. The flux depends on the concentration in the normal deuterium profile and the helium profile. The final deuterium concentration in the second deuterium profile is reduced by another reaction, representing the loss of trapped deuterium by recombination on the surface. A detailed interpretation of the implementation of helium nanobubbles into the simulation system is given in the next section 5.1.

### Implementation in MATLAB

The following part of this section gives a short overview about the implementation of the introduced features into a MATLAB [86] code. The complete source code can be found in the appendix (section 7). In the first part of the program, the definition of certain constants like the deuterium and helium flux, exposure time, size and size steps of the integration volume, and reaction rate coefficients for trapping. Then the main part follows, where the diffusion of the deuterium/helium is calculated and the deuterium/helium influx and trapping in the helium nanobubbles is performed. Periodically, the deuterium and helium profiles and the integrated amount of deuterium in the sample is saved to track the fluence dependency of the results. In figure 71, a graphic overview of the simulation sequence is shown.

The orange and pink arrows represent transport (influx, diffusion, trapping or loss) of helium or hydrogen. The red arrows indicate the influence of the local concentration of helium or deuterium on the diffusion and the trapping.

The numerical method used to solve the diffusion equation is the forward-time

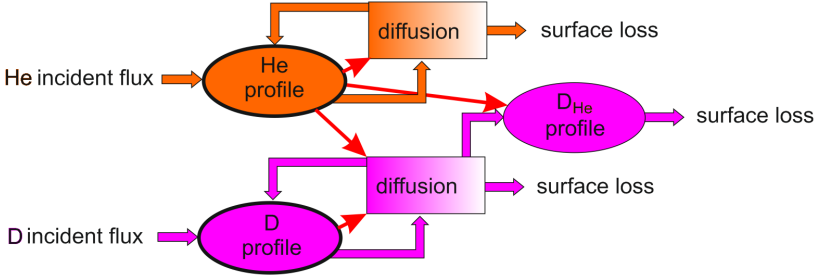


Figure 71: Scheme of the diffusion-calculation

central-space (FTCS) method [87]. As an explicit method, it is easy to implement, because it calculates values for a point in time  $t_{n+1}$  only with known values at a time  $t_n$ . The basic equation for calculating the value for the concentration  $u(x_i, t_{n+1})$  is:

$$u_i^{n+1} = u_i^n + \frac{D\Delta t}{\Delta x^2} (u_{i+1}^n - 2u_i^n + u_{i-1}^n) + \Delta t R(u_i^n) \quad (30)$$

with  $D$  as the diffusivity and  $\Delta t$  and  $\Delta x$  as the resolution in time and space. This equation is only suitable if the diffusion coefficient is not dependent on  $u$ . With  $D$  as a function of  $u$ , the first step of deriving (29) gives:

$$\frac{\partial n}{\partial t} = D \frac{\partial^2 n}{\partial x^2} + \frac{\partial D}{\partial x} \frac{\partial n}{\partial x} \quad (31)$$

Approximating these derivatives again with central differences in space and forward-difference in time yields the following result [88]:

$$u_i^{n+1} = u_i^n + \frac{\Delta t}{\Delta x^2} \left( \frac{D_{i+1}^n + D_i^n}{2} (u_{i+1}^n - u_i^n) + \frac{D_i^n + D_{i-1}^n}{2} (u_{i-1}^n - u_i^n) \right) + \Delta t R(u_i^n) \quad (32)$$

The FTCS method needs the following stability criteria to be fulfilled [87]:

$$\frac{D\Delta t}{\Delta x^2} \leq 0.5 \quad (33)$$

This expression basically states that the maximum stable  $\Delta t$  is the diffusion time across one cell of the spacial grid with  $\Delta x$ . As it is clearly visible, the temporal resolution has to be very high if also a high spacial resolution is required. To save computational time, the calculation is made with a variable temporal and spacial resolution. The temporal resolution can be easily changed between the time steps. But for the spatial resolution, equation (32) has to be changed again. For the simulation, the spatial grid is divided into two parts: the first 50 nm are calculated

with a high resolution of 1 nm per grid point. After 50 nm, the resolution decreases with:

$$\Delta x_{i+1} = a \cdot \Delta x_i, a = 1.07 \quad (34)$$

With this variation of the spatial grid, the FTCS method itself and also the implementation of  $D(u)$  has to be adapted, because now the average diffusion coefficient between  $x = i$  and  $x = i \pm 1$  has to be weighted to account for the different sizes of each grid point. The adaptation of the FTCS for a variable space grid with a constant diffusion coefficient yields the following equation [89]:

$$u_i^{n+1} = u_i^n + D\Delta t \left( \frac{a \cdot u_{i-1}^n - a \cdot u_i^n - u_i^n + u_{i+1}^n}{0.5 \cdot a(a+1)\Delta x_i^2} \right) + \Delta t R(u) \quad (35)$$

Here, the same 4 terms as in (32) can be recognized in the diffusion term of the equation. Now  $D$  is replaced by  $D(u)$ ; the new diffusion coefficient between two cells  $x_i$  and  $x_{i+1}$  with  $\Delta x_{i+1} = a \cdot \Delta x_i$  is:

$$D'_i = D_i^n + \frac{D_{i+1}^n - D_i^n}{a+1} \quad (36)$$

This gives the following result:

$$u_i^{n+1} = u_i^n + \Delta t \left( \frac{aD'_{i-1} \cdot u_{i-1}^n - aD'_{i-1} \cdot u_i^n - D'_i \cdot u_i^n + D'_i \cdot u_{i+1}^n}{0.5 \cdot a(a+1)\Delta x_i^2} \right) + \Delta t R(u) \quad (37)$$

To validate equation (32), a test is performed for a diffusion calculation along a uniform space grid ( $\Delta x = 10^{-9}$  m) and a space grid with a change in resolution as described above. All other factors (diffusivity, influx, time) are kept constant. As figure 72 shows, the calculated profiles are in agreement. This method of variable size steps can save much computation time in cases where the particles are expected to reach depths of several  $\mu\text{m}$ , but at the same time the shape of the profile of the first few nm is of interest. With variable size steps, instead of having to calculate the whole profile at high spacial resolution, the first nanometers can be calculated with high resolution, while the remaining part of the profile is calculated with lower resolution. As an example for the simulation results, figure 73 shows deuterium profiles for different fluences. The total deuterium retention is calculated by integrating the profiles. The results show that the deuterium content and the diffusion depths depend on the square root of the fluence, as it was also observed in experiments for constant sample temperatures. The width of the space grid is adjusted to a value which is always high enough so that no relevant deuterium concentration at the back end of the space grid will occur. This represents a sample which is thick enough to only exhibit surface losses at the front at the sample, and not at the back (no

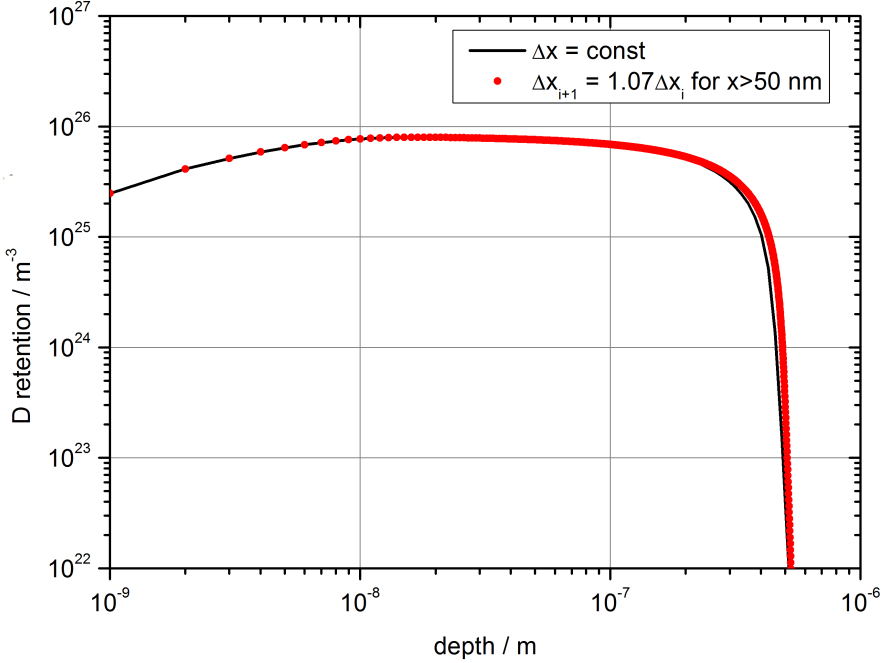


Figure 72: Calculated deuterium profile with constant and variable space grid steps

permeation).

In this model, the deuterium loss by recombination on the surface is not separately calculated, but implemented by fixing the deuterium density at the surface ( $x = 0$ ) to zero. By that boundary condition, instant recombination of any deuterium at the surface is assumed. This is feasible because the loss of deuterium at the surface is assumed to be diffusion-limited, not recombination limited [90, 91]. This can also be estimated by comparing the diffusion rate,  $R_D = D \cdot \frac{\delta u}{\delta x}$ , with the recombination rate  $R_R = K_R \cdot u^2$  [90]. If  $D = 1 \cdot 10^{-16} \text{ m}^2\text{s}^{-1}$  is chosen for the diffusion coefficient,  $\frac{\delta u}{\delta x} = \frac{10^{26} \text{ m}^{-3}}{2 \cdot 10^{-9} \text{ m}} = 5 \cdot 10^{34} \text{ m}^{-4}$  for the concentration gradient, and  $K_R = 10^{-31} \text{ m}^4\text{s}^{-1}$  as the worst case for the recombination rate coefficient reported in [90], the recombination rate is still orders of magnitudes higher than the diffusion rate ( $R_D = 5 \cdot 10^{18} \text{ m}^{-2}\text{s}^{-1}$ ,  $R_R = 1.0 \cdot 10^{21} \text{ m}^{-2}\text{s}^{-1}$ ). This makes the diffusion the limiting process for the surface losses.

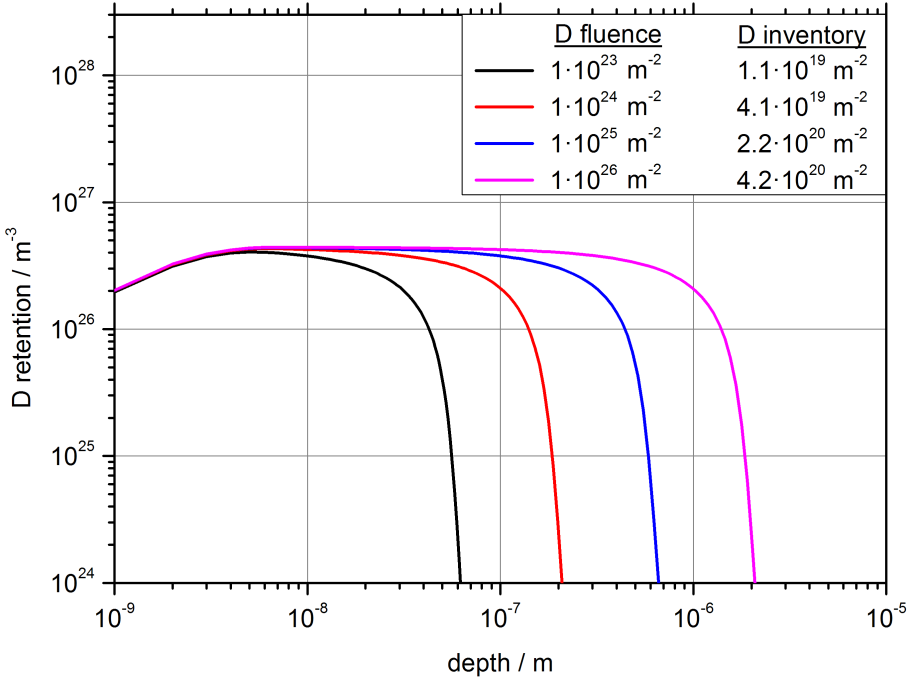


Figure 73: Deuterium profiles in tungsten for a deuterium flux of  $10^{22} \text{ m}^{-2}\text{s}^{-1}$  and mean implantation depth of 2 nm

## 5.1 Influence of helium nanobubbles

As introduced before, the helium nanobubbles [17] are implemented as an additional deuterium depth profile, called  $u_{D-He}$ , which represents deuterium trapped in or at helium nanobubbles in tungsten. The  $u_{D-He}$ -profile is "filled" by deuterium from the normal profile  $u_D$ . As a consequence, there is a loss term in  $R(u)$  for the deuterium profile:

$$R_{u_D} = f_D(x) - C_1 \cdot u_{He}(x, t) \cdot u_D(x, t) \quad (38)$$

$f_D(x)$  is the input flux profile of deuterium into the sample, and  $C_1[\text{m}^3/\text{s}]$  is the rate coefficient of the trapping of deuterium in the helium nanobubbles. The reaction rate of this reaction can be roughly estimated as  $C_1 = \langle \sigma v \rangle$  with the cross section  $\sigma$  and the diffusion speed  $v$ . The cross section is represented by the square of the lattice constant for tungsten,  $d = 0.316 \text{ nm}$ , and the diffusion speed by the diffusion

coefficient divided by the lattice constant  $v \propto D/d$ , with  $D \approx 1 \cdot 10^{-16} \text{ m}^2\text{s}^{-1}$ . The result for the reaction rate is  $\langle \sigma v \rangle = 3 \cdot 10^{-26} \text{ m}^3/\text{s}$ . This is in the same range as usual trapping rate coefficients used in the CRDS code, if the smaller diffusion coefficient in the present model is accounted for. In the estimation, the diffusion speed is used instead of the thermal speed, because the diffusion speed represents the thermal speed multiplied with the probability of the deuterium ion moving from one interstitial site to the next, which defines the reaction rate coefficients instead of the pure thermal speeds. For the profile  $u_{D-He}$ , which represents the deuterium trapped in helium nanobubbles, the loss term of  $u_D$  is the source term:

$$R_{u_{D-He}} = C_1 \cdot u_{He}(x, t) \cdot u_D(x, t) - C_2 \cdot u_{He}(x, t) \cdot u_{D-He}(x, t) \quad (39)$$

As equation (39) shows, there is also a loss term for  $R(u_{D-He})$ . This represents the loss of trapped deuterium to the surface due to the porous structure of the helium nanobubbles [17]. This loss term is proportional to density of helium  $u_{He}$  and the trapped deuterium in helium nanobubbles  $u_{D-He}$  and has another rate coefficient  $C_2[\text{m}^3/\text{s}]$ .  $C_2$  is typically smaller than  $C_1$ , due to the fact that helium in tungsten is generally a strong trapping site for deuterium [25]. On the other hand, the loss of deuterium due to the porous structure only occurs at high concentrations of helium, which are required for the development of the helium nanobubbles and the porous structure. At the low sample temperatures treated in the model, there is no reaction which transfers deuterium from  $u_{D-He}$  back to  $u_D$ . Instead, all deuterium which is removed from  $u_{D-He}$  is considered lost to the surface because of the porous structure of the helium nanobubbles at high helium densities.

The profile  $u_{D-He}$  is not diffusing ( $D_{u_{D-He}} = 0$ ), as this profile should only be existing where also the helium nanobubbles ( $u_{He}$ ) are present.

Both reactions introduced above are proportional to the helium profile  $u_{He}$ . The helium profile is set to be diffusing with a much lower diffusion coefficient  $D_{He} = 10^{-5}D_D$ . This condition is required to keep the helium profile limited to the first few nm below the surface, as it was shown in the experimental results (figure 49). But this very small diffusion coefficient exhibits a problem: the helium density can get very high ( $> 10^{30}\text{m}^{-3}$ ), because the losses by diffusion to the surface are drastically reduced. To achieve a more reasonable density, a loss reaction has to be implemented also for the helium profile  $u_{He}$ :

$$R_{u_{He}} = f_{He}(x) - C_3 \cdot u_{He}(x, t) \quad (40)$$

This loss can be interpreted in the same way as the loss term of  $R(u_{D-He})$  in equation (39): When the density of helium is so high that the helium nanobubbles form a

porous structure, the losses are increased in the same way as for deuterium. Because this is a first-order reaction, which is only dependent on a single reactant, the unit of  $C_3$  is  $\text{s}^{-1}$ . As a first result, figure 74 shows the results of this implementation for a deuterium flux of  $1 \cdot 10^{22} \text{ m}^{-2}\text{s}^{-1}$  and a deuterium fluence of  $1 \cdot 10^{26} \text{ m}^{-2}$  with and without 5 % helium impurities in the plasma. The applied rate coefficients are:  $C_1 = 8 \cdot 10^{-28} \text{ m}^3/\text{s}$ ,  $C_2 = 4 \cdot 10^{-28} \text{ m}^3/\text{s}$  and  $C_3 = 5 \cdot 10^{-2} \text{ s}^{-1}$ . These factors were found by matching the simulated reduction of deuterium retention to the measured reduction from the experimental results in section 4.2.3 by hand. The found rate coefficients differ about one order of magnitudes from the estimated rate coefficient. This can be explained by the uncertainty in the cross sections for this reaction used in the simple estimation. The plot shows two different cases: The black profile

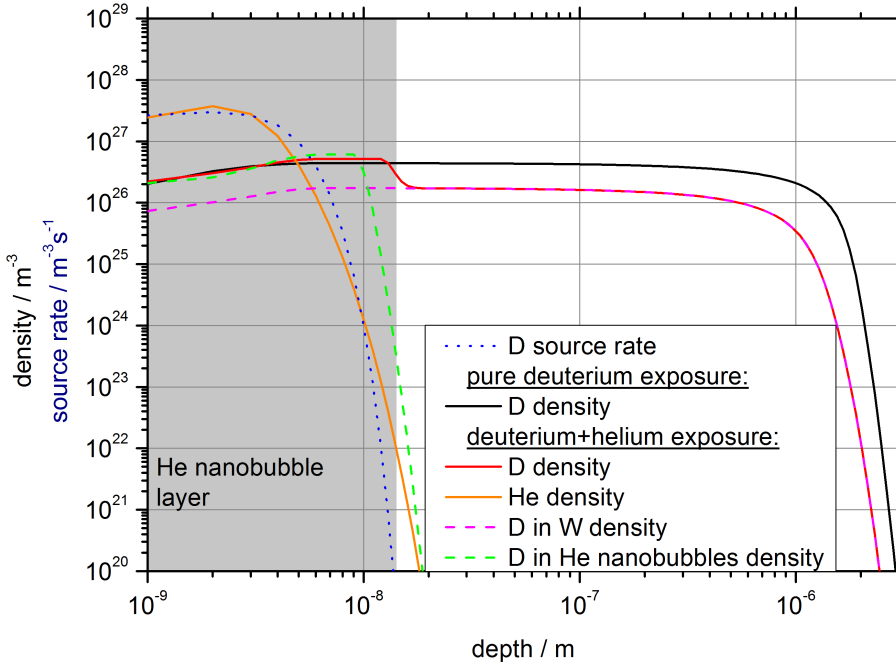


Figure 74: Simulated deuterium and helium depth profiles from exposures with and without 5 % helium impurities

is the result of a simulation without any helium impurities, hence only one deuterium profile is considered, which is diffusing according to the description in the previous section. By integrating the profile, the total retention is calculated to be  $4.2 \cdot 10^{20} \text{ m}^{-2}$ . The blue curve shows the deuterium input profile calculated with the

SRIM model [18] for 40 eV hydrogen ions on tungsten, which was then approximated by a gauss-shaped profile. The helium input profile uses the same shape, but with a reduced width of 50 % of the deuterium input profile width, and a total input reduced to 5 % of the deuterium input, according to the experimentally observed helium concentration in the plasma. The resulting deuterium profile with the presence of helium impurities is given by the red curve. The pink and green curves show how the total deuterium profile is composed by the deuterium trapped in helium nanobubbles and the deuterium trapped in ordinary tungsten trapping sites. The grey layer represents the depth of the helium nanobubbles as it was found in the TEM images in figure 49. In the area deeper than 12 nm from the surface, no relevant amount of helium is present and the deuterium is only existing in the normal, diffusing profile  $u_D$ . The trapping of deuterium in  $u_{D-He}$  cause a reduced deuterium concentration in the ordinary profile  $u_D$  in the deeper regions of the tungsten sample by a factor of around 3, and also a reduced diffusion depth. The integration of the total deuterium profile yields a deuterium retention of  $1.2 \cdot 10^{20} \text{ m}^{-2}$ , a reduction in the same range as it was found in the experiment. For the surface layer with the helium nanobubbles, the local retention is increased by the additional trapping in helium nanobubbles. The concentration is limited to  $5 \cdot 10^{26} \text{ m}^{-3}$  because of the loss reaction representing the losses due to the porous structure. The increase of

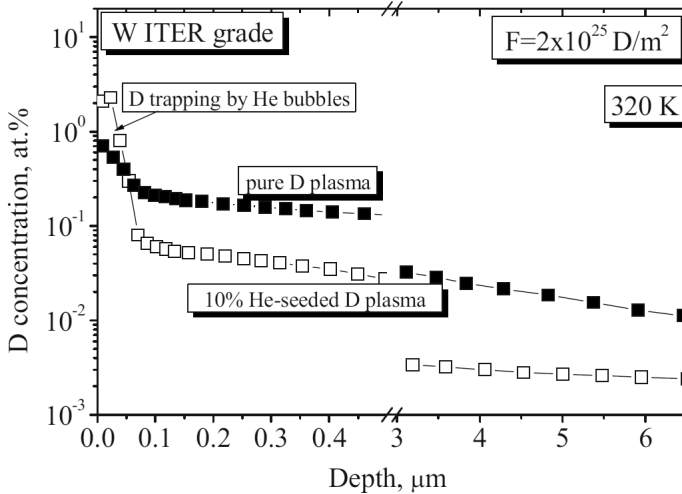


Figure 75: Deuterium depth profiles from [24] in ITER-grade tungsten with and without 10 % helium impurities at 320 K sample temperature

the deuterium retention in the surface layer, where helium nanobubbles are present, and the simultaneous reduction of the deuterium content in deeper regions of the sample was also found in experiments, as shown in figure 75 from [24]. Therefore, the approach of a trapping-detrapping reaction in the region with helium nanobubbles can not only reproduce the reduction in total deuterium content, but also the depth profiles from experimental results. The separate integration of  $u_{D-He}$  and  $u_D$  reveals that only 4 % of the total deuterium content is stored in the helium nanobubble profile  $u_{D-He}$  ( $4.6 \cdot 10^{18} \text{ m}^{-2}$ ). As it was shown with the TDS measurements from section 4.2.2, the TDS spectra show no evidence of trapping in trapping sites with different trapping energies, like helium nanobubbles. This complies with the low amount of deuterium trapped in the helium nanobubble profile  $u_{D-He}$ , which presumably would have also no visible effect on the TDS spectra shape.

## 5.2 Implementation of argon-induced defects

While the implementation of the helium nanobubbles in the previous section gives the results which were expected from literature, there are much less existing results on the influence of argon on the implantation and diffusion of deuterium in tungsten. The two major known differences are: The mass difference between argon and helium leads to ten times lower mean implantation depths for a given energy, as it was already shown in figure 6. This also agrees with the results from the TEM surface cross sections in figure 49, where the exposure with argon impurities yields only surface damages which are not deeper than for the exposure with a pure deuterium plasma. Second, the TDS measurements in section 4.2.2 have shown that the addition of argon impurities leads to an increase of the total deuterium retention. Also, the shape of the TDS spectra changes, indicating the creation of additional trapping sites by argon, which differ in their trapping energies from the ordinary trapping sites in tungsten. An additional obvious difference between helium and argon is the bigger sputter yield of argon. However, the sputtering is not implemented in the diffusion modelling. Therefore it must be regarded when analyzing the simulation results, if the given circumstances cause a relevant sputtering effect on tungsten. Now, with these informations, the simulation parameters which were used in the previous section about the helium nanobubbles are adjusted. The width of the input profile of argon is reduced to 5 % of the deuterium input file. The diffusion coefficient for the argon depth profile is reduced by a factor of  $10^7$ , compared to the

previous factor of  $10^5$  for the helium profile, to keep the argon depth profile very shallow and concentrated to the first few nm below the surface. The reaction rate of  $u_D$  has now a source term, which is the same as the loss term for  $u_{D-Ar}$ :

$$R_{u_D} = f_D(x) - C_1 \cdot u_{Ar}(x, t) \cdot u_D(x, t) + C_2 \cdot u_{Ar}(x, t) \cdot u_{D-Ar}(x, t) \quad (41)$$

This means that the deuterium detrapped from  $u_{D-Ar}$  is not lost to the surface due to a porous structure, but re-entering the tungsten lattice as it would be the case for any other normal trapping site in tungsten. Of course, it cannot be excluded from the single TEM image in figure 49 that also argon produces a porous structure. However, the detrapping into the tungsten lattice is no necessary condition to reproduce the results as shown next. The results can also be reproduced if it is assumed that also argon impurities form a porous structure like helium. The applied rate coefficients are:  $C_1 = 5 \cdot 10^{-28} \text{ m}^3/\text{s}$ ,  $C_2 = 5 \cdot 10^{-30} \text{ m}^3/\text{s}$  and  $C_3 = 0.02 \text{ s}^{-1}$ , which causes a much lower trapping of deuterium in the profile  $u_{D-Ar}$ , as well as a lower loss rate from this profile. The result is displayed in figure 76. Again, the black profile

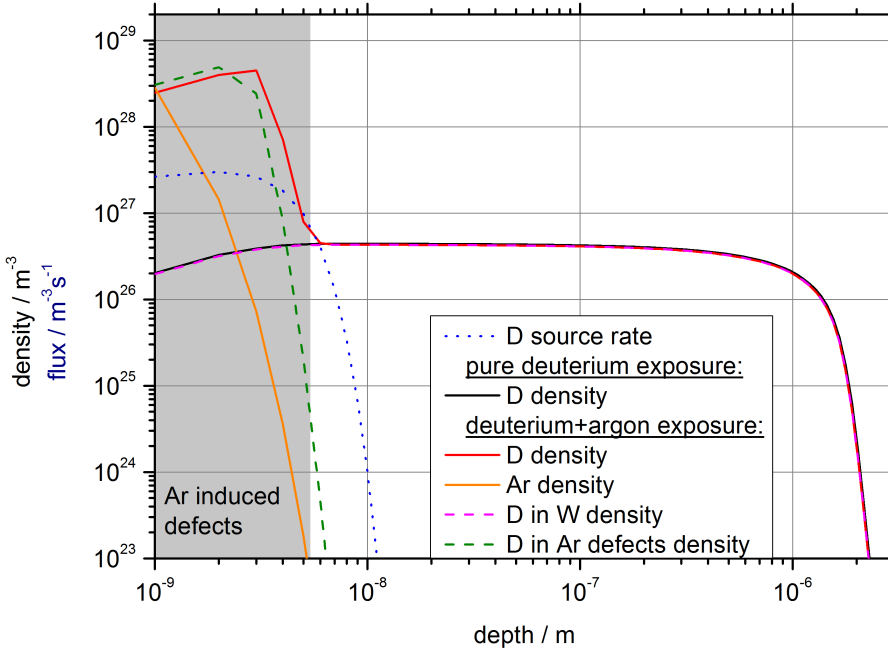


Figure 76: Simulated deuterium and argon depth profiles from exposures with and without 5 % argon impurities

is the result of the simulation without any argon impurities for comparison. The blue curve shows the deuterium input profile. The resulting deuterium profile with the presence of argon impurities is given by the red curve. The pink and green curves show how the total deuterium profile is composed by the deuterium trapped in the presumed additional defects by argon impurities, and the deuterium trapped in ordinary tungsten trapping sites. The argon depth profile was fitted to the depth of the damaged layer as it was found in the TEM images in figure 49, indicated by the grey layer in the graph. The corresponding additional deuterium profile  $u_{D-Ar}$  is increasing the local deuterium concentration where the argon concentration is relevant. But because the deuterium input profile reaches much deeper than the argon profile, the normal deuterium profile is only influenced in the first few nm of the depth profile. In the deeper regions, the profile stays almost the same, regarding the amplitude as well as the diffusion depth. The integrated deuterium retention reveals an increase for the case with argon (total retention  $5.1 \cdot 10^{20} \text{ m}^{-2}$ ), reproducing the experimental results from section 4.2.2.

### 5.3 Fluence dependency

In this section, the fluence dependency of the deuterium retention with He, Ar and without impurities is investigated. Figure 77 shows the total deuterium retention between  $1 \cdot 10^{23} \text{ m}^{-2}$  and  $2 \cdot 10^{26} \text{ m}^{-2}$  for the same cases investigated in the previous two sections: Pure deuterium exposure, deuterium+helium exposure and deuterium+argon exposure. The symbols show the experimental results from section 4.2.3. For the exposure with argon impurities, only a single data point is available. The simulation shows a similar increase in the total deuterium retention for this fluence. The increase is of course depending on the choice of rate coefficients for the trapping of deuterium in the profile  $u_{D-Ar}$ . The other influencing factor is the thickness of the argon layer directly below the surface. As explained in the previous section, a deeper layer of argon would be able to trap a bigger amount of deuterium. But because the layer thickness is known from TEM images, the increase in deuterium retention is matched to the experimental values primarily with the rate coefficients. The result with these rate coefficients, which reproduce the measured increase of deuterium retention at  $1 \cdot 10^{26} \text{ m}^{-2}$ , imply an constant increase of the total deuterium retention over the whole fluence range.

With helium as the plasma impurity, the simulation is able to reproduce the experimentally measured values along the whole range of fluences. At low fluences, it

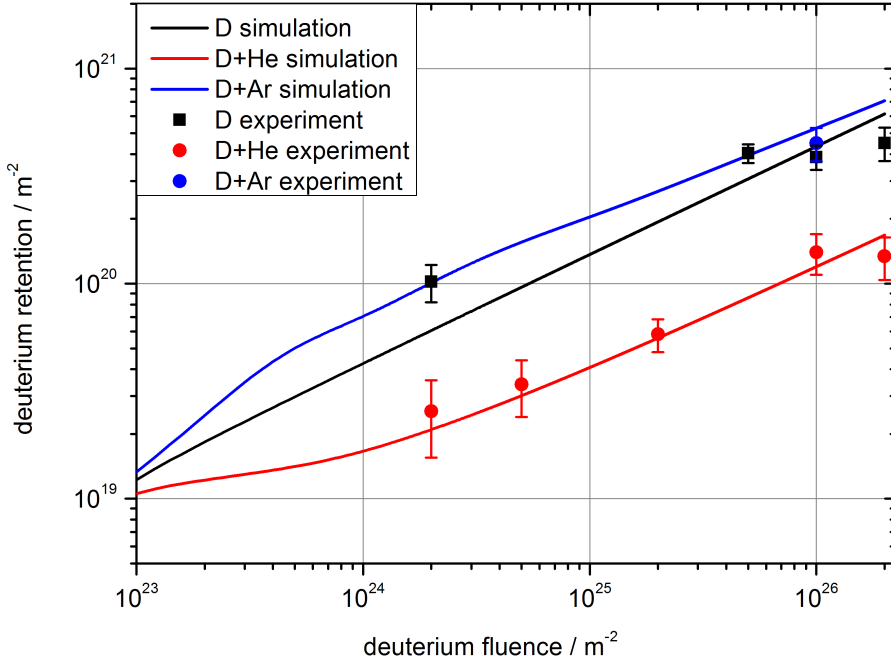


Figure 77: Simulated deuterium retention in dependence of the deuterium fluence with and without 5 % helium or argon impurities

shows that the influence of helium impurities on the deuterium retention is increasing with fluence. While the reduction of the deuterium retention gets bigger up to a fluence of  $2 \cdot 10^{24} \text{ m}^{-2}$ , it starts to get constant for fluences above this value. This is related to the very small to almost non-existent growth of the helium profile depth at the high fluences. In the simulation, the growth of this profile is limited because of the loss term introduced in equation (40). When the helium density gets very high, the loss of helium gets high enough to compensate the helium input from the incident plasma, and the profile becomes stationary. By that, the trapping rate of deuterium in the profile  $u_{D-Ar}$  and therefore also the reduction factor of the total deuterium retention gets constant. Because also the experimental results show the same behaviour at high fluences (the datapoints for D+He exposure rise with the same slope as the datapoints for pure deuterium exposure), it can be concluded that the constant width of the helium profile at fluences above  $1 \cdot 10^{25} \text{ m}^{-2}$  is also the case in the experiment. A comparison with an increased helium diffusion depth in

figure 78 show the dramatic influence of the helium depth profile on the deuterium retention. The change in the helium depth profile was realized by a change in the

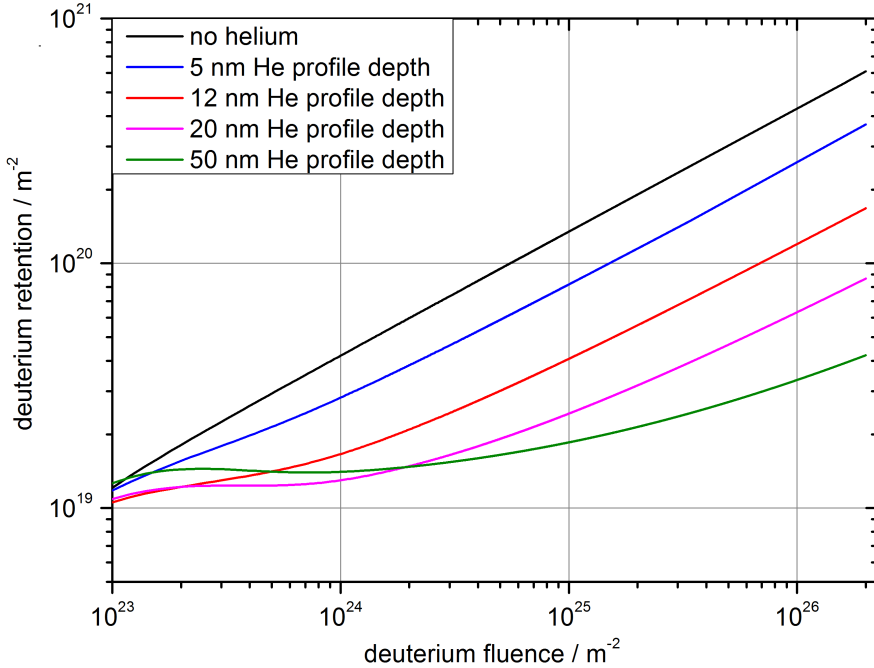


Figure 78: Simulated deuterium retention in dependence of the deuterium fluence with and without 5 % helium impurities at 4 different helium depth profiles

helium diffusion coefficient. The depths given in the legend are the depths of the helium profile reached at a deuterium fluence of  $1 \cdot 10^{26} \text{ m}^{-2}$ . The depth of 12 nm is the case which is also shown in the previous section in figure 74. For a very shallow helium profile depth of only 5 nm, the reduction factor for the total deuterium retention is decreased over the whole fluence range. With a helium depth of 50 nm, which is deeper as the deuterium input profile, the total deuterium retention is increased compared to the case of a 12 nm helium profile depth up to a fluence of  $5 \cdot 10^{23} \text{ m}^{-2}$ . This is caused by the stronger diffusion of helium, which leads to a higher total amount of helium in the sample, and therefore also a higher trapping rate into the profile  $u_{D-He}$ . From here, the deuterium cannot diffuse to the surface anymore, and the total deuterium retention is increased. But the local concentration in the helium

profile and  $u_{D-He}$  is not yet high enough for the a significant loss of deuterium due to the porous structure. For fluences higher than  $5 \cdot 10^{23} \text{ m}^{-2}$ , this situation changes, as the loss due to the porous structure becomes the dominant reaction, significantly decreasing the deuterium retention at the higher fluence range. In the experiment, the deeper helium depth profile, which also represents a thicker helium nanobubble layer, can be caused for example by higher sample temperatures [23]. At higher sample temperatures of about 500 K, the helium nanobubble layer is already deeper than the 10-15 nm layer observed in the present samples exposed at 380 K. The

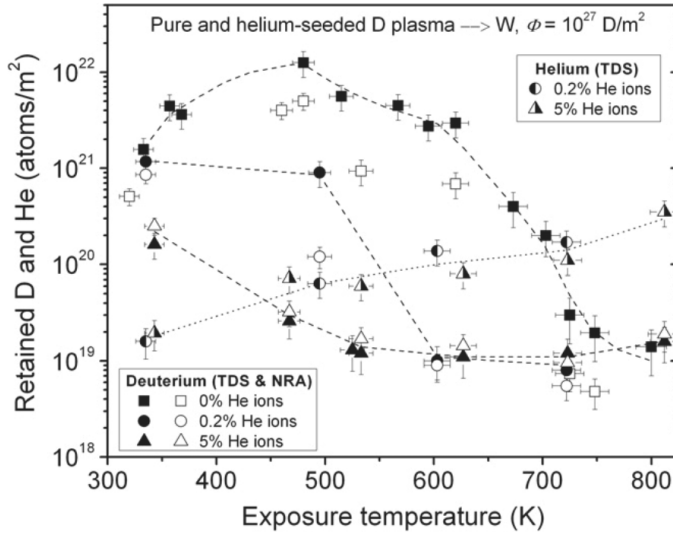


Figure 79: Total deuterium retention in tungsten with and without helium impurities under variation of the sample temperature [13]

results from [13] in figure 79 show that the total deuterium retention with helium impurities at 500 K sample temperature is indeed decreased by one order of magnitude compared to the exposures at 350 K. If the helium layer is assumed to continue growing all the time, which might be the case for even higher temperatures [22], a saturation of the total deuterium content can be proposed. But then, the temperatures have also already reached values which cause a significant decrease of the total deuterium retention just by the temperature (1400 K for the case in [22]).

All in all, the simulation has shown that the thickness of the helium nanobubble layer might be the most important factor in the reduction of the deuterium retention by helium impurities. Of course, the helium nanobubble layer thickness has to be viewed in relation to the deuterium penetration depth. But a deep penetration

depth of deuterium with a shallow helium nanobubble layer at the same time is unlikely for the incident ion energy of less than 100 eV, which is the relevant range for the divertor region in the tokamak.

## 6 Conclusions

The main topic of this thesis is the influence of helium and argon impurities in a deuterium plasma on the deuterium retention in metals. For that purpose, tungsten and aluminium samples are exposed to such plasmas in the linear plasma generator PSI-2. The analysis of these samples is performed mainly by thermal desorption spectroscopy for the deuterium retention and scanning electron microscopy for the surface morphology of the samples. For the control and measurement of the impurity ion content in the plasma, measurement methods by optical emission spectroscopy are established at PSI-2 in the framework of this thesis. To understand the mechanisms behind the influence of helium or argon on the deuterium retention, a numerical diffusion model is developed, which calculates the diffusion of deuterium in tungsten and the trapping in helium- or argon-induced defects. The following paragraphs summarize the results of these experiments and calculations.

### **Measurement of the impurity ion content by optical emission spectroscopy**

The optical emission spectroscopy has been proven to be an important diagnostic tool at PSI-2. The results of the experiments for the diagnostics of plasma parameters have shown that the optical emission spectroscopy can be used to measure plasma parameters like the electron density and electron temperature in "standard" deuterium plasmas as well as in recombining plasmas. The most important aspect of the optical emission spectroscopy measurements for this thesis is the measurement of impurity ion concentrations in the plasma. For argon as a plasma impurity, a method was applied which calculates the argon ion ratio from an  $\text{Ar}^+$  spectral line at 434.8 nm. At argon gas input ratios below 5 %, the resulting deuterium to argon ion ratio is about the same as the gas input ratio of deuterium and argon. With increasing argon gas input, the argon ion content rises slower than the the argon gas input. Therefore, the spectroscopic measurement is required to get a more accurate value of the argon ion content than just estimating it from the gas input ratio.

For helium as a plasma impurity, a different method was applied, which calculates the helium ion ratio from the intensity of a neutral helium spectral line at 447.1 nm. The results of this method show that the helium ion ratio is even lower with respect to the helium gas input as it was the case with argon. This effect is a result of the higher ionization energy of helium compared to deuterium, which decreases the helium ion ratio in deuterium plasmas with lower electron temperatures. Only if the

helium gas input is dominating (80-100 %), the higher electron temperatures cause a steep rise of the helium ion content in this parameter range. Again, the measurement of the helium ion to deuterium ion ratio by spectroscopy has been proven to be required for reliable results of the impurity ion concentration in the plasma.

### **Experimental studies of deuterium retention in tungsten**

The experiments with tungsten samples in PSI-2 investigated the influence of plasma impurities on the deuterium retention.

The exposed samples are analyzed regarding their surface morphology by SEM/TEM imaging. It was shown that the exposure to pure deuterium plasmas causes surface roughness on the nm-scale, which is interpreted as surface modifications due to deuterium retention in the first few nm of the sample surface. For the case of argon impurities, the increased sputtering yield for argon leads to a smoother surface due to erosion of the previously mentioned surface modifications.

With helium impurities, the surface is getting smoother as well, but here it is caused by the reduced deuterium retention by helium. The main effect of the helium impurities is visible in TEM cross section images of the surface: For the exposure with helium impurities, a layer of about 12-15 nm is visible at the surface. This layer is caused by the formation of helium nanobubbles in the tungsten surface. For the cases without any impurities and with argon impurities, only a very shallow damaged layer of  $< 5$  nm is visible. This damaged layer is probably caused by stress damages induced by high deuterium concentrations in the surface region. The helium nanobubble layer leads to a reduction of the deuterium retention. The reduction of the deuterium retention by helium impurities is one of the most important effects investigated in this thesis. A reduction by a factor of 3 was measured for the exposures at a sample temperature of 380 K. Literature values show an even stronger reduction when the sample temperature is higher. At higher temperatures, there is an increased formation of helium nanobubbles, which increases the total reduction of deuterium retention. This is an important result which shows that also at low temperatures, where only a very shallow helium nanobubble layer is present, a significant reduction of the deuterium retention can still be expected. From the shape of the TDS spectra, where no change was observed for the exposures with and without helium impurities, it can be concluded that the type of trapping sites, where deuterium is retained, remains unchanged, while only the total amount of trapped deuterium is decreased.

For the exposures with argon impurities, a different behaviour was observed. In contrast to the helium impurities, the addition of argon impurities increased the

total deuterium retention by 30 % for 8 % argon impurities in the plasma. Also, the shape of the TDS spectra changed, which indicates that additional trapping sites are formed by the argon ions. Because of the higher mass of the argon ions, they are more likely to produce ion induced defects at the surface of the tungsten samples, which can act as trapping sites for deuterium.

### **Numerical simulation of the deuterium diffusion in tungsten**

For a better understanding of the effects of helium and argon impurities on the deuterium retention, a diffusion model for deuterium in tungsten was developed in this work. Based on the results from the TEM imaging of the tungsten samples, the depth profile of the helium nanobubbles and the argon-induced damages is known and implemented into the simulation. The results show that the difference in the deuterium retention between D + He and D + Ar exposures is mainly caused by the difference in these depth profiles: The argon-induced damages are limited to the first 5 nm. This layer can influence the incident deuterium by providing additional trapping sites for deuterium. But most of the deuterium is able to pass this layer and diffuse into deeper regions of the sample. Consequently, the simulated depth profile remains mostly unchanged when compared to the depth profile for a pure deuterium exposure, with the exception of an increased deuterium retention in the first 5 nm of the surface due to trapping in the argon-induced damages. This also leads to the increased total deuterium retention which was observed in the experiments.

For the exposures with added helium impurities, the layer with helium nanobubbles is thicker (12-15 nm). Therefore, it has a much bigger influence on the incident deuterium. Only a small amount of deuterium is able to diffuse from the helium nanobubble layer into deeper regions. Thus, the deuterium amount below the helium nanobubble layer is smaller and does not reach the same depth as with the pure deuterium exposure. This is also backed up by experimental results from literature. The majority of the deuterium is trapped in the helium nanobubble layer. For the reduction of the total deuterium retention observed in the experiments, the deuterium content trapped in the helium nanobubbles has to be reduced. The physical mechanism for this reduction is surface recombination, because for a certain density of helium nanobubbles, this layer can be assumed to be porous with open paths to the surface. The reduction of deuterium trapped in helium nanobubbles is also required to explain the unchanged TDS spectra from the experimental results, which indicates that no relevant amount of deuterium is trapped in additional defects like helium nanobubbles.

With the diffusion simulation, also the fluence dependency of the deuterium retention could be investigated. In the experiments, no saturation of the total deuterium retention could be observed for pure deuterium exposures or for deuterium + helium exposures up to a fluence of  $2 \cdot 10^{26} \text{ m}^{-2}$ , and the total retention is decreased by a factor of 3 for the whole fluence range between  $2 \cdot 10^{24} \text{ m}^{-2}$  and  $2 \cdot 10^{26} \text{ m}^{-2}$ . In the simulation, it was found that the reduction factor is also constant at fluences above  $1 \cdot 10^{24} \text{ m}^{-2}$  and depends on the thickness of the helium nanobubble layer.

The main conclusion of these results is that the reduction of the total deuterium retention by helium depends on the porous structure produced by the helium nanobubbles, and the depth of this helium nanobubble layer. It has to be deep enough for a significant reduction of the total deuterium retention. The experimental results in this thesis show no saturation effect because the helium nanobubble layer stayed shallow due to the low energy, low temperature exposure. This can be reproduced in the simulation by a saturation of the helium nanobubble layer depth. Argon has a smaller influence on the total deuterium retention because of its very shallow depth profile.

### **Experimental studies of deuterium retention and erosion of aluminium and beryllium**

To investigate the suitability of aluminium as a proxy material for beryllium, the experiments with aluminium samples were performed. Although a different element can be expected to yield different results in plasma-wall-interaction studies, a proxy material for beryllium could help investigating particular aspects without the problems of the toxicity of beryllium. The focus is again on the influence of plasma impurities. The results of the aluminium exposures regarding surface morphology, sputtering rates and deuterium retention were compared to results of beryllium exposures at PISCES-B. For the surface morphology, it was found that the exposure to a pure deuterium plasma forms a grass-like structure on the aluminium surface. The same structures were also observed on beryllium.

The structures are formed because the sputtering yields of deuterium on aluminium and beryllium are dependent on the angle of incidence. With the addition of helium impurities to the plasma, the grass-like structure is still present, because the angular dependence of the sputtering yields is similar for deuterium and helium. On the other hand, argon suppresses the grass like structure even at very low concentrations. The angular dependence of the sputtering yields for argon shows that the maximum of the sputtering yield is reached at smaller angles than for helium or deuterium, and the maximum sputtering yield is also not much bigger than the sputtering yield

for an incident angle perpendicular to the surface. This is supposed to be the main reason for the uniform erosion of the surface and the suppression of the grass-like structure by argon. The same grass-like structure is also found for deuterium exposures of beryllium, and argon or helium impurities have the same influence on the structure as for aluminium. The results of the sputter yield measurements show that the experimental sputter yields are significantly lower than the calculation results from the TRIM code for flat surfaces when the grass-like structure is present on the surface, for both aluminium and beryllium exposures. With the suppression of the grass-like structure by argon impurities, also the measured sputter yields are increasing and reaching the predicted values from the TRIM simulations. When the grass-like structure is present, there is increased prompt redeposition of eroded material due to geometrical effects, which lead to a decreased effective erosion of aluminium. As the TRIM simulations do not take the roughness of the surface and the resulting redeposition into account, the TRIM simulations can only correctly reproduce the sputtering yields for a flat sample surface.

A third aspect investigated in the comparison between aluminium and beryllium is the deuterium retention under the influence of plasma impurities. The TDS results for the aluminium samples show that helium impurities reduce the deuterium retention in aluminium, as it was also observed also in tungsten. However, the reason for this reduction might not be the formation of helium nanobubbles, but simply the increased absolute erosion of the sample surface by helium because of its higher sputter yield. The erosion of the surface consequently also removes trapped deuterium from the sample. For argon, the deuterium retention stays constant. Also, the shape of the TDS spectra stays constant for all cases, which indicates that no additional trapping sites are formed by helium or argon. The comparison with beryllium shows a different behaviour for exposures with and without argon impurities. In a pure deuterium plasma, the deuterium retention is dominated by trapping sites produced by structural damages in the beryllium lattice produced by supersaturation of deuterium. Argon impurities suppress the formation of these trapping sites, and the total deuterium retention is strongly reduced.

The conclusion of these comparisons is that despite the major differences between aluminium and beryllium, like a different melting temperature, lattice structure and atomic mass, some aspects of their plasma-wall-interaction behaviour are similar. The influence of helium or argon impurities on the surface morphology and sputtering yields are comparable, at least for the parameter range observed in the experiments. However, as these similarities are caused by the angular dependence of the sputter yields, also other low- $z$  materials might exhibit the same behaviour. On

the other hand, the deuterium retention shows fundamentally different behaviours for aluminium and beryllium. Similar to the findings from the tungsten experiments, helium impurities decrease the deuterium retention in aluminium, while argon impurities do not decrease the deuterium retention. For beryllium, literature shows that argon reduces the total deuterium retention. As a consequence, aluminium cannot be used as a proxy material for beryllium concerning deuterium retention.

## 7 Appendix I: Diffusion simulation MATLAB code

```

%%%%%%%%%%%%%%%%%%%%%%%%%%%%%%%%%%%%%%%%%%%%%%%%%%%%%%%%%%%%%%%%%%%%%%%%%%
%Input parameters
%%%%%%%%%%%%%%%%%%%%%%%%%%%%%%%%%%%%%%%%%%%%%%%%%%%%%%%%%%%%%%%%%%%%%%%%%%

%Number of gridpoints
sizesteps=170;
%grid factor
gridfactor=1.07;
%start value diffusion [m^2/s]
d=1e-17;
%increase value diffusion [m^2/s]
dfactor=5e-15;
%reduction factor for helium diffusion
dredution=1/300;
%exposure time [s]
time=20000;
%reflection factor for the deuterium influx
influx_reflection=0.99868;
%trapping rate coefficient deuterium in helium bubbles
c1=8e-27;
%detrapping rate coefficient deuterium in helium bubbles
c2=4e-27;
%loss from porous structure?
c4=0;
%loss rate coefficient helium in helium bubbles
c3=0.05;
%impurity present = 1
helium=1;

%input profiles (format: [1:sizesteps]-matrix)
fluxinput=load('D:\Matlab\flux.mat');
if helium==1

```

---

```
hefluxinput=load('D:\Matlab\heflux.mat');
end

%%%%%%%%%%%%%%%%%%%%%%%%%%%%%%%%%%%%%%%%%%%%%%%%%%%%%%%%%%%%%%%%%%%%%%%%%
%Initializing
%%%%%%%%%%%%%%%%%%%%%%%%%%%%%%%%%%%%%%%%%%%%%%%%%%%%%%%%%%%%%%%%%%%%%%%%%

currenttime=0;

%loading input profiles

flux=fluxinput.flux;
heflux=hefluxinput.heflux;

%calculating grid spaces

dx(1)=1e-9;
xaxis(1)=0;
for x=2:1:50
    alpha(x)=1;
    dx(x)=dx(x-1)*alpha(x);
    xaxis(x)=xaxis(x-1)+dx(x);
end

for x=51:1:sizesteps
    alpha(x)=gridfactor;
    dx(x)=dx(x-1)*alpha(x);
    xaxis(x)=xaxis(x-1)+dx(x);
end

alpha(sizesteps+1)=1.07;

%calculating timestep size

dt = 0.24*dx(1)^2/d;
if dt>time/100000
    dt=time/100000;
```

---

```

end

%factors for derivative

for i=1:1:sizesteps
    a1(i)=alpha(i)+1;
    a2(i)=0.5*alpha(i)*(alpha(i)+1)*dx(i)^2;
end

clear fluencesum hefluencesum

%preallocate variables

inventory=zeros(10000,1);
profile=zeros(sizesteps,2);
heprofile=zeros(sizesteps,2);
d2profile=zeros(sizesteps,2);
diffusion1=zeros(1,sizesteps);
diffusion2=zeros(1,sizesteps);
diffusionhe=zeros(1,sizesteps);
loss=zeros(sizesteps,1);
safecount=1;

%%%%%%%%%%%%%%%%%%%%%%%%%%%%%%%%%%%%%%%%%%%%%%%%%%%%%%%%%%%%%%%%%%%%%%%%%
%Calculating
%%%%%%%%%%%%%%%%%%%%%%%%%%%%%%%%%%%%%%%%%%%%%%%%%%%%%%%%%%%%%%%%%%%%%%%%%

if helium==1

    %calculation with He

while currenttime<time

    %diffusion variation

diffusion2(:)=d+dfactor.*profile(:,1)./2e28;
diffusionhe(:)=d*dreduction;

```

---

```

diffusion2(1)=diffusion2(2);

%setting timestep size

dt = (0.24)*dx(1)^2/max(diffusion2);
currenttime=currenttime+dt;

%calculating profiles

for i=2:sizesteps-1
profile(i,2) = profile(i,1)+(alpha(i)*(diffusion2(i-1)+(
diffusion2(i)-diffusion2(i-1))/a1(i))*dt)/a2(i)*profile(i
-1,1)-(alpha(i)*(diffusion2(i-1)+(diffusion2(i)-
diffusion2(i-1))/a1(i))*dt)/a2(i)*profile(i,1)-((
diffusion2(i)+(diffusion2(i+1)-diffusion2(i))/a1(i))*dt)*
profile(i,1)/a2(i)+((diffusion2(i)+(diffusion2(i+1)-
diffusion2(i))/a1(i))*dt)/a2(i)*profile(i+1,1)-profile(i
,2)*dt*heprofile(i,1)*c1+d2profile(i,1)*dt*heprofile(i,1)
*c2*c4+dt*flux(i);
heprofile(i,2) = heprofile(i,1)+(alpha(i)*(diffusionhe(i-1)
+(diffusionhe(i)-diffusionhe(i-1))/a1(i))*dt)/a2(i)*
heprofile(i-1,1)-(alpha(i)*(diffusionhe(i-1)+(diffusionhe
(i)-diffusionhe(i-1))/a1(i))*dt)/a2(i)*heprofile(i,1)-((
diffusionhe(i)+(diffusionhe(i+1)-diffusionhe(i))/a1(i))*
dt)/a2(i)*heprofile(i,1)+((diffusionhe(i)+(diffusionhe(i
+1)-diffusionhe(i))/a1(i))*dt)/a2(i)*heprofile(i+1,1)-
heprofile(i,2)*c3*dt +dt*heflux(i);
d2profile(i,1)=d2profile(i,1)+profile(i,2)*dt*heprofile(i,1)
*c1-d2profile(i,1)*dt*heprofile(i,1)*c2;
end

%saving results

if currenttime > (safecount-1)*time/10000
safeprofile(:,safecount)=profile(:,2)+d2profile(:,1);
safeheprofile(:,safecount)=heprofile(:,2);
safe1profile(:,safecount)=profile(:,2);

```

---

```

safelossprofile (: , safecount)=loss (: ,1) ;
fluencesum ( safecount)=flux (1) *dx (1) / (1-
    influx _ reflection) ;
hefluencesum ( safecount)=heflux (1) *dx (1) / (1-
    influx _ reflection) ;
inventory ( safecount)=safeprofile (1 , safecount) *dx (1) ;
for i =2:1: sizesteps ;
    inventory ( safecount)=inventory ( safecount) +
        safeprofile (i , safecount) *dx (i) ;
    fluencesum ( safecount)=fluencesum ( safecount) +flux (i
        ) *dx (i) / (1- influx _ reflection) ;
    hefluencesum ( safecount)=hefluencesum ( safecount) +
        heflux (i) *dx (i) / (1- influx _ reflection) ;
end

%result output

resultflux=fluencesum ( safecount)
resultheflux=hefluencesum ( safecount)
resultfluence=sum ( fluencesum ) *time /10000
resultinventory=inventory ( safecount)
progress=currenttime

%plot

loglog (xaxis , [ flux (: ) , profile (: ,2) , d2profile (: ,1) ,
    safeprofile (: , safecount) , heprofile (: ,2) ])
axis ([1e-9 max (xaxis) 1e22 1e30 ])
hleg1=legend ( 'flux ' , 'D profile ' , 'D2 profile ' , 'total D
    profile ' , 'He profile ' ) ;
drawnow
    safecount=safecount+1;
end

%shift columns

profile (: ,1)=profile (: ,2) ;

```

---

```

    heprofile (:,1)=heprofile (:,2) ;

end

else

%calculation without He

while currenttime<time

    %diffusion variation

    diffusion2 (:)=d+dfactor.*profile (:,1)./2e28;
    diffusion2 (1)=diffusion2 (2) ;

    %setting timestep size

    dt = 0.24*dx (1) ^2/max (diffusion2) ;
    currenttime=currenttime+dt ;

    %calculating profiles

    for i=2:sizesteps-1
        profile (i,2) = profile (i,1)+(alpha (i)*(diffusion2 (i-1)
            +(diffusion2 (i)-diffusion2 (i-1))/a1 (i))*dt)/a2 (i)*
            profile (i-1,1)-(alpha (i)*(diffusion2 (i-1)+(
            diffusion2 (i)-diffusion2 (i-1))/a1 (i))*dt)/a2 (i)*
            profile (i,1)-((diffusion2 (i)+(diffusion2 (i+1)-
            diffusion2 (i))/a1 (i+1))*dt)/a2 (i)*profile (i,1)+((
            diffusion2 (i)+(diffusion2 (i+1)-diffusion2 (i))/a1 (i
            +1))*dt)/a2 (i)*profile (i+1,1) +dt*flux (i) ;;
    end

    %saving results

```

---

```

if currenttime > (safecount-1)*time/10000

    safeprofile(:,safecount)=profile(:,2);
    fluencesum(safecount)=flux(1)*dx(1)/(1-
        influx_reflection);
    inventory(safecount)=profile(1,2)*dx(1);

    for i=2:1:sizesteps;
        inventory(safecount)=inventory(safecount)+profile(
            i,2)*dx(i);
        fluencesum(safecount)=fluencesum(safecount)+flux(i
            )*dx(i)/(1-influx_reflection);
    end

    %result output

    resultflux=fluencesum(safecount)
    resultfluence=sum(fluencesum)*time/10000
    resultinventory=inventory(safecount)
    progress=currenttime

    %plotting

    loglog(xaxis,profile(:,2))
    axis([1e-9 max(xaxis) 1e22 1e30])
    hleg1=legend('D profile');

    drawnow
        safecount=safecount+1;
end

%shift column

profile(:,1)=profile(:,2);

end
end

```

## 8 References

- [1] M. P. Fewell  
The atomic nuclide with the highest mean binding energy  
*American Journal of Physics* 63, Nr. 7, 653-658 (1995)
- [2] J. Wesson  
Tokamaks  
Oxford Engineering Science Series No 48, Clarendon Press, Oxford (1997)
- [3] G. H. Miller et al.  
The National Ignition Facility  
*Opt. Eng.* 43(12), p. 2841-2853 (2004)
- [4] J. D. Huba  
NRL Plasma Formulary  
Naval Research Laboratory, page 45 (2013)
- [5] C. H. Skinner et al.  
Recent Advances On Hydrogen Retention in ITER's Plasma-Facing Materials:  
Beryllium, Carbon and Tungsten  
*Fusion Science and Technology* 54, 891-945 (2008)
- [6] A. Kallenbach et al.  
Impurity seeding for tokamak power exhaust: from present devices via ITER to  
DEMO  
*Plasma Phys. Control. Fusion* 55, 124041 (2013)
- [7] A. Manhard  
Deuterium Inventory in Tungsten After Plasma Exposure: A Microstructural  
Survey  
PhD Thesis, University Augsburg (2011)
- [8] J. Roth et al.  
Hydrogen in Tungsten as plasma-facing material  
*Phys. Scr.* T145, 014031 (2011)
- [9] G. Pintsuk  
Comprehensive Nuclear Materials 4.17 Tungsten as a Plasma-Facing Material  
Elsevier Ltd., p. 572 (2012)

- 
- [10] P. Boolchand et al.  
Mobile silver ions and glass formation in solid electrolytes  
Nature 410, 1070-1073 (2001)
- [11] R. A. Causey  
Hydrogen isotope retention and recycling in fusion reactor plasma-facing components  
Journal of Nuclear Materials 300, 91-117 (2002)
- [12] R. Frauenfelder  
Solution and Diffusion of Hydrogen in Tungsten  
J. Vac. Sci. Technol. 6, 388 (1969)
- [13] V. Kh. Alimov et al.  
Surface morphology and deuterium retention in tungsten exposed to low-energy, high flux pure and helium-seeded deuterium plasmas  
Phys. Scr. T138, 014048 (5pp) (2009)
- [14] A. A. Haasz et al.  
Deuterium retention in tungsten for fusion use  
Journal of Nuclear Materials 258-263, 889-895 (1998)
- [15] L. Buzi et al.  
Influence of tungsten microstructure and ion flux on deuterium plasma-induced surface modifications and deuterium retention  
Journal of Nuclear Materials, Accepted Manuscript (2014)
- [16] W. Wang  
Blister formation of tungsten due to ion bombardment  
Journal of Nuclear Materials 299-2, 124-131 (2001)
- [17] M. Miyamoto  
Observations of suppressed retention and blistering for tungsten exposed to deuterium-helium mixture plasmas  
Nucl. Fusion 49, 065035 (2009)
- [18] James F. Ziegler et al.  
SRIM - The Stopping and Range of Ions in Matter (2010)  
United States Naval Academy, Physics Dept., Annapolis, USA (2010)

- 
- [19] K. O. E. Henriksson et al.  
Difference in formation of hydrogen and helium clusters in tungsten  
*Applied Physics Letters* 87, 163113 (2005)
- [20] K. O. E. Henriksson et al.  
The Depths Of Hydrogen And Helium Bubbles In Tungsten: A Comparison  
*Fusion Science and Technology* 50, 43-57 (2006)
- [21] K. B. Wollner et al.  
Dynamic measurement of the helium concentration of evolving tungsten nanostructures using Elastic Recoil Detection during plasma exposure  
*Journal of Nuclear Materials*, available online 5 December 2014
- [22] S. Kajita et al.  
TEM observation of the growth process of helium nanobubbles on tungsten: Nanostructure formation mechanism  
*Journal of Nuclear Materials* 418 1-3, p152-158 (2011)
- [23] H. Iwakiri et al.  
Microstructure evolution in tungsten during low-energy helium ion irradiation  
*Journal of Nuclear Materials* 283-287, 1134-1138 (2000)
- [24] O. V. Ogorodnikova et al.  
Deuterium retention in tungsten exposed to low-energy pure and helium-seeded deuterium plasmas  
*Journal Of Applied Physics* 109, 013309 (2011)
- [25] E. Abramov et al.  
Hydrogen Trapping in helium damaged metals: a theoretical approach  
*Journal of Materials Science* 27, 2595-2598 (1992)
- [26] M. Miyamoto et al.  
Microscopic damage of tungsten exposed to deuterium-helium mixture plasma in PISCES and its impacts on retention property  
*Journal of Nuclear Materials* 415 S657-S660 (2011)
- [27] M. Yajima et al.  
Comparison of Damages on Tungsten Surface Exposed to Noble Gas Plasmas  
*Plasma Science and Technology* 15, No.3 (2013)

- 
- [28] [http://www.fz-juelich.de/iek/iek-4/DE/Forschung/03\\_PSI-2/\\_node.html](http://www.fz-juelich.de/iek/iek-4/DE/Forschung/03_PSI-2/_node.html)  
Institut für Energie- und Klimaforschung - Plasmaphysik (IEK-4), Forschungszentrum Jülich
- [29] <http://plasma.physik.hu-berlin.de/psi/psi.html>  
Lehrstuhl für Experimentelle Plasmaphysik, Arbeitsgruppe Plasmaphysik, Institut für Physik der Humboldt-Universität zu Berlin
- [30] O. Waldmann  
Untersuchung der Transportphänomene magnetisierter Plasmen in der Umgebung materieller Limiter  
PhD Thesis, Humboldt-University Berlin (2009)
- [31] M. Langowski  
Untersuchungen mit einer segmentierten Neutralisatorplatte in einem linearen Plasmagenerator  
Diploma Thesis, P45, Humboldt-University Berlin (2009)
- [32] E. V. Shun'ko  
Langmuir Probe in Theory and Practice  
Universal Publishers Boca Raton, Florida, USA 2009
- [33] R. L. Stenzel  
Typical Double Probe Trace and its Evaluation  
Plasma Physics Laboratory University of California, Los Angeles (1997)
- [34] L. Conde  
An introduction to Langmuir probe diagnostics of plasmas  
Department of Applied Physics University Madrid (2011)
- [35] Operating Instructions Acton Research Corporation SpectraPro-750i  
[www.acton-research.com](http://www.acton-research.com)
- [36] W. R. Wing et al.  
A Rapid Abel Inversion  
American Journal of Physics 39, 760-764 (1971)
- [37] B. Liebig  
Untersuchung der lokalen Anregung einer gepulsten Magnetronentladung mittels optischer Emissionsspektroskopie und Abel-Inversion  
TU Chemnitz (2008)

- 
- [38] H. Zohm  
Plasmaphysik  
Lecture notes LMU München (2012)
- [39] D. M. Goebel  
Ion source discharge performance and stability  
Phys. Fluids 25(6), 1093-1102 (1982)
- [40] E. Kautto et al.  
Analysing Methods for Thermal Desorption Spectra  
Phys. Scr. 55, 628-633 (1997)
- [41] [http://open.adas.ac.uk/detail/adf13/ionelec/ionelec\\_sxb%5D%5Bh0.dat](http://open.adas.ac.uk/detail/adf13/ionelec/ionelec_sxb%5D%5Bh0.dat)
- [42] S Brezinsek et al.  
Molecular and Atomic Deuterium in the Plasma Edge of TEXTOR-94  
Contrib. Plasma Phys. 42 6-7, 668-674 (2002)
- [43] S Brezinsek  
Untersuchung von atomarem und molekularem Wasserstoff vor einer Graphitoberfläche in einem Hochtemperatur-Randschichtplasma  
Jül-3962 p.20 (Dissertation Univ. Düsseldorf) (2002)
- [44] G. Sergienko et al.  
Molecular Deuterium Behaviour in Tungsten Divertor on JET  
Journal of nuclear materials 438, 1100-1103 (2013)
- [45] P. J. Bruggeman et al.,  
Gas temperature determination from rotational lines in non-equilibrium plasmas:  
a review  
Plasma Sources Sci. Technol. 23, 023001 (32pp) (2014)
- [46] W. Lochte-Holtgreven  
Plasma Diagnostics  
North-Holl. Publ. Comp., Amsterdam (1968) p. 433
- [47] [http://open.adas.ac.uk/detail/adf15/pec96%5D%5Bh/pec96%5D%5Bh\\_pju%5D%5Bh0.dat](http://open.adas.ac.uk/detail/adf15/pec96%5D%5Bh/pec96%5D%5Bh_pju%5D%5Bh0.dat)
- [48] A. Kreter et al.  
Mitigation of carbon erosion in beryllium seeded deuterium plasma under bom-

- 
- bardment by argon and helium ions in PISCES-B  
Journal of nuclear materials 417, (2011)
- [49] M. O'Mullane  
Photon emissivities for ArI and ArII  
ADAS-C(08)01(2008)
- [50] K. B. Fournier et al.  
IONIZATION STATE DISTRIBUTION AND RADIATIVE COOLING RATE  
FOR ARGON IN A LOW-DENSITY PLASMA  
ATOMIC DATA AND NUCLEAR DATA TABLES 70, 231-254 (1998)
- [51] L. Loeb  
Electrical Coronas Their Basic Physical Mechanisms  
University of California Press (1965)
- [52] D. Reiser, private communication
- [53] B.A. Trubnikov, "Reviews of Plasma Physics, Vol. I", ed. by M.A. Leontovich,  
Consultants Bureau, New York (1965)
- [54] M. A. Lennon  
Recommended Data on the Electron Impact Ionization of Atoms and Ions: Flu-  
orine to Nickel  
Journal of Physical and Chemical Reference Data 17, 1285 (1988)
- [55] M. Arnaud et al.  
An updated evaluation of recombination and ionization rates  
R. Astron. Astrophys. Suppl. Ser. 60, 425-457 (1985)
- [56] D. Nishijima et al.  
Spectroscopic determination of the singly ionized helium density in low electron  
temperature plasmas mixed with helium in a linear divertor plasma simulator  
Physics Of Plasmas 14, 103509 (2007)
- [57] R. K. Janev et al.  
Elementary Processes in Hydrogen-Helium Plasmas  
Springer-Verlag, Berlin (1987)
- [58] L. Schmitz et al.  
Plasma and neutral dynamics in a simulated tokamak gas target divertor  
Phys. Plasmas 2, 3081 (1995)

- 
- [59] M. O'Mullane  
[http://open.adas.ac.uk/detail/adf13/sxb96%5D%5Bhe/sxb96%5D%5Bhe\\_pjr%5D%5Bhe0.dat](http://open.adas.ac.uk/detail/adf13/sxb96%5D%5Bhe/sxb96%5D%5Bhe_pjr%5D%5Bhe0.dat) (1999)
- [60] A. Simon  
Ambipolar Diffusion in a Magnetic Field  
Phys. Rev. 98, 317 (1955)
- [61] D. Reiser  
Revised global drift fluid model for linear devices  
Phys. Plasmas 19, 072317 (2012)
- [62] F.F. Chen  
Introduction to Plasma Physics  
Plenum, New York, p. 169 (1974)
- [63] Atomic And Plasma-Material Interaction Data For Fusion, page 48-55  
Volume 7 Part B, IAEA, Vienna (2001)
- [64] M. I. Guseva et al.  
Sputtering of beryllium, tungsten, tungsten oxide and mixed W±C layers by deuterium ions in the near-threshold energy range  
Journal of Nuclear Materials 266-269, 222-227 (1999)
- [65] J. Roth et al.  
Data on low energy light ion sputtering  
MPI Report IPP9/26 (1979)
- [66] H.Y. Xu et al.  
Enhanced modification of tungsten surface by nanostructure formation during high flux deuterium plasma exposure  
Journal of Nuclear Materials 447, 22-27 (2014)
- [67] L. Marot et al.  
Can aluminium or magnesium be a surrogate for beryllium: A critical investigation of their chemistry  
Fusion Engineering and Design 88, 1718-1721 (2013)
- [68] A. Kreter et al.  
Erosion, formation of re-deposited layers and fuel retention for beryllium under the influence of plasma impurities  
Phys. Scr. to be published

- 
- [69] R.P. Doerner et al.  
Plasma-Induced Morphology Of Beryllium Targets Exposed In Pisces-B  
Journal of Nuclear Materials (2014)
- [70] Y. Yamamura et al.  
Angular dependence of sputtering yields of monatomic solids  
Report No. IPPJ-AM-26 (1983)
- [71] N. Matsunami et al.  
Energy Dependence of the Yields of Ion-Induced Sputtering of Monatomic Solids,  
IPPJ-AM-32, Institute of Plasma Physics, Nagoya University, Japan (1983)
- [72] W. Eckstein  
Calculated Sputtering, Reflection and Range Values  
IPP report 9/132, IPP Garching, Germany (2002)
- [73] R. Weissmann et al.  
Sputtering and backscattering of keV light ions bombarding random targets  
Radiat. Eff. 19,1, 7-14 (1973)
- [74] R.P. Doerner private communication
- [75] W. Eckstein et al.  
SDTrimSP: A Monte-Carlo Code for Calculating Collision Phenomena in Randomized Targets  
IPP report 12/3, IPP Garching, Germany (2007)
- [76] M. Reinelt et al.  
Ion implanted deuterium retention and release from clean and oxidized beryllium  
Journal of Nuclear Materials 390-391, 568-571 (2009)
- [77] G. R. Longhurst  
TMAP7 Manual  
Idaho National Engineering and Environmental Laboratory,EXT-04-02352  
(2004)
- [78] M. Oberkoffer  
Retention and release mechanisms of deuterium implanted into beryllium  
Nuclear Instruments and Methods in Physics Research B 269, 1266-1270 (2011)
- [79] G.-H. Lu et al.  
A review of modelling and simulation of hydrogen behaviour in tungsten at

- different scales  
Nucl. Fusion 54 089001(21pp) (2014)
- [80] B. J. Merrill et al.  
Simulating Tritium Retention in Tungsten with a Multiple Trap Model in the TMAP Code  
J. Plasma Fusion Res. Series, Vol. 10, p. 71-75 (2013)
- [81] V. Kh. Alimov et al.  
Depth distribution of deuterium in single- and polycrystalline tungsten up to depths of several micrometers  
Journal of Nuclear Materials 337-339, 619-623 (2005)
- [82] V. Kh. Alimov et al.  
Surface morphology and deuterium retention in tungsten and tungsten-rhenium alloy exposed to low-energy, high flux D plasma  
Journal of Nuclear Materials 454, 136-141 (2014)
- [83] R. B. Bird et al.  
Transport Phenomena  
John Wiley & Sons (1976)
- [84] M. H. J. 't Hoen  
Strongly Reduced Penetration of Atomic Deuterium in Radiation-Damaged Tungsten  
Phys. Rev. Lett. 111, 225001 (2013)
- [85] S. Möller et al.  
Time evolution of deuterium desorption from plasma-implanted tungsten and its flux density dependence  
Proceedings of 15th International Conference on Plasma-Facing Materials and Components for Fusion Applications (2015)
- [86] MATLAB R2011b  
MathWorks 2011
- [87] P. J. Roache  
Computational Fluid Dynamics (1st ed.)  
Hermosa Publishers (1972)

- 
- [88] W. H. Press  
Numerical Recipes: The Art of Scientific Computing  
Cambridge University Press (1986) p. 640
- [89] J. Noye  
Computational Techniques for Differential Equations  
p. 303, Elsevier Science Publishers B.V. (1984)
- [90] R. Causey et al.  
The Use of Tungsten in Fusion Reactors: A Review of the Hydrogen Retention  
and Migration Properties  
Physica Scripta T94, 9-15 (2001)
- [91] R. Causey et al.  
Tritium retention in tungsten exposed to intense fluxes of 100 eV tritons  
Journal of Nuclear Materials 266-269, 467-471 (1999)

## 9 List of figures

1	Divertor in ITER . . . . .	7
2	The different forms of deuterium retention in metals . . . . .	10
3	Tetrahedral (red), trigonal (green) and octahedral (black) interstitials in the bcc lattice (blue) [10] . . . . .	11
4	Energy levels for the solution ( $E_S$ ), diffusion ( $E_D$ ) and trapping( $E_T$ ) of deuterium in tungsten [11] . . . . .	11
5	TEM images of helium nanobubbles by helium plasma exposure at 570 K [17] . . . . .	14
6	Implantation depth of noble gas ions in tungsten in dependence of the incident energy [27] . . . . .	16
7	Layout of PSI-2 [30] . . . . .	18
8	Cylindrical cathode . . . . .	19
9	Magnetic field lines in PSI-2, cathode cross-section indicated in red .	20
10	Ion flux profiles with cylindrical and planar cathode for argon plasmas	20
11	planar cathode . . . . .	21
12	I-V characteristic . . . . .	21
13	Dispersion of the 2D imaging spectrometer . . . . .	24
14	Fulcher Bands Q-Branch as an example for the spectrometer images .	24
15	Spectrometer setup for the measurement of profiles along the plasma axis . . . . .	25
16	Inverse Abel transformation with the matrix method [37] . . . . .	26
17	measured signal and inverse abel transformed signal of the $D_\alpha$ line . .	27
18	Calibration factors of the 2D imaging spectrometer . . . . .	28
19	The position of the PSI-2 side manipulator . . . . .	29
20	Tungsten sample for the side manipulator sample holder . . . . .	30
21	The PSI-2 side manipulator sample holder with a sample in a deu- terium plasma . . . . .	30
22	PSI-2 with the new target station + target manipulator . . . . .	31
23	Target manipulator sample holder . . . . .	31
24	Sample exposure at 900 °C . . . . .	32
25	QMS signal for mass 4 and temperature versus time . . . . .	34
26	Graphic representation of the parameters required for the peak-area method . . . . .	36
27	Intensity ratio of $H_\alpha/H_\beta$ . . . . .	37
28	Intensity ratio of $H_\alpha/H_\gamma$ . . . . .	38

29	Intensity ratio of $H_{\beta}/H_{\gamma}$ . . . . .	38
30	Electron density profiles by $H_{\alpha}/H_{\gamma}$ (lines) and Langmuir probe (points)	40
31	Fulcher Q(0-0) band emission lines . . . . .	41
32	Boltzmann plot of the Fulcher Q2 - Q5 lines . . . . .	42
33	Rotational temperature as a function of electron density for TEXTOR and PSI-2 . . . . .	43
34	Recombining deuterium plasma in PSI-2 . . . . .	43
35	Electron density in a recombining deuterium plasma in PSI-2 under variation of the neutral gas pressure and at 2 different axial positions	45
36	Ratios of the P9 and P7 line emissions for different electron densities	46
37	Electron temperature in a recombining plasma in PSI-2 under varia- tion of the neutral gas pressure and at 2 different axial positions . . .	47
38	Photon emissivity coefficients for the 434,8 nm transition of $Ar^{+}$ [49]	49
39	Argon ion ratios for a pure argon plasma, calculated with (15) . . . .	50
40	Simulated argon ion charge ratio for $T_e=5-12$ eV along the z-axis . . .	52
41	Argon ion ratios for mixed deuterium-argon plasmas with variation in discharge power and argon gas ratio . . . . .	54
42	Results for $n_{He^{+}}/n_e$ calculated with equation (17) for mixed deuterium- helium plasmas with variation in helium gas ratio . . . . .	56
43	Photon emissivity coefficients for the 468,6 nm transition of $He^{+}$ for $n_e = 10^{12} \text{ cm}^{-3}$ [56] . . . . .	57
44	Measured perpendicular confinement time compared to classical and Bohm confinement time . . . . .	59
45	Helium ion ratios for mixed deuterium-helium plasmas with variation in helium gas ratio . . . . .	60
46	Surface of sample type A before (a) and after (b) deuterium exposure and surface of sample type B before (c) and after (d) deuterium exposure	63
47	Surface of sample type A after deuterium exposure without (a) and with 1 % (b) and 5 % (c) helium impurity in the plasma . . . . .	65
48	Surface of sample type A after deuterium exposure without (a) and with 4 % (b) and 8 % (c) argon impurity in the plasma . . . . .	66
49	TEM cross-section images of sample type C exposed to deuterium plasmas with 8 % Ar, 5 % He and 0 % impurities. a) platinum coating, b) helium nanobubbles / defects, c) bulk tungsten . . . . .	67
50	TDS spectra with different amounts of helium impurities during ex- posure . . . . .	68

51	Two Voigt-shaped peaks fitted to the TDS spectrum for the case of pure deuterium exposure . . . . .	69
52	TDS spectra with different amounts of argon impurities during exposure	71
53	Deuterium retention in dependence of the deuterium fluence to the target with and without helium impurities . . . . .	73
54	Aluminium sample . . . . .	75
55	Aluminium sample surface before (a,b) and after (c) exposure to pure deuterium plasma . . . . .	76
56	Beryllium (a) [68] and aluminium sample (b,c) after exposure to pure deuterium plasma . . . . .	77
57	Aluminium samples after exposure with different argon impurity concentrations (all same magnification) . . . . .	78
58	Aluminium sample after exposure to deuterium plasma with 6 % argon impurity . . . . .	78
59	Beryllium samples after exposure with different argon impurity concentrations (all same magnification) [68] . . . . .	79
60	Aluminium (a) and beryllium (b) samples after exposure with pure argon plasma (all same magnification) [68] . . . . .	79
61	Aluminium samples after exposure with different helium impurity concentrations and pure helium plasma (100 %) . . . . .	80
62	Relation between the angle of the grass-like structure ( $\alpha$ ) to the incident angle ( $\Theta$ ) . . . . .	82
63	Angular dependence of the sputtering yields of deuterium, helium and argon on aluminium and beryllium . . . . .	84
64	Sputter yields for exposures of aluminium and beryllium to deuterium plasmas with different impurities . . . . .	85
65	Erosion at a surface with grass-like structures and at a flat surface . .	86
66	Sputtering yields by TRIM calculations for exposures of aluminium and beryllium to deuterium plasmas with different impurities . . . . .	87
67	TDS spectra of aluminium samples Al-1 (black) and Al-2 (red) measured with the TDS systems at FZJ-IEK4 and UCSD respectively . .	88
68	TDS spectra of aluminium samples exposed to deuterium plasma with different ratios of Ar or He impurities . . . . .	89
69	TDS spectra of beryllium exposures in PISCES-B with argon impurities [68] . . . . .	91
70	Calculated diffusion depth in comparison to experimental results from literature for deuterium in tungsten([13, 81, 82]) . . . . .	94

---

71	Scheme of the diffusion-calculation . . . . .	97
72	Calculated deuterium profile with constant and variable space grid steps . . . . .	99
73	Deuterium profiles in tungsten for a deuterium flux of $10^{22} \text{ m}^{-2}\text{s}^{-1}$ and mean implantation depth of 2 nm . . . . .	100
74	Simulated deuterium and helium depth profiles from exposures with and without 5 % helium impurities . . . . .	102
75	Deuterium depth profiles from [24] in ITER-grade tungsten with and without 10 % helium impurities at 320 K sample temperature . . . .	103
76	Simulated deuterium and argon depth profiles from exposures with and without 5 % argon impurities . . . . .	105
77	Simulated deuterium retention in dependence of the deuterium fluence with and without 5 % helium or argon impurities . . . . .	107
78	Simulated deuterium retention in dependence of the deuterium fluence with and without 5 % helium impurities at 4 different helium depth profiles . . . . .	108
79	Total deuterium retention in tungsten with and without helium impurities under variation of the sample temperature [13] . . . . .	109

## Danksagung

An dieser Stelle möchte ich mich bei allen Personen bedanken, die mich während meiner Arbeit unterstützt haben. Insbesondere bedanke ich mich bei:

Prof. Bernhard Unterberg für die Ermöglichung dieser Arbeit und die Mithilfe bei vielen physikalischen Fragestellungen,

Arkadi Kreter für die sehr gute Betreuung meiner Arbeit und der Experimente,

Prof. Uwe Czarnetzki, Prof. Christian Linsmeier, und Prof. Ulrich Samm für die zusätzliche fachliche Unterstützung meiner Arbeit,

Albrecht Pospieszczyk, Michaele Freisinger, Marcin Rasinski, Dirk Reiser, Luxherta Buzi, Sören Möller, Michael Hubeny und Mirosław Zlobinski für die gute Zusammenarbeit und Hilfe im Labor,

Sebastian Kraus, Thorsten Tietz und Michael Vogel für die technische Unterstützung an PSI-2,

allen Mitarbeitern des Instituts IEK-4 für die angenehme Arbeitsatmosphäre, sowie meinen Eltern und meinem Bruder für die Motivation und Unterstützung während meiner gesamten Promotionszeit.

Vielen Dank!

## Lebenslauf

Persönliche Daten	
Name	Michael Reinhart
Geburtstag	27.05.1985
Geburtsort	Gelsenkirchen-Buer
Schulausbildung und Studium	
08/1991-07/1995	Pfefferacker-Grundschule, Gelsenkirchen
08/1995-06/2004	Gymnasium, Annette von Droste-Hülshoff-Gymnasium, Gelsenkirchen
10/2005-09/2008	Bachelorstudium Physik, Ruhr-Universität Bochum, Abschlussarbeit "Modellierung und experimentelle Untersuchung eines kapazitiven Energiespeichers"
10/2008-03/2011	Masterstudium Physik, Ruhr-Universität Bochum, Abschlussarbeit "Entwurf und Realisation eines Pinch-Experiments"
06/2011-07/2015	Promotionsstudium Physik, Ruhr-Universität Bochum Doktorand am Institut für Energie- und Klimaforschung 4 - Plasmaphysik, Forschungszentrum Jülich



Band / Volume 283

**Entwicklung von geträgerten protonenleitenden  
Dünnschichtmembranen für die Wasserstoffabtrennung**

W. Deibert (2015), XI, 117 pp

ISBN: 978-3-95806-082-1

Band / Volume 284

**Thermochemische Beständigkeit von keramischen Membranen  
und Katalysatoren für die H<sub>2</sub>-Abtrennung in CO-Shift-Reaktoren**

E. M. H. Forster (2015), X, 137 pp

ISBN: 978-3-95806-084-5

Band / Volume 285

**Spektrale aktinische Flussdichten und Photolysefrequenzen -  
Untersuchungen in der atmosphärischen Grenzschicht und der freien  
Troposphäre**

I. M. Lohse (2015), VI, 111, VII-XXIII pp

ISBN: 978-3-95806-086-9

Band / Volume 286

**Neue Charakterisierungsmethoden für die Gasdiffusionslage in PEM-  
Brennstoffzellen vor dem Hintergrund produktionsprozessbedingter  
Materialschwankungen**

S. M. Bach (2015), VIII, 149 pp

ISBN: 978-3-95806-088-3

Band / Volume 287

**Using the anisotropy of electrical properties for the characterization  
of sedimentological structures and preferential flow processes**

S. Al-Hazaimay (2015), xxii, 94 pp

ISBN: 978-3-95806-090-6

Band / Volume 288

**Aktivitätsuntersuchungen und Methoden zur Regeneration von  
Katalysatoren für die autotherme Reformierung von Dieselmotorkraftstoffen**

K. Löhken (2015), II, 147 pp

ISBN: 978-3-95806-093-7

Band / Volume 289

**Large-Scale Three Dimensional Modelling  
of a Direct Methanol Fuel Cell Stack**

J. W. McIntyre (2015), 138 pp

ISBN: 978-3-95806-094-4

Band / Volume 290

**Abscheidung von Wärmedämmschichtsystemen mit dem Plasma Spray-Physical Vapor Deposition- (PS-PVD-) Prozess – Untersuchung des Prozesses und der hergestellten Schichten**

S. Rezanka (2015), XII, 204 pp  
ISBN: 978-3-95806-095-1

Band / Volume 291

**Characterization & Modification of Copper and Iron Oxide Nanoparticles for Application as Absorber Material in Silicon based Thin Film Solar Cells**

M. R. Nuys (2015), XII, 123 pp  
ISBN: 978-3-95806-096-8

Band / Volume 292

**Interpretation of L-band brightness temperatures of differently tilled bare soil plots**

M. Dimitrov (2015), XIV, 116 pp  
ISBN: 978-3-95806-098-2

Band / Volume 293

**Atrazine in the environment 20 years after its ban: long-term monitoring of a shallow aquifer (in western Germany) and soil residue analysis**

D. S. Vonberg (2015), 149 pp  
ISBN: 978-3-95806-099-9

Band / Volume 294

**Yttria-Stabilized Zirconia / Gadolinium Zirconate Double-Layer Plasma-Sprayed Thermal Barrier Coating Systems (TBCs)**

E. Bakan (2015), viii, 131 pp  
ISBN: 978-3-95806-100-2

Band / Volume 295

**Hydration and dehydration at the tropical tropopause**

C. Schiller (2015), 72 pp  
ISBN: 978-3-95806-101-9

Band / Volume 296

**Influence of Impurities on the Fuel Retention in Fusion Reactors**

M. Reinhart (2015), 140 pp  
ISBN: 978-3-95806-105-7

Weitere **Schriften des Verlags im Forschungszentrum Jülich** unter  
<http://www.zb1.fz-juelich.de/verlagextern1/index.asp>



**Energie & Umwelt /  
Energy & Environment  
Band / Volume 296  
ISBN 978-3-95806-105-7**

